Advanced Brachytherapy Dosimetric Considerations

By

Christopher S. Melhus

M.Sc. Nuclear Engineering (2002)
Massachusetts Institute of Technology

B.A. Physics (1997)
Reed College

Submitted to the Division of Health Science and Technology
in Partial Fulfillment of the Requirements for the Degree of

Doctor of Philosophy
at the
Massachusetts Institute of Technology

June 2008

Signature of Author _____
Harvard-MIT Division of Health Sciences and Technology
7 March 2008

Certified by _____
Mark J. Rivard, Ph.D.
Associate Professor of Radiation Oncology
Tufts University School of Medicine
Thesis Supervisor

Accepted by _____
Martha L. Gray, Ph.D.
Edward Hood Taplin Professor of Medical and Electrical Engineering
Director, Harvard-MIT Division of Health Sciences and Technology

Advanced Brachytherapy Dosimetric Considerations

by

Christopher S. Melhus

Submitted to the Division of Health Science and Technology and
the Department of Nuclear Science and Engineering on
7 March 2008 in Partial Fulfillment of the Requirements
for the Degree of Doctor of Philosophy in Radiological Sciences

ABSTRACT

The practice of brachytherapy and brachytherapy dosimetry was investigated with emphasis on evaluations of dose distributions and shielding considerations for both photon- and neutron-emitting radionuclides. Monte Carlo simulation methods were employed to calculate dose distributions for virtual and commercial brachytherapy sources. Radionuclides studied were ^{103}Pd, ^{125}I, ^{131}Cs, ^{137}Cs, ^{169}Yb, ^{192}Ir, and ^{252}Cf. ^{252}Cf sources also emit neutrons from spontaneous fission. The brachytherapy dosimetry protocol recommended by the American Association of Physicists in Medicine was followed and evaluated for conditions of partial scatter (non-infinite media) and material inhomogeneities, both commonly encountered in brachytherapy treatment. Furthermore, energy-dependent characteristics of dosimetry parameters were evaluated and reference calculations performed for virtual photon and neutron sources. These findings were applied to three clinical brachytherapy cases: eye plaques using ^{103}Pd, ^{125}I, and ^{131}Cs; high-dose rate ^{252}Cf treatment; and, ^{252}Cf plaques for superficial lesions. For eye plaques, material heterogeneities were significant for each radionuclide with dose reduction at 5 mm of 18%, 11%, and 10% for ^{103}Pd, ^{125}I, and ^{131}Cs, respectively. For a proposed high-dose rate ^{252}Cf source (5mm length), relative brachytherapy dosimetry parameters were found to be similar to those obtained for a low-dose rate Applicator Tube-type source (15 mm length). Considering ^{252}Cf plaque brachytherapy when partial scatter conditions were accounted for, central axis equivalent dose rate decreased by 11 ± 1% and 7 ± 2% for depths of 4 to 50 mm, respectively. The ratio of neutron dose to total physical dose was 70 ± 1% and 57 ± 2% for depths of 4 and 50 mm, respectively, while the fractional dose-equivalent due to neutrons was 93 ± 1% and 89 ± 2% at these depths, respectively. Finally, shielding requirements for a clinical high-dose rate ^{252}Cf source were explored for common shielding materials and a linear accelerator vault. Lead, polyethylene, and borated polyethylene were evaluated for neutron, primary photon, and secondary photon attenuation. Half-value layers of 0.70, 0.15, and 0.13 m were obtained for lead, polyethylene, and borated polyethylene, respectively. A linear accelerator vault was found to adequately shield up to a 5 mg ^{252}Cf source for regular clinical use.

Thesis Supervisor: Mark J. Rivard Ph.D.
Title: Associate Professor of Radiation Oncology
Tufts University School of Medicine

ACKNOWLEDGEMENTS

Support was provided in part by appointment to the U.S. Department of Energy Nuclear Engineering and Health Physics Fellowship Program, sponsored by the U.S. Department of Energy's Office of Nuclear Energy, Science, and Technology (**sections 3.2**, **4.1**, and **4.2**). Computer time for Monte Carlo calculations was provided by the Radiation Saftey Information Computational Center at Oak Ridge National Laboratory (**section 4.1**). For the use of ^{252}Cf, the author is indebted to the U. S. Department of Energy's Californium University Loan Program as administered by the Office of Nuclear Materials production through the facilities of the Oak Ridge National Laboratory (**section 4.2**). Additional resources were provided by Tufts-New England Medical Center and Tufts University School of Medicine.

Prof. Ademir da Silva of the Universidade Federal do Rio de Janeiro kindly shared Monte Carlo input files as used in reference **99** for **section 4.1**. Dr. Sou-Tung Chiu-Tsao provided helpful information for **section 2.2**. Mrs. Bernadete Kirk was a strong supporter of this work and provided assistance through the Radiation Safety Information Computational Center. The Chair of Radiation Oncology at Tufts University School of Medicine, Dr. David Wazer, generously provided travel support to present this work at national meetings of the American Association of Physicists in Medicine, the American Brachytherapy Society, and the American Nuclear Society.

I am very appreciative of the guidance and support provided by Prof. Jeffrey A. Coderre, the thesis reader. He supported efforts to perform clinical research at Tufts-New England Medical Center and enabled work away from the MIT campus to take place. Prof. Jacquelyn Yanch has supported my clinical research efforts since I matriculated to MIT in 1999 and was on the dissertation committee.

Finally, this dissertation would not have been possible without the mentorship and unyielding support of Prof. Mark J. Rivard, the thesis advisor. At every step, he has encouraged me to be a better scientist and to effectively communicate results to the scientific community. In addition to these academic pursuits, he has supervised my training as a medical physicist which put this work in context with clinical needs and the impact on patient care.

DEDICATION

This dissertation is lovingly dedicated to my wife, Kate.

TABLE OF CONTENTS

1 INTRODUCTION

1.1 Background

1.1.1 INTRODUCTION TO BRACHYTHERAPY

In the year 2007, the American Cancer Society estimated over 1.4M new cancer diagnoses in the United States.[1] More than half of these patients are expected to receive radiation therapy towards curing cancerous disease or relieving symptoms. Approximately 0.1M patients will receive brachytherapy for the management of their disease. Brachytherapy is the medical practice of placing material that emits ionizing radiation directly adjacent to or within a tumor or lesion. The placement may be within a body cavity or lumen, in tissue, or superficial. Furthermore, treatment can be delivered over short time periods using mechanical systems to rapidly position and move a radiation source, or over long time periods using permanently implanted radioactive seeds.

Male patients commonly receive brachytherapy treatment for prostate cancer, which accounted for an estimated 0.2M new cancers (29%) and 0.03M (9%) deaths in the year 2007.[1] Many anatomical sites and cancer types are treated with brachytherapy or with a combination of brachytherapy and other treatment modalities, such as external beam radiotherapy, surgery, or chemotherapy. For example, ocular melanoma (2,340 estimated 2007 cases) can be treated with superficial plaque brachytherapy; gynecological cancers (78,290 estimated 2007 cancers) can be treated with specialized applicators; and breast cancer (178,480 estimated 2007 cancers) treatments can be augmented with a brachytherapy boost or can be treated with brachytherapy as monotherapy.[1-4]

Brachytherapy has been applied for over a century, with the first suggestion of the practice closely following the discovery of radioactivity in 1896.[5] Early encapsulated clinical brachytherapy sources contained mg quantities of ^{226}Ra, one of the few radionuclides available at the turn of the 19th century. Because the modern quantity "activity" [disintegrations s^{-1}] was not defined at the time, early measurements of ^{226}Ra source strength were defined using an analytical balance.[6] Through the efforts of Marie Curie, the measurement unit "Curie" [Ci] was defined as "the quantity of emanation in equilibrium with one gram of radium" in 1912.[7] By the early 1920s, ^{226}Ra standards were available in Europe to calibrate and certify ^{226}Ra sources.[6,7]

Brachytherapy treatments during this era comprised needles or capsules loaded with ^{226}Ra ($t_{½}$ = 1600 y) that were implanted throughout a lesion following a loading system to obtain desired dose distributions. Examples of these loading systems are the Quimby (1932), Manchester (1934), and Paris (1960) systems where the differences arise from uniformity of source strength and/or the geometrical distribution of sources.[8] For example, the Paris system employs uniformly loaded sources that are regularly spaced in one or two planes.[9] By following source placement rules prescribed by each system, the radiation oncologist (previously known as the radiation therapist) would know the approximate shape and magnitude of dose distributions during treatment. Thus, brachytherapists planned patient treatments while avoiding difficult hand calculations and in the absence of computers.

Following World War II, nuclear research reactors allowed the production of radionuclides that did not occur naturally, and new radionuclide sources were popularized, such as ^{60}Co, ^{125}I, ^{137}Cs, ^{192}Ir, and ^{198}Au among others. In the 1950s, source strength started being reported in equivalent mg of ^{226}Ra (mg Ra-eq.), where the exposure rate of the new source was compared to a ^{226}Ra source filtered by a 0.5 mm-thick Pt capsule.[6] Thus, the decades of experience with ^{226}Ra sources continued to guide the field of brachytherapy with new radionuclide-based sources.

The practice of comparing radionuclide sources to ^{226}Ra changed when manufacturing advances allowed the miniaturization of brachytherapy sources and the mass-production of small sources containing radionuclides with high specific activity. These advances led to the introduction of ^{125}I sources ($t_{½}$ = 59.4 d) for use in permanent

implants. With implants containing a higher number of sources, the historic dosimetry systems were no longer adequate for determining dose distributions. The National Cancer Institute commissioned the Interstitial Collaborative Working Group to evaluate methods for calculating brachytherapy dose distributions. This commission was followed in 1988 by the formation of the American Association of Physicists in Medicine (AAPM) Task Group 43 Report (TG-43), which introduced a quantitative brachytherapy dosimetry formalism and recommended brachytherapy dosimetry data for selected brachytherapy sources in 1995.[10] A discussion of the AAPM TG-43 brachytherapy dosimetry formalism follows in **section 1.1.2**.

For much of the 20th Century, brachytherapy was administered by hand, which resulted in high radiation doses to oncologists, physicists, support personnel, and patients in adjacent rooms. Remote afterloading was introduced in the 1960s to reduce these concerns.[11] A remote afterloader is a mechanical device that can accurately position a small radiation source attached to a wire. By utilizing mm positioning accuracy and varying the "dwell" time at each position, a remote afterloader can create more conformal dose distributions than low-dose rate (LDR) brachytherapy. Due to the extreme variation in dose rate between LDR and high-dose rate (HDR) brachytherapy, brachytherapists must account for differences in radiobiological effect.[12] Most commercial remote afterloaders utilize a HDR ^{192}Ir source ($t_{½}$ = 73.8 d) with a maximum activity of 10 Ci, where HDR designates dose rates exceeding 12 Gy h^{-1} at the prescription point.[11]

In the beginning of the 21st Century, novel developments in brachytherapy technology continue to occur. For example ^{131}Cs, a radionuclide not previously used in brachytherapy, was developed and is in clinical use. A multi-institution phase II clinical trial demonstrated ^{131}Cs to be a viable alternative to seeds containing ^{125}I and ^{103}Pd, which have been in use for 25 and 21 years, respectively.[13-15] Other notable advancements include the introduction of an electronic brachytherapy source, the Xoft Inc., Axxent system.[16] The Axxent is a miniature, single-use x-ray tube allowing a peak accelerating potential of 50 kV with a W target. Photons emitted by the Axxent exhibit similar depth-dose characteristics to ^{125}I; although, the Axxent exhibits increased anisotropy near the connecting cable.[16] In contrast to radionuclide-based sources, the

Xoft Axxent does not provide a serious radiological risk to hospital personnel as a switchable electric current is needed to generate radiation.

1.1.2 Brief History of Brachytherapy Dosimetry

Early brachytherapy dosimetry measurements were hindered by the lack of an appropriate exposure calibration standard. While ^{226}Ra standards allowed relative classification of source strength by mass, quantitative measure of the exposure rate from a given source was not possible. By the late 1920s, orthovoltage radiotherapy beams were calibrated in Roentgens [R] using a free-air ionization chamber; however, a comparable method for brachytherapy source calibration was lacking.[6] Between 1920 and 1940, investigators attempted to compare treatment by orthovoltage therapy and brachytherapy using biological dosimeters, such as the threshold erythema dose (TED) which is the quantity required to produce erythema in 80% of irradiated subjects (~11 Gy). While biological dosimeters allowed comparison of the two modalities, the need for a directly measurable quantity to benchmark dose distributions limited the development of quantitative brachytherapy dosimetry.

One of the first methods to calculate dose distributions about a linear source was demonstrated by Sievert in 1921.[17] The Sievert Integral was obtained by dividing a line source into short sections that were treated as point sources. By summing the contributions from each point and multiplying by an estimated exposure rate constant (Γ_{Ra}), the exposure rate at a point was calculated. An example of a Sievert Integral for a source with length L, mass of ^{226}Ra M_{eq}, and exposure rate constant Γ_{Ra} is given in equation **1.1.1**.

$$\dot{X}(x,y) = \frac{M_{Ra}\Gamma_{Ra}}{Ly} e^{\bar{\mu}t} \int_{\theta_1}^{\theta_2} e^{-\bar{\mu}t\cdot\sec(\theta)} d\theta \qquad \textbf{(1.1.1)}$$

In equation **1.1.1**, the encapsulation thickness, t, and average attenuation of the encapsulation, $\bar{\mu}$, contribute to the calculation of exposure at a point (x,y), where x is along the source axis. The Sievert Integral has been shown to accurately simulate dose distributions for ^{226}Ra and ^{192}Ir sources in regions parallel to the source, but the technique does not compare favorably to Monte Carlo (MC) calculations near the source long

axis.[17] These differences are likely due to the impact of attenuation in source internal components (*e.g.*, Ag or Pb markers), which was not included in the Sievert Integral.

In addition to the semi-empirical Sievert Integral, individual source dosimetry in the latter-half of the 20th Century was reported using along-and-away tables. These tables listed the dose rate as a function of position in a two-dimensional grid along and away from the source long axis. For multiple source implants, the brachytherapist employed superposition to determine the total dose at any point in the implant. However, this process became tedious as the number of sources in an implant increased. Furthermore, it is necessary to interpolate along-and-away data, and steep dose gradients near the source can introduce interpolation errors.

The development of Bragg-Gray cavity theory in 1957 allowed calibration of ^{226}Ra sources in terms of exposure [R], which was the calibration standard for orthovoltage x-rays during that era.[6] Thus, brachytherapists could compare clinical findings to outcomes from external-beam treatment. The National Institute of Standards and Technology (NIST; formerly the National Bureau of Standards) introduced exposure standards for ^{137}Cs, ^{60}Co, ^{192}Ir, and ^{125}I between 1970 and 1984 based on the Ritz Free-Air Chamber, which is the national primary calibration standard for W x-ray sources between 20 and 100 kVp.[18,19]

As described in **section 1.1.1**, the 1995 AAPM TG-43 Report defined a quantitative dosimetry formalism that replaced Sievert integrals and along-and-away tables.[10] A summary of the TG-43 brachytherapy dosimetry parameters is included in Appendix II, **section 7.2**. Generally, the TG-43 formalism is designed to reproduce dose distributions in a semi-infinite liquid water phantom. Brachytherapy dosimetry investigators are advised to perform simulations and measurements in a phantom large enough to minimize losses due to lack of backscattering material.[20] Because the medium is water, no considerations are given to differences in material or tissue heterogeneities. Both of these effects have been successfully addressed for treatment planning of external photon beams, but still have not been incorporated into TPS for brachy.[21-23] For external photon beam TPS, heterogeneity corrections in the mediastinum were demonstrated to range from 5% to 16% for photon energeies between ^{60}Co and 25 MV, with correction factors as high as 21% for 25 MV in lung tissue.[24]

Since this landmark publication, brachytherapy dose distributions have largely been reported using the AAPM TG-43 formalism. To be included in consensus treatment data approved by the AAPM, a brachytherapy source must have MC-calculated and experimentally-measured brachytherapy dosimetry parameters published in a peer-reviewed journal.[25] The AAPM revised the dosimetry formalism in a 2004 update to the TG-43 report (TG-43U1), but limited the scope to ^{103}Pd and ^{125}I sources.[20] The AAPM TG-43U1 formalism, which calculates the dose rate in spherical coordinates about a source aligned along $\theta = 0°$, is given in equation **1.1.2**.

$$\dot{D}(r,\theta) = S_K \Lambda \frac{G_L(r,\theta)}{G_L(r_0,\theta_0)} g_L(r) F(r,\theta) \qquad \textbf{(1.1.2)}$$

In equation **1.1.2**, S_K is the air kerma strength [cGy cm^2 h^{-1}], L is the dose rate constant [cm^{-2}], $G_L(r,\theta)$ is the geometry function that corrects for inverse square effects, $g_L(r)$ is the radial dose function that corrects for attenuation and scatter along $\theta = 90°$, and $F(r,\theta)$ is the two-dimensional anisotropy function that corrects for attenuation and scatter at (r,θ) relative to $(r, 90°)$.

The radionuclide limitation was imposed by the physical dimensions of the Wide Angle Free Air Chamber (WAFAC) air kerma strength primary calibration standard at NIST in 1999.[18] The WAFAC was developed because deficiencies were identified in the previous standard, the Ritz Free-Air-Chamber, and the introduction of new radionuclides, such as ^{103}Pd, warranted a new standard.[18] The WAFAC was not physically large enough to measure air kerma strength for high-energy sources such as ^{192}Ir due to the increased pathlength of secondary charged particles, *i.e.*, electrons. Nonetheless, dose distributions in water using the TG-43 brachytherapy dosimetry formalism are published for several high- and low-energy brachytherapy sources, such as ^{131}Cs, ^{137}Cs, ^{169}Yb, ^{192}Ir, and ^{252}Cf.[26-30] To be compatible with the AAPM TG-43U1 formalism, S_K and Λ for high-energy radionuclides would be defined for primary calibration standards other than the NIST WAFAC air kerma standard.

Contemporary treatment planning systems implement the TG-43 dosimetry formalism; however, not all systems are capable of calculating the two-dimensional dosimetry formalism. These systems employ the one-dimensional version of the formula

where the geometry function is replaced with a point source representation (r^{-2}); and $F(r,\theta)$ is replaced with $\phi_{an}(r)$, the one-dimensional anisotropy function. When multiple sources are employed, superposition determines the total dose distribution. Thus, the limitations and assumptions of the AAPM TG-43 brachytherapy dosimetry formalism discussed above are also present in contemporary brachytherapy treatment planning systems. Even for planning systems that display three-dimensional patient data, such as computed tomography, the material heterogeneities and volume limitations are not included in dose calculation.

Both of the recently developed novel brachytherapy sources discussed in **section 1.1.1**, the ^{131}Cs seed and electronic Xoft Axxent, can utilize the AAPM TG-43 brachytherapy dosimetry formalism and be implemented in contemporary brachytherapy treatment planning systems. However, the formalism is not easily applied to other novel, developing brachytherapy techniques. For example, ^{90}Y-loaded microspheres (glass beads with diameter 25 ± 10 μm) have been delivered to liver tumors through the hepatic artery using interventional radiology techniques.[31] Microsphere implants result in large numbers of small sources in a highly non-uniform manner that would not be readily applied to the AAPM TG-43 formalism. Similarly, a technique for treating brain tumors has been developed where a balloon is inserted into a resection cavity and filled with a liquid ^{125}I solution.[32] Additional brachytherapy dosimetry research is needed to determine if the AAPM TG-43 formalism can be modified to include these sources or if a new formalism is needed.

1.1.3 CALIFORNIUM BRACHYTHERAPY

^{252}Cf is a man-made trans-plutonium radionuclide that largely undergoes alpha decay; however, 3.09% of nuclear transitions follow spontaneous fission.[33] The half-life of ^{252}Cf is 2.645 y. Oak Ridge National Laboratory (ORNL) produced Cf isotopes from approximately 100 g highly-enriched heavy Cm targets (^{244}Cm, ^{246}Cm, and ^{248}Cm) irradiated in the High-Flux Isotope Reactor for ~7 months.[34] Combinations of neutron activation and beta decay leads to successively higher atomic numbers. For example, neutron activation of ^{248}Cm produces ^{249}Cm ($t_{½}$ = 64 m) that beta decays to ^{249}Bk ($t_{½}$ = 330 d) that beta decays to ^{249}Cf ($t_{½}$ = 351 y), and subsequent neutron capture reactions are

required to produce Cf isotopes with atomic numbers 249-254.[33] Due to the amount of time required to produce ^{252}Cf and the extensive radiochemistry needed to separate Cf isotopes from the Cm target, ^{252}Cf is both extremely rare and expensive.

Clinical use of the neutron-emitting radionuclide ^{252}Cf was first proposed in 1965 by Schlea and Stoddard.[35] Schlea and Stoddard noted that early radiobiological studies of external neutron beam therapy demonstrated effectiveness in anoxic tumors that were typically resistant to conventional photon therapies. They also described the advantage of intracavitary and interstitial brachytherapy treatment over external neutron beam therapy, which includes higher radiation doses to healthy tissue.[35] The first medical source containing ^{252}Cf was described in 1967 and was modeled after a radium needle.[36]

Thousands of patients worldwide have been treated over the past 40 years with ^{252}Cf-based brachytherapy.[36] The mixed neutron and photon radiation has been shown to be particularly effective for large tumors and traditionally radio-resistant tumors, such as melanomas and late-stage cervical carcinomas. For example, Tacev *et al.* have reported increased survival rates (+16%, $p < 0.002$) and decreased relapse rates (-17%, $p < 0.0002$) using ^{252}Cf for the treatment of advanced cervical carcinoma with twelve years post treatment follow-up in comparison to conventional treatment.[37] The increased effectiveness is attributed to a number of radiological characteristics of neutrons, such as increased relative biological effectiveness (RBE), decreased oxygen effect, and decreased cell-cycle dependence. In the United States, Yosh Maruyama M.D. treated many disease sites and published nearly one hundred clinical papers on the subject before his death in 1995. Consider **ref. 36** for a detailed overview of medical applications of ^{252}Cf brachytherapy and summary of clinical results for head and neck, gynecological, skin, rectal, esophageal, prostate, and brain tumors, among others.

Brachytherapy dosimetry for ^{252}Cf sources was aggressively pursued in the early 1970s once medical sources were available.[38-40] Calculations by Krishnaswamy used MC methods to determine a point source model for four different source types, including the Applicator Tube (AT) source with source length L = 1.5 cm.[38] Each point source was subsequently used in a numerical integration to calculate the dose to points up to 5 cm along and away from the source. Neutron kerma factors were not reported, and the photon cross-sections of Storm and Israel[41] were employed. Colvett *et al.* followed with

measurements using paired ion chambers (tissue equivalent and Al) in a large volume of tissue equivalent liquid to simulate infinite scatter conditions. Measurements from 1 to 5 cm on the transverse plane agreed within 0.94 ± 0.02 to Krishnaswamy's calculations; however, the measurements did not agree favorably with other reported measurements.[39] Differences between measurements were attributed to differences in phantom size, which resulted in varying scatter conditions, and to differences in chamber or ^{252}Cf source calibration.[39,40] Windham *et al.* calculated dose distributions for ^{252}Cf sources using a one-dimensional discrete ordinates code, 21 energy groups, and neutron kerma factors published by Ritz *et al.*[40,42] Calculations by Windham *et al.* were in good agreement with the Krishnaswamy calculations (1.01 ± 0.03) and Colvett *et al.* measurements (0.97 ± 0.02) for $0.5 \leq r \leq 5.0$ cm on the transverse plane. Anderson reviewed these and six other publications (3 calculations and 3 measurements) in a 1973 review paper on ^{252}Cf dosimetry.[43] The measurements of Colvett *et al.* were recommended for ^{252}Cf, although, the Colvett *et al.* photon data were only recommended for AT-type sources. The calculations of Krishnaswamy for non-AT-type sources needle sources were the recommended alternative.[43] These data were reported as along-and-away tables up to 5 cm from the source center.

The most recent determinations of ^{252}Cf neutron dose distribution about a low-dose rate source were published by Yanch and Zamenhof in 1992[44] and by Rivard *et al.* in 2000.[30] Yanch and Zamenhof calculated along-and-away tables using MC methods for AT-type sources.[44] Rivard adapted the TG-43 formalism for a generalized source of variable active length and provided brachytherapy dosimetry parameters for the neutron dose component.[30]

To date, ^{252}Cf brachytherapy in the United States is applied using manually loaded, LDR sources delivering below 2 Gy h^{-1} to the prescription point during patient treatment.[36] Both manual loading and LDR treatment increases radiological risk to the brachytherapist and support personnel who must attend to patient needs during long treatment sessions. Considering these issues, there is an interest in employing ^{252}Cf brachytherapy in the HDR regime. In addition, remote afterloading technology, which is well-documented and successful for HDR ^{192}Ir brachytherapy, is being considered for ^{252}Cf.[45] Measurement of the mixed-dose distribution about a clinical HDR ^{252}Cf source

has not been attempted because sources comparable in size and geometry to conventional HDR ^{192}Ir sources have only recently become possible due to advances in radiochemistry.[45] Furthermore, while radiochemistry now allows an HDR source containing > 1 mg/mm^3 of ^{252}Cf, one has not been constructed.

1.1.4 Radiological Protection

Brachytherapy presents unique radiological protection concerns for the brachytherapist. Marie Curie, one of the first people to regularly handle encapsulated radioactive sources, experienced radiation burns on her fingers after extended handling periods.[7] Henri Becquerel similarly experienced skin erythema and desquamation after carrying a few tenths of a gram of radium chloride in a glass tube in his pocket for six hours. After noting a less intense reaction from carrying the source for one hour, he repeated the experiment by placing the source in a 5 mm-thick lead capsule and noting that the shielded source needed significantly more time to produce a biological effect.[46] Many of the early experimenters and clinicians died as a result of their repeated radiation exposures.

Until the development of remote afterloading technology, brachytherapy procedures required manual loading or placement of sources into treatment position. These placed the brachytherapist at risk for repeated radiobiological harm. Thus, tools were developed to increase the distance or to incorporate shielding between clinicians and brachytherapy sources. Furthermore, LDR treatments could have durations exceeding one week that posed a radiological risk to ancillary clinical staff, such as nurses, who were attending to patient needs. Generally, these concerns were addressed by using patient rooms in relatively remote locations with portable, rolling shields to reduce radiation levels outside the room.

However, the methods that were effective for traditional photon-based brachytherapy would not provide adequate protection for neutron-based brachytherapy using ^{252}Cf. While Pb shields would be effective against the photon emissions from a ^{252}Cf source, Pb does not notably attenuate or moderate neutrons. Maruyama *et al.* noted that early ^{252}Cf treatment centers utilized a treatment vault that was originally designed for megavoltage energy photon beams.[36] At one facility in the Czech Republic, a vault designed for a ^{60}Co treatment unit was augmented with a 24-cm thick layer of borated

polyethylene before being used for ^{252}Cf therapy.[47] Borated polyethylene is an effective neutron shield because the hydrogen component in polyethylene moderates the neutrons, increasing their probability of absorption by boron, which has a high neutron-capture cross section.

During HDR ^{252}Cf therapy, treatment vaults will be subjected to extremely high neutron fluence. One mg of ^{252}Cf emits 2.314×10^9 ($\pm$ 2%) neutrons s^{-1} and 1.3×10^{10} ($\pm$ 4%) photons s^{-1}, which correlate to approximately 0.28 Gy h^{-1} and 0.14 Gy h^{-1} at 1 m from an unshielded source.[45,48] As such, it is possible for the instantaneous dose rate outside of the treatment vault to exceed regulatory limits. Current regulations specifiy maximum permissible radiation doses to a member of the public at 0.02 mSv in one hour and 0.1 mSv in one year.

Shielding calculations for ^{252}Cf emissions were published in technical reports of the Savannah River Laboratory by Hootman (1970) and by Hootman and Stoddard (1971).[48,49] These shielding analyses solved a one-dimensional Boltzman equation in a slab, sphere or cylindrical geometry using discrete ordinates and anisotropic scattering.[48] In addition, the calculations included RBE factors [sic] to convert absorbed dose (rad or Gy) to equivalent dose (rem or Sv). Historical RBE values (1957) were employed because radiation weighting factors were not available at the time. The International Council for Radiation Protection (ICRP) recommended radiation weighting factors for dose equivalent calculations in Report 60 (1990).[50]

1.2 Thesis statement

1.2.1 PHOTON DOSIMETRY

As noted in **section 1.1.2**, the AAPM TG-43 brachytherapy dosimetry formalism determines dose distributions in a semi-infinite volume of liquid water, *i.e.*, dose calculations assume negligible losses due to energy escape from the phantom. Unfortunately, this assumption rarely simulates patient geometry. Similarly, differences between energy absorption in water and other media have been studied with corrections implemented for external beam treatments. However, corrections are not used for brachytherapy.

These concepts are explored in **Chapter 2**, where dose distributions from virtual and commercial photon-emitting brachytherapy sources were calculated using MC methods and compared to the current brachytherapy dosimetry formalism in AAPM TG-43U1 Report. While the TG-43U1 report describes commercial low-energy photon-emitting ^{125}I and ^{103}Pd sources, the formalism was applied to a number of radionuclide sources spanning a wide energy range. Furthermore, mono-energetic sources were employed to identify generalizable characteristics in photon-based brachytherapy dosimetry parameters.

These observations were subsequently applied to eye plaque brachytherapy using commercial ^{103}Pd, ^{125}I, and ^{131}Cs brachytherapy sources. Gold-alloy plaques provide significant attenuation of emitted radiation, but existing treatment planning systems exclude these effects. Furthermore, material inhomogeneities in plaque components have been shown to perturb single-seed ^{125}I dose distributions by as much as 10% at clinically relevant distances.[51] MC-based treatment simulations described in **section 2.2** demonstrate changes in dose distributions for fully-loaded eye plaques using common low-energy radionuclide sources. Correction factors accounting for these effects were derived for conventional treatment plans.

1.2.2 NEUTRON DOSIMETRY

Chapter 3 extends the photon-specific effects described in **Chapter 2** to neutron-emitting sources. Thus, generalizable characteristics of neutron brachytherapy were derived and compared to the dosimetry formalism of AAPM TG-43U1 Report in **section 3.1**. Distinctions between dose distributions obtained for photon and neutron brachytherapy were established towards a better understanding of the photon contribution in neutron-based brachytherapy. Furthermore, recommendations to future dosimetry investigators were presented.

These analyses were broadened to a theoretical HDR ^{252}Cf source in **section 3.2**. As discussed in **section 1.1.3**, HDR ^{252}Cf sources are still in development. However, comparisons were made between LDR AT-type sources and a theoretical HDR source in preparation for neutron-based HDR treatment.

The clinical impact of partial scatter conditions during surface plaque brachytherapy was examined for comparison to the semi-infinite water phantom assumed

by the AAPM TG-43U1 dosimetry formalism in **section 3.3**. MC calculations were performed for comparison to treatment plans calculated using conventional brachytherapy treatment planning software in support of a ^{252}Cf brachytherapy clinical trial.

1.2.3 SHIELDING CONSIDERATIONS

In further support of neutron-based brachytherapy using HDR ^{252}Cf, the shielding requirements for mg quantities of ^{252}Cf were evaluated using MC methods in **Chapter 4**. Shielding properties of concrete, barite concrete, lead, water, polyethelyene, and borated polyethylene were evaluated for thicknesses up to 1 m in **section 4.1**. MC calculations employed three dimensional radiation transport modeling, modern cross-section libraries, and contemporary radiation weighting factors.

Finally, a linear accelerator vault at Tufts-New England Medical Center in Boston, MA was assessed for shielding an HDR-equivalent ^{252}Cf source in **section 4.2**. MC calculations were performed in conjunction with ionization chamber, proportional counter, and track-etch detector measurements of a ^{252}Cf neutron radiography source (> 1 mg) positioned where treatment would occur within the accelerator vault. The resulting measurements were utilized to estimate limitations on patient throughput due to radiation exposure to personnel and to the public during HDR ^{252}Cf treatment assuming conventional permissible exposures.

1.3 Data, reference, and publication heritage

Segments of this dissertation are reprinted or reproduced from previously published materials. These materials include two peer-reviewed publications, one peer-reviewed abstract, two peer-reviewed papers from a conference proceeding, and one manuscript submitted for publication.

Section 2.1 is reprinted from: Melhus and Rivard "Approaches to calculating AAPM TG-43 brachytherapy dosimetry parameters for ^{137}Cs, ^{125}I, ^{192}Ir, ^{103}Pd, and ^{169}Yb sources" in *Medical Physics* Vol. 33, pgs. 1729-1737 (© 2006 by the AAPM).[52]

Section 2.2 is reproduced from the manuscript "COMS eye plaque brachytherapy dosimetry for ^{103}Pd, ^{125}I, and ^{131}Cs" by Melhus and Rivard, submitted (07-853) to *Medical Physics* in December 2007.[53]

Section 3.2 is from Melhus *et al.* "Clinical brachytherapy dosimetry parameters and mixed-field dosimetry for a high dose rate Cf-252 brachytherapy source" in The Monte Carlo method: Versatility unbounded in a dynamic computing world published by the American Nuclear Society (ANS; © 2005 by the ANS, La Grange Park, IL).[54]

Section 3.3.1 is from Melhus and Rivard "Monte Carlo validation of clinical brachytherapy dosimetry under partial scatter conditions for neutron-emitting sources" in *Medical Physics* Vol. 34, pg. 2330 (© 2007 by the AAPM).[55]

Section 4.1, "Storage safe shielding assessment for a HDR californium-252 brachytherapy source," by Melhus *et al.* is also reprinted from The Monte Carlo method: Versatility unbounded in a dynamic computing world (© 2005 by the ANS, La Grange Park, IL).[56]

Section 4.2 by Melhus *et al.* titled "Shielding evaluation of a medical linear accelerator vault in preparation for installing a high dose rate ^{252}Cf remote afterloader" was published in *Radiation Protection Dosimetry* Vol. 113, pgs. 428-437 (© 2004 by C.S. Melhus).[57]

All works were used with permission from the copyright owners.

2 PHOTON DOSIMETRY

2.1 Approaches to calculating AAPM TG-43 brachytherapy dosimetry parameters for ^{137}Cs, ^{125}I, ^{192}Ir, ^{103}Pd, and ^{169}Yb sources[†]

2.1.1 ABSTRACT

Underlying characteristics in brachytherapy dosimetry parameters for medical radionuclides ^{137}Cs, ^{125}I, ^{192}Ir, ^{103}Pd, and ^{169}Yb were examined using Monte Carlo methods. Sources were modeled as un-encapsulated point or line sources in liquid water to negate variations due to materials and construction. Importance of phantom size, mode of radiation transport physics - i.e., photon transport only (MODE P) or coupled photon:electron transport (MODE PE), phantom material, volume averaging, and Monte Carlo tally type were studied. For non-infinite media, g(r) was found to degrade as r approached R, the phantom radius. MCNP5 results were in agreement with those published using GEANT4. Brachytherapy dosimetry parameters calculated using coupled photon:electron radiation transport simulations did not differ significantly from those using photon transport only. Radial dose from low-energy photon-emitting radionuclides ^{125}I and ^{103}Pd were sensitive to phantom material by upto a factor of 1.4 and 2.0, respectively, between tissue-equivalent materials and water at r = 9 cm. In comparison, high-energy photons from ^{137}Cs, ^{192}Ir, and ^{169}Yb demonstrated ± 5% differences in radial dose between water and tissue-substitutes at r = 20 cm. Similarly, volume-averaging effects were found to be more significant for low-energy

[†] Reproduced from: C. S. Melhus and M. J. Rivard, "Approaches to calculating AAPM TG-43 brachytherapy dosimetry parameters for ^{137}Cs, ^{125}I, ^{192}Ir, ^{103}Pd, and ^{169}Yb sources," Med. Phys. **33**, 1729-1737 (2006).

radionuclides. When modeling line sources with $L \leq 0.5$ cm, the 2-D anisotropy function was largely within ± 0.5% of unity for ^{137}Cs, ^{125}I, and ^{192}Ir. However, an energy and geometry effect was noted for ^{103}Pd and ^{169}Yb, with $_{Pd\text{-}103}F(0.5,0°) = 1.05$ and $_{Yb\text{-}169}F(0.5,0°) = 0.98$ for L = 0.5 cm. Simulations of monoenergetic photons for L = 0.5 cm produced energy-dependent variations in $F(r,\theta)$ having a maximum value at 10 keV, minimum at 50 keV, and ~ 1.0 for higher-energy photons up to 750 keV. Both the F6 cell heating and *F4 track-length estimators were employed to determine brachytherapy dosimetry parameters. F6 was found to be necessary for g(r), while both tallies provided equivalent results for $F(r,\theta)$.

2.1.2 INTRODUCTION

For brachytherapy dosimetry calculations using radiation transport codes, TG-43U1 makes a number of "good practice" recommendations.[20] These nine recommendations include allowing for adequate backscatter material, utilizing modern photon cross-sections, and maintaining volume-averaging effects below 1%, among others. Regardless of the TG-43U1 guidance, the dosimetry investigator is allowed considerable flexibility in designing and conducting both simulations and measurements, resulting in notable methodology variations between authors. These variations are clearly evidenced in Appendix A of TG-43U1, which includes a discussion of the number of authors and publications dedicated to an individual seed design (manufacturer and model), and each publication contains investigator-specific methodologies and approaches. Additional complexity is added as the scope extends to multiple seed models, each with a unique subset of contributing dosimetry investigators and related methodologies that change over time in response to new discoveries, other publications, and AAPM recommendations.

Furthermore, specific dosimetry parameters have garnered considerable interest in the brachytherapy dosimetry community during recent years.[58-63] For example, dosimetry investigators have suggested both adding complexity[58] and simplifying the geometry function, $G(r,\theta)$,[60] towards improving brachytherapy dosimetry. The AAPM TG-43U1 currently recommends either a line- or point-source approach to approximate all commercially available brachytherapy seeds. As much of the recent interest relates to

derivation of $G(r,\theta)$, the AAPM published a clarification stressing the need for consistent application of a geometry function, rather than accurate representation of particle streaming behavior.[63]

Unlike $G(r,\theta)$, which is not a function of radionuclide energy spectrum and is purely mathematical, other AAPM TG-43U1 brachytherapy dosimetry parameters are determined by comparing absorbed dose measurements or calculations within a phantom. The brachytherapy dosimetry investigator must carefully model and sample the phantom to avoid introducing bias related to the radiation transport model or technique. Errors incurred through inappropriate technique usage can be magnified when dose distribution results are processed using the dosimetry formalism because of the relative nature of the calculations.

Assuming further advances in computer processing capabilities, the current dosimetry formalism standard may eventually be abandoned in favor of direct MC-based brachytherapy dosimetry simulations,[64,65] though careful measurements will be needed to commission such a system. At present, the brachytherapy dosimetry formalism presented in the AAPM TG-43U1 report represents the current standard. Therefore, this publication provides reference brachytherapy dosimetry parameters for a variety of un-encapsulated medical radionuclides using MCNP5. This goal will not only elucidate inherent characteristics of each individual source photon spectrum, but also provide reference data towards comparing with other MC-based brachytherapy dosimetry calculations. At the same time, the impact of phantom geometry, including backscatter and sampling volume effects, and phantom material will be explored for MCNP5.

2.1.3 Materials and Methods

Dose distributions from five radionuclides (^{137}Cs, ^{125}I, ^{192}Ir, ^{103}Pd, and ^{169}Yb) used for brachytherapy were modeled. The 2004 update to the AAPM TG-43 report included only low-energy photon emitting brachytherapy sources containing ^{125}I or ^{103}Pd.[20] This study employed the same formalism and extended it to high-energy photon sources (E_{AVG} > 50 keV) with a more energetic population of secondary particles. All photon energies were included in spectral characterization with the exception of those below 9 keV, because the average pathlength is < 0.2 cm in water. Photon and electron spectra for each

radionuclide were taken from the National Nuclear Data Center (NNDC).[33] Furthermore, AAPM TG-43U1 recommended photon energy and emission frequencies for ^{125}I and ^{103}Pd and the ^{192}Ir spectrum of Glasgow and Dillman[66] were used in radiation transport simulations for comparison to results obtained using NNDC-published values.

Simulations were performed using version 5 of the MCNP Monte Carlo code (MCNP5) developed by Los Alamos National Laboratory.[67] The default MCNP5 photon cross-section library, p04, was applied, which is based upon Release 8 of ENDF/B-VI.[68] Computed results of cell particle fluence, energy fluence, and heating were obtained using the MCNP F4, *F4, and F6 tallies, respectively. These three tallies correspond to track length estimates in a cell of photon flux, product of photon flux with photon energy, and energy deposition, respectively. Source encapsulation was not included in any of the simulations in order to ascertain underlying characteristics of each radiation spectrum in materials of dosimetric interest and to eliminate manufacturer-specific effects due to source construction. Water was modeled using an atomic ratio of 2:1 for H:O and a mass density of 0.998 g cm^{-3} at standard temperature and pressure, 22°C and 101.325 kPa, respectively. Due to their low-energy photon emissions and subsequent rapid dose falloff, ^{103}Pd and ^{125}I results were excluded beyond 9 cm and 15 cm, respectively.[69]

2.1.3.1 Radial dose function

The radial dose function, g(r), was assessed for each radionuclide photon spectrum using an un-encapsulated point source in a spherical water phantom with R = 50 cm in radius, i.e., $_{X\text{-}A}g(r)_R$. where the prefix subscript denotes the radionuclide and the suffix subscript denotes the phantom radius. Concentric spheres were designed to create spherical shells in which MCNP5 tallies were computed, allowing calculation of g(r) at radial distances between 0.1 and 20 cm. Values of R were 5, 10, 15, 20, 25, 30, 35, 40, and 45 cm were used to assess full scatter conditions. While a smaller radius is generally representative of human anatomy, e.g., the R = 15 cm used by Daskalov et. al. for HDR ^{192}Ir calculations[29], $g(r)_{50}$ data is presented here. Varying the radial width of the sampling volume, *i.e.*, the thickness of the spherical shell, assessed the impact of volumetric averaging. Data were collected for 0.01, 0.02, 0.05, 0.1, 0.2, 0.3, 0.5, 1, and 2 cm thick shells, as well as for a variable thickness of 5% or 10% of the radial distance. The inner

and outer radii defining the sampling volume were equally displaced from the reported point of calculation. Volume averaging errors caused by non-zero voxel width were evaluated for ± 0.5% variation in g(r) by comparing results to the 0.01 cm-thick voxel. Simulations were also performed in breast tissue, muscle, soft tissue, and four-component soft tissue, as defined in ICRU 44,[70] and presented by NIST,[71] to compare with the in-water calculations required by TG-43U1.

Source emissions were modeled as photon and electron spectra for all five radionuclides. To determine the impact of simplifying radiation transport calculations for the five photon source spectra, photon-only (MODE P) and coupled photon:electron (MODE PE) calculations were performed. Furthermore, simulations of electrons emitted following β-decay or electron capture, including auger electrons, were performed using the default MCNP5 electron transport mode (par = 3) to evaluate whether electron-only transport (MODE E) or secondary photons generated by electrons (MODE PE) contributed to total radial dose deposition. The algorithm used for default electron transport calculation is subject to non-physical energy effects, see for example **Ref. 72**, and may not accurately reproduce electron dose distributions. As such, comparisons of electron and photon transport are made on a relative basis to show order-of-magnitude results.

The F6 energy deposition tally was evaluated by transporting 0.001 to 10 MeV photons from a point source through a sphere of liquid water(R = 15 cm) and sampling within a thin sampling volume (spherical shell) 0.01 cm from the source. Using the tally energy card (En), energy bins were established with an average energy bin width of 7% ± 6% (± 1 s.d.) of the bin energy. A ratio of F6 and *F4 results for each energy bin was taken to evaluate energy absorption coefficients ($\mu_{en}\ \rho^{-1}$) employed when using MCNP5. The dose rate per mCi was calculated from F6 results at (r_o,θ_o) to allow comparison of radial dose data in a non-normalized manner. The normalized and balkanized nature of TG-43U1 dosimetry parameters, such as g(r), precludes clear understanding of absolute dose rates. Thus, the dosimetry investigator may use dose rate values for additional comparison and benchmarking. It is important to note, however, that the AAPM discourages use of apparent activity or exposure rate constants that describe dose rate as a function of source radioactivity.[20]

The statistical uncertainties for 10^7 starting particles were < 0.05% at r = 1 cm for all radionuclides for a spherical shell with radial thickness of 0.01 cm. At r = 10 cm, statistical uncertainties were ≤ 0.06% for high-energy sources and 0.2% for ^{125}I. For ^{103}Pd, statistical uncertainties were 0.7% and 0.1% for 10^7 and $5x10^8$ starting particles, respectively. At r = 20 cm, statistical uncertainties were ≤ 0.1% for ^{137}Cs, ^{192}Ir, and ^{169}Yb.

2.1.3.2 MC F(r,θ) analysis

The 2-D anisotropy function F(r,θ) was calculated for six active lengths (0, 0.1, 0.2, 0.3, 0.4, and 0.5 cm) in a liquid water phantom of R = 25 cm for low-energy and R = 40 cm for high-energy radionuclides. Monoenergetic photons were generated for active lengths of 0.1, 0.3, and 0.5 cm at 10, 20, 30, 50, 75, 100, 200, 300, 500, and 750 keV for comparison to the radionuclide energy spectra. Line sources were approximated using a cylinder with radius 10^{-6} cm. A series of intersecting concentric spheres and cones were designed to provide 1° angular resolution about the long axis of the source. Data were calculated at 11 radial distances between 0.5 and 12 cm, and two voxel thickness models were examined – a fixed radial width of 0.02 cm and variable width determined using 10% of the radial distance at the point of calculation.

Monte Carlo simulations were performed using MODE P transport. A total of 5 x 10^7 starting particles were utilized for all radionuclides, with the exception of ^{103}Pd that required 2.5 x 10^8 starting particle histories for improved statistics. The concentric cones result in sampling volumes that are cylindrically located about the long axis of the source. As a result the minimum statistical uncertainty occurs on the transverse plane (θ = 90°) and the maximum uncertainty is located on the long axis of the source (θ = 0° and 180°), where the sampling volume is approximately 450 times smaller. At a radial distance of 1 cm from a point source and a bin-width of 10% of the radial distance, the statistical uncertainties at 5° and 85° were 0.5% and 0.2% for ^{137}Cs; 0.5% and 0.1% for ^{125}I; 0.5% and 0.2% for ^{192}Ir; 0.3% and 0.1% for ^{103}Pd; and, 0.5% and 0.2% for ^{169}Yb, respectively. At a radial distance of 10 cm from a point source and a bin-width of 10% of the radial distance, the statistical uncertainties at 5° and 85° were 0.5% and 0.1% for ^{137}Cs; 1.4%

and 0.4% for ^{125}I; 0.4% and 0.1% for ^{192}Ir; 3.3% and 1.0% for ^{103}Pd; and, 0.4% and 0.1% for ^{169}Yb, respectively.

In addition, data from the transverse plane were taken to determine $g_L(r)$ for each active length and radionuclide, and a comparison of the point source (L = 0 cm) result was made to the values calculated using concentric spheres. In this way, results obtained using 4π geometry were compared to those employing the relatively small sampling volumes introduced using concentric cones as described above.

2.1.4 RESULTS AND DISCUSSION

2.1.4.1 Phantom size

The effect of phantom size is shown in **Figure 2.1.1** as the ratio of $g_p(r)$ calculated for a given phantom thickness and $g_p(r)$ for a 50 cm radius phantom. For all radionuclides at any distance, g(r) for R < 50 cm was less than or equal to $g(r)_{50}$. Furthermore, as r approached R, the ratio of $g(r)/g(r)_{50}$ rapidly diminished from unity. This decrease became more pronounced as r increased due to the increased proportion of scatter dose compared to primary dose. Similarly, this increase was more pronounced and gradual for sources having higher average photon energy (^{137}Cs, ^{192}Ir, ^{169}Yb) in comparison to lower average energy sources (^{125}I and ^{103}Pd).

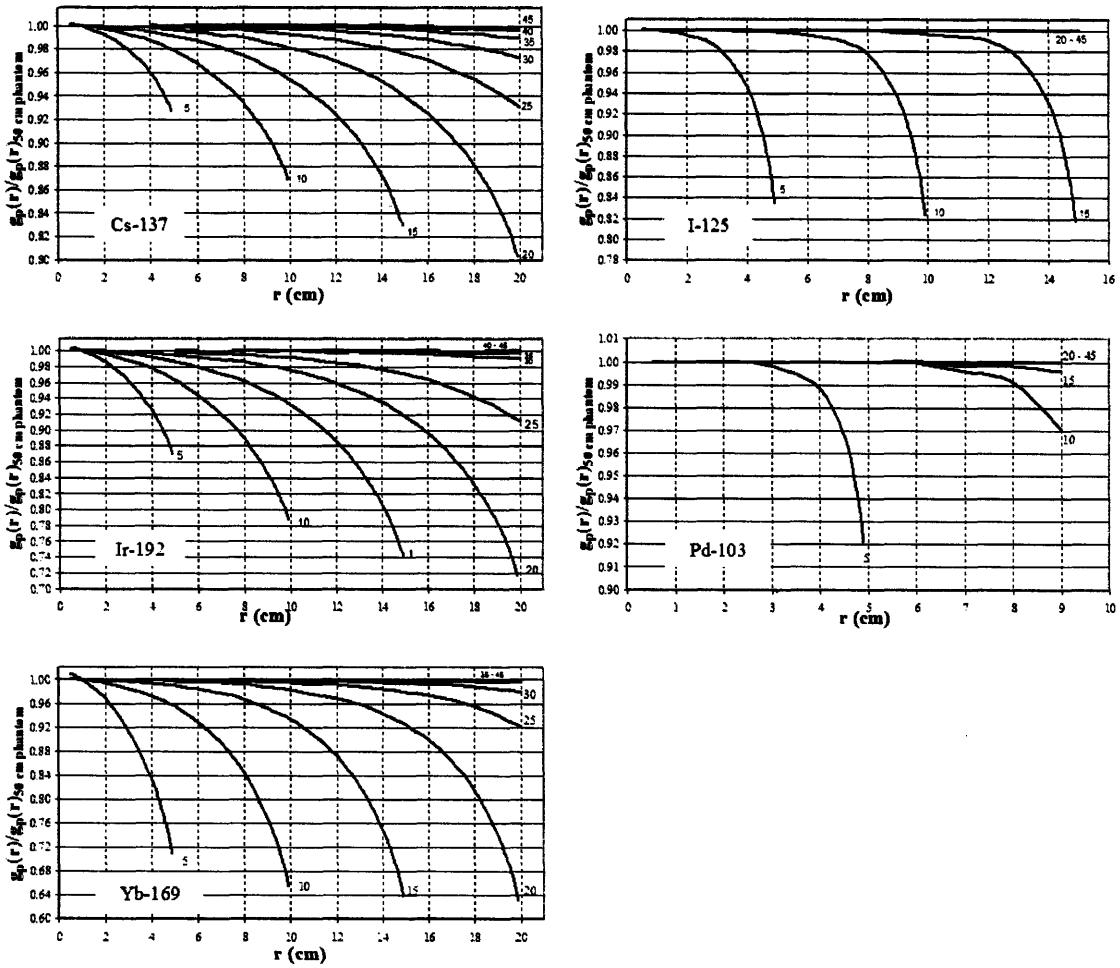

Figure 2.1.1: Comparison of g(r) values calculated for a given phantom size, R, compared to R = 50 cm, which is assumed to provide full scatter conditions. Data for ^{137}Cs, ^{125}I, ^{192}Ir, ^{103}Pd, and ^{169}Yb include curves for R = 5, 10, 15, 20, 25, 30, 35, 40, and 45 cm shown from left to right. Curves for large phantom sizes within statistical uncertainty of unity, *e.g.*, R = 45 and 40 cm, are not discernable. Note the variation in the x-ordinate for the low-energy radionuclides ^{125}I and ^{103}Pd.

Similarly, Pérez-Calatayud *et al.* determined phantom sizes needed to provide full scatter conditions for ^{137}Cs, ^{125}I, ^{192}Ir, and ^{103}Pd using the GEANT4 Monte Carlo code.[73] Although they did not report the photon cross-sections utilized in their study, reasonable comparisons may be made between results using the GEANT4 and MCNP5 Monte Carlo codes. Pérez-Calatayud *et al.* observed full scatter conditions within 0.5% for $_{I\text{-}125}g(10)_{15}$ and $_{Pd\text{-}103}g(10)_{15}$. Using MCNP5 in this study, $_{I\text{-}125}g(10)_{15}/_{I\text{-}125}g(10)_{50} = 0.997 \pm 0.001$ and $_{Pd\text{-}103}g(10)_{15}/_{Pd\text{-}103}g(10)_{50} = 0.989 \pm 0.002$. This study obtained $_{Cs\text{-}137}g(20)_{40}/_{Cs\text{-}137}g(20)_{50} = 0.996 \pm 0.001$ and $_{Ir\text{-}192}g(20)_{40}/_{Ir\text{-}192}g(20)_{50} = 0.997 \pm 0.001$ which is in agreement with

Pérez-Calatayud *et al.* who noted full scatter conditions within 0.5% for $g(20)_{40}$ for both radionuclides. Excellent agreement was also obtained for ^{137}Cs and ^{192}Ir at all r and R, with differences < 0.3% between our results and those obtained by Pérez-Calatayud *et al.* We recommended $R \geq 40$ cm for ^{169}Yb to provide full scatter conditions (within 0.2%) for $r \leq 20$ cm.

2.1.4.2 MCNP5 F6 tally

The dosimetry investigator using MCNP5 has several cell or surface-based tally options to choose from. Volume-based tallies are preferred as they reduce the statistical uncertainties and improve the accuracy of MCNP5 simulations, though, the sampling volume must be sufficiently small to minimize differences in particle fluence and average photon path length within the cell. The *F4 tally, providing energy flux results in MeV cm^{-2}, can be converted to absorbed dose through application of appropriate $\mu_{en}\ \rho^{-1}$ coefficeints. However, the investigator is required to segment results into energy bins compatible with published $\mu_{en}\ \rho^{-1}$ coefficeints, or include a tally multiplier (FMn) card to convert results from MeV cm^{-2} to MeV g^{-1} in a direct fashion. Using F6 tally results and a radial voxel thickness of 0.01 cm, un-encapsulated g(r) in water for a point source is shown in **Table 2.1.1**. These reference data may be used to benchmark other radiation transport codes and ensure accurate derivation of brachytherapy dosimetry parameters between other sampling geometries and radiation transport codes.

Table 2.1.1: Radial dose functions for un-encapsulated point sources in a 50 cm-radius liquid water phantom using the MCNP5 F6 cell-heating tally. Based upon the number of histories simulated and the MCNP5 coefficient of variation in the tally result, all results have a maximum statistical uncertainty of 0.1%. The tally volume at each distance was a spherical shell of radial thickness 0.01 cm centered on the specified r. Italicized data for ^{125}I and ^{103}Pd indicate larger uncertainties attributed to substantive attenuation.

	$g_P(r)$				
r [cm]	^{137}Cs	^{125}I	^{192}Ir	^{103}Pd	^{169}Yb
0.1	1.006	1.004	0.988	1.469	0.874
0.2	1.006	1.018	0.990	1.429	0.890
0.3	1.005	1.025	0.992	1.381	0.905
0.5	1.004	1.030	0.994	1.274	0.934
0.8	1.002	1.017	0.998	1.107	0.974
1.0	1.000	1.000	1.000	1.000	1.000
1.5	0.995	0.939	1.005	0.761	1.056
2.0	0.990	0.862	1.009	0.571	1.103
2.5	0.985	0.780	1.012	0.424	1.142
3.0	0.979	0.699	1.014	0.313	1.172
3.5	0.972	0.622	1.015	0.229	1.197
4.0	0.966	0.549	1.015	0.168	1.213
4.5	0.958	0.482	1.014	0.123	1.224
5.0	0.951	0.422	1.013	0.0902	1.229
6.0	0.936	0.319	1.006	0.0483	1.226
7.0	0.920	0.239	0.997	0.0261	1.206
8.0	0.903	0.179	0.984	0.0142	1.175
9.0	0.885	0.132	0.968	0.0080	1.135
10.0	0.866	0.0972	0.949	*0.0046*	1.088
11.0	0.847	0.0719	0.927	*0.0029*	1.035
12.0	0.826	0.0527	0.903	*0.0019*	0.983
13.0	0.805	0.0386	0.876	*0.0013*	0.927
14.0	0.784	0.0283	0.848	*0.0010*	0.871
15.0	0.763	0.0207	0.817	*0.0008*	0.816
16.0	0.740	*0.0152*	0.785	*0.0007*	0.763
17.0	0.717	*0.0112*	0.751	*0.0006*	0.712
18.0	0.695	*0.0082*	0.715	*0.0006*	0.6616
19.0	0.672	*0.0061*	0.677	*0.0005*	0.6152
20.0	0.649	*0.0044*	0.638	*0.0005*	0.5705

Towards determining these parameters, the F6 tally with appropriate units of MeV g^{-1} is recommended for simulating radiation transport using MCNP because it directly correlates with absorbed dose rate without using potentially inconsistent μ_{en} ρ^{-1}

coefficeints. The F6 tally, generating cell-heating data, incorporates MCNP5 $\mu_{en}\ \rho^{-1}$ values that were evaluated by taking the ratio of F6 and *F4 tally results. Comparison of MCNP5-derived values and $\mu_{en}\ p^{-1}$ values published by NIST[71] gives an average of 0.999 ± 0.002 (± 1 s.d.) for photon energies between 15 keV and 1.5 MeV. Thus, the F6 tally now adequately estimates absorbed dose rates for conventional photon-emitting brachytherapy sources and obviates the need to use and modify alternate tallies.

2.1.4.3 Radial dose function

Williamson calculated g(r) with the MCPT radiation transport code for an un-encapsulated ^{125}I point source in water,[74] using a modified version of the DLC-146 photon cross-sections released in 1989. Comparison of the ^{125}I results in this study to Williamson show agreement within 0.5% up to 7 cm, followed by a rapid divergence to 1.8% at 11 cm and 8.2% at 14 cm. The primary difference between this study and Williamson is due to disparity in phantom size. Repeating the simulation described above using an R = 15 cm liquid water phantom resulted in a maximum disagreement of 1.3% at 14 cm.

When assessed using *F4 tallies, differences between MODE PE and MODE P transport to account for the dosimetric impact of electrons for $0.1 \leq r \leq 20$ cm was < 0.2% for ^{137}Cs, < 0.1% for ^{192}Ir, and < 0.03% for ^{169}Yb. Thus, the proportion of dose contributed by electrons was less than 1:500 for these high-energy radionuclides. For low-energy sources such as ^{103}Pd and ^{125}I, electron contributions were < 1:3,000. Similarly, MODE PE and MODE E simulations of source electrons for the five radionuclides yielded inconsequential contributions to the total dose past 0.3 cm. For example, MODE PE simulations of source electrons from ^{169}Yb yielded *F4 results < 0.01% of the source photons from ^{169}Yb. Therefore, brachytherapy dosimetry calculations using MODE P simulation of the source photon spectrum is adequate towards determining dose distributions in water as recommended in TG-43U1. Justification for this simplification is required for other radiation sources having considerably different energies, or beyond the radial ranges studied.

For the three high-energy radionuclides, there was no variation in g(r) > ± 0.5% for voxel thickness of 0.2 cm and below and variable voxel thickness of 5% and 10% of

the radial distance similarly provided comparable (± 0.5%) g(r) data. For the low-energy radionuclides, there were few noticeable volume-averaging effects at large radial distances below a voxel thickness of 0.2 cm. ^{125}I exhibited < ± 0.5% variation for voxel thickness ≤ 0.05 cm, and ^{103}Pd demonstrated few minor deviations within ± 0.6% for voxel thickness of ≤ 0.1 cm. Variable voxel widths of 5% and 10% did not reproduce g(r) within ± 0.5% of that for 0.01 cm-thick shells for ^{125}I and ^{103}Pd due to the rapid radial dose falloff of these radionuclides. The maximum errors incurred using variable voxel width for low-energy radionuclides was 1.5% and the average difference was 0.2% ± 0.01% in comparison to the 0.01 cm-thick shells.

Comparisons of dose rates and $g_P(r)$ calculated using the spherical sampling space or the space divided into conics produced identical results within the statistical uncertainties for all radionuclides and r values examined. Thus, there were no artifacts from the MCNP software when dividing the space using different methods.

The calculated radial dose functions for L = 0.2, 0.3, and 0.4 cm were compared to the average of the value calculated for neighboring lengths (0.1 cm increments). For example, $g_L(r)$ calculated from L = 0.2 cm $F(r,\theta)$ values was compared to the average of $g_L(r)$ calculated from L = 0.1 cm and L = 0.3 cm. For ^{137}Cs, ^{192}Ir, and ^{169}Yb, the average of the neighboring values produced $g_L(r)$ data that were within 0.5% of the calculated one for all radial distances evaluated. The low-energy radionuclides provided interpolated $g_L(r)$ values within 0.8% for ^{125}I and within 1.2% for ^{103}Pd of the calculated values. Thus, radial dose function data for non-integer active lengths can be closely interpolated from calculated values. Additional work is required, however, to determine if $g_L(r)$ can be appropriately extrapolated to smaller or larger active lengths than those calculated.

Table 2.1.2 shows the absolute dose rates in water per contained mCi of radionuclide at r_o and θ_o for the five radionuclides. In addition, the ratio of the dose rate in each tissue-model to liquid water is also provided. The $(\Gamma_\delta)_\chi$ values in the original TG-43 report[10] can be compared to dose rates calculated in this study; however, significant differences in the photon spectra and calculation methodologies are present. Ratios of 0.702, 1.105, and 1.001 were obtained for ^{103}Pd, ^{192}Ir, and ^{125}I, respectively, by comparing **Table 2.1.2** data to TG-43 values.

Table 2.1.2: Dose rate per contained mCi of activity in water at r_0 for each radionuclide for the point source approximation. Also shown is the ratio of the dose rate in materials of dosimetric interest (from **Refs. 70** and **71**) to that in liquid water.

	$\dot{D}(r_0,\theta_0)$	${}_X\dot{D}(r_0,\theta_0) \,/\, {}_{water}\dot{D}(r_0,\theta_0)$			
	[cGy h^{-1} mCi^{-1}]	Breast	muscle	soft tissue	4-component tissue
Cs-137	3.153	0.992	0.991	0.991	0.989
I-125	1.321	0.852	1.016	1.018	0.942
Ir-192	4.541	0.993	0.992	0.992	0.990
Pd-103	0.910	0.898	0.981	0.977	0.966
Yb-169	1.996	0.936	1.014	1.017	0.967

Comparison of g(r) calculated in four materials of dosimetric interest to g(r) in liquid water is shown in **Figure 2.1.2** for ^{137}Cs, ^{125}I, ^{192}Ir, ^{103}Pd, and ^{169}Yb. There were notable variations in g(r) at large radial distances for the low-energy photon brachytherapy sources, ^{125}I and ^{103}Pd. Factor of 2 differences in g(r) between water and ICRU 44 breast tissue were present for ^{103}Pd at a depth of 9 cm, and g(r) for ICRU muscle and soft tissue were approximately 30% below that in water at a depth of 9 cm for both ^{125}I and ^{103}Pd. Conversely, high-energy ^{137}Cs and ^{192}Ir exhibited only a 4% reduction of g(r) in ICRU muscle and soft tissue in comparison to liquid water at a penetration of 20 cm. Generally, ^{169}Yb was more sensitive to phantom material in comparison to ^{137}Cs or ^{192}Ir. At 10 cm, g(r) in the four tissue compositions studied was approximately within ± 1% of g(r) in water for ^{137}Cs and ^{192}Ir, but differences increased to ± 5% for ^{169}Yb.

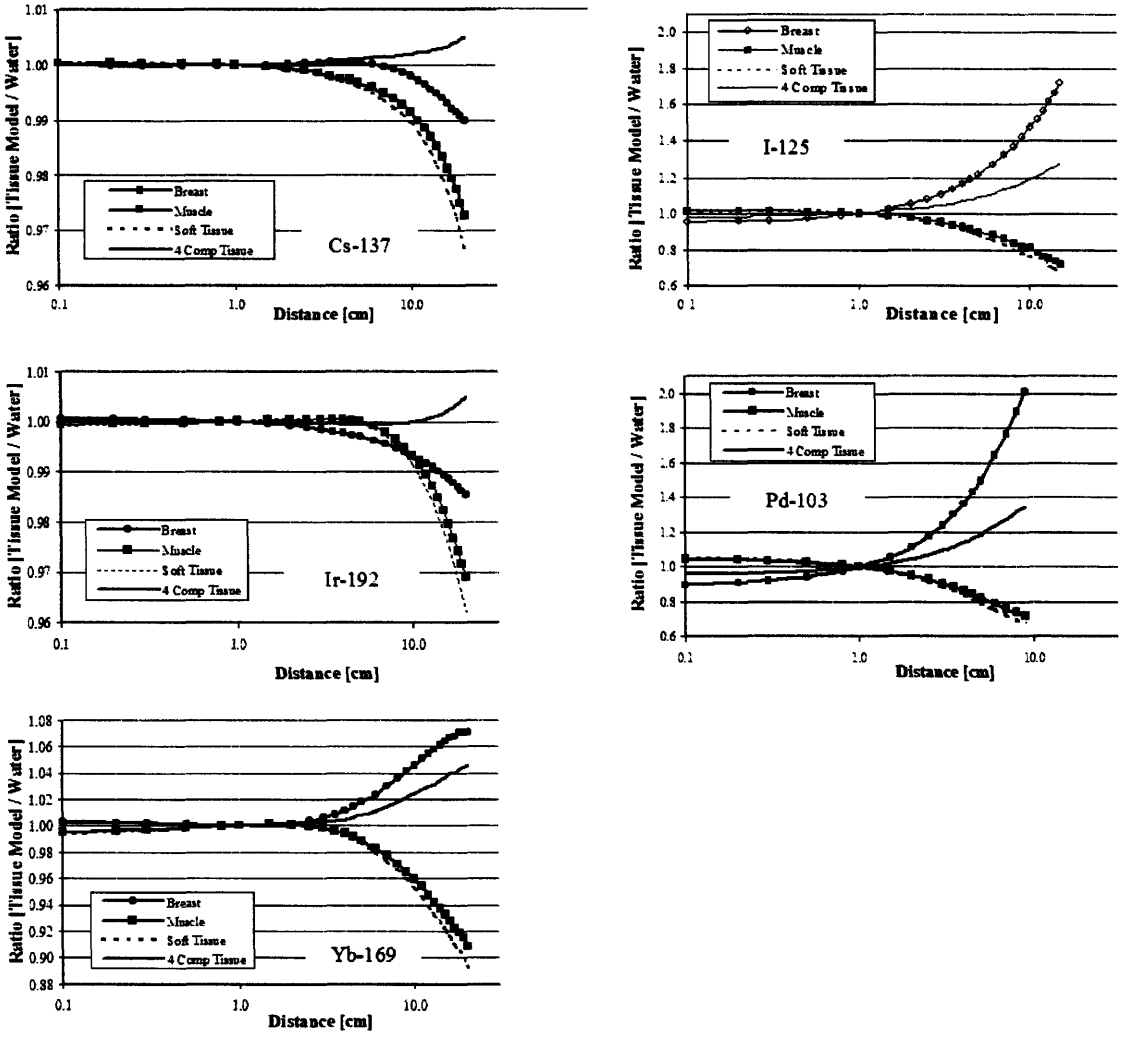

Figure 2.1.2: Comparison of g(r) calculated in four tissue substitutes to g(r) calculated in liquid water for ^{137}Cs, ^{125}I, ^{192}Ir, ^{103}Pd, and ^{169}Yb. Because low-energy photons are strongly attenuated through transport in neutral density material, the ^{125}I and ^{103}Pd photons exhibit the greatest difference between g(r) in tissue and in liquid water. Of the three high-energy sources, ^{169}Yb is the most strongly affected by transport in non-water media.

Reniers used MCNP4C and the EPDL97 cross-section library to study the impact of tissue composition on brachytherapy dosimetry parameters for low-energy photon emitting radionuclides using the IBt seed design.[75] Differences of 10% and 15% at a depth of 5 cm in muscle for ^{125}I and ^{103}Pd were reported by Reniers, while this study yielded differences of 9.7 ± 0.2% and 17.7 ± 0.3%, respectively. Similarly, Reniers

noted that g(5) for ^{103}Pd in water was underestimated by up to 50% in comparison to breast tissue, an effect also observed in this study with $_{water}g(5)/_{breast}g(5)$ = 67% using a differently expressed ratio. Thus, our observations of bare point sources were supported by Reniers' findings for low-energy radionuclides in a specific seed design, and we agree that advances in brachytherapy source dosimetry should incorporate tissue composition to better reflect non-trivial differences that may occur, especially for low-energy photon-emitting brachytherapy sources.

Incorporating TG-43U1 recommended photon spectra for ^{125}I and ^{103}Pd resulted in MCNP5 F6 tally results within 0.1% and 0.8%, respectively, of those using the NNDC photon data for all radii. The difference in dose rates for ^{125}I are within the statistical uncertainties (0.5% max), and differences for ^{103}Pd are likely due to the more detailed NNDC photon spectra (14 vs 8 lines above 10 keV) with slightly different intensities. Furthermore, normalized dose rate values such as using g(r) computed with the TG-43U1 photon data were on average < 0.03% different for ^{125}I and <0.3% different for ^{103}Pd in comparison to the results in **Table 2.1.1**. Radiation transport calculations using the NNDC photon spectrum and that of Glasgow and Dillman provided similarly comparable g(r) data for ^{192}Ir. Differences in F6-based dose rates using NNDC data or Glasgow and Dillman photon spectra were –1.6% at 0.1 cm, increased to +1.7% at 1 cm, and were approximately +1.9% to r = 20 cm. These tally ratios correspond to $_{Ir\text{-}192}g(r)$ ratios of -3.2% at 0.1 cm, -0.7% at 0.5 cm, and < 0.3% from 0.8 cm to 20 cm. As such, the NNDC ^{192}Ir photon spectrum with 25 β-decay photons and 16 electron capture photons (each including 6 characteristic x-rays) provides similar radiation transport results to the classic Glasgow and Dillman spectra having 36 β-decay photons (including 21 characteristic x-rays), 34 electron capture photons (including 21 characteristic x-rays), and 49 bremsstrahlung photons between 0.006 and 1.3 MeV.

While a coarse ^{192}Ir spectra is presented in the 1995 AAPM TG-43 report,[10] the AAPM has not yet recommended photon energy spectra for ^{137}Cs, ^{192}Ir, or ^{169}Yb to be used for Monte Carlo simulations of brachytherapy dose deposition. The widely used ^{192}Ir photon spectrum of Glasgow and Dillman could be evaluated and adapted by the AAPM for this purpose.[29,76,77] Other radionuclides, such as ^{137}Cs, have had a number of disparate sources cited for energy spectra used in radiation transport calculations and

would benefit from a standardized spectrum, as well as a review of the impact of each variation.[78-80]

2.1.4.1 F(r,θ) analysis

F(r,θ) data calculated using six effective lengths between 0.0 and 0.5 cm were largely within 0.5% of unity for $0.5 \leq r \leq 12$ cm for ^{137}Cs and ^{125}I. For L = 0.5 cm, $_{Ir\text{-}192}F(0.5,0^\circ)$ approached 1.01 for decreasing θ. A similar increase in F(r,θ) with decreasing θ was more strongly exhibited by ^{103}Pd for L = 0.5 cm, with $_{Pd\text{-}103}F(0.5,0^\circ)$ = 1.048, $_{Pd\text{-}103}F(1,0^\circ)$ = 1.031, and $_{Pd\text{-}103}F(1.5,0^\circ)$ = 1.023. The increase in F(r,θ) for small r and θ was similarly exhibited for active lengths of 0.4 and 0.3 cm with $_{Pd\text{-}103}F(0.5,0^\circ)$ = 1.031 and 1.017, respectively. ^{169}Yb exhibited the opposite effect, where F(r,θ) was reduced below unity for increased active length, decreased radius, and decreased polar angle with $_{Yb\text{-}169}F(0.5,0^\circ)$ = 0.984 and $_{Yb\text{-}169}F(1,0^\circ)$ = 0.992. As observed for $_{Pd\text{-}103}F(r,\theta)$, the magnitude of the deviation from unity for $_{Yb\text{-}169}F(r,\theta)$ was reduced along with reduction in L. All these results were statistically significant, and perturbations of the dose distribution beyond those accounted for by g(r) were not expected since the radionuclide distributions were un-encapsulated. Reported deviations in source anisotropy commonly occur along the source long-axes where end welds and other mechanical features are present. Thus, the $_{Yb\text{-}169}F(r,\theta) < 1.0$ result at $\theta = 0^\circ$ was notable because it occurred in the absence of a capsule, and the $_{Pd\text{-}103}F(r,\theta) > 1.0$ result was notable because commercial sources have not exhibited a dose rate on the long axis larger than that on the transverse plane for the same r value. Observed anisotropy effects, attributed to source photon absorption in the liquid water medium, suggest a relationship between L and photon energy.

Therefore, Monte Carlo simulations were performed using monoenergetic photons to further examine these observations. **Figure 2.1.3** shows F(0.5,θ) for ten energies between 10 and 750 keV for L = 0.5 cm. Considering the observed behavior of ^{169}Yb, with an average energy of 93.3 keV, the F(r,θ) data is consistent with the values depicted in **Figure 2.1.3** between 100 and 75 keV. A 5% difference in F(0.5,0°) between 20 and 30 keV photons was detected. ^{125}I with an average photon energy of 28.4 keV did

not exhibit the F(r,θ) effect observed for ^{103}Pd, because of the average photon energy of ^{103}Pd is 20.7 keV. In practice, the ^{103}Pd photon spectrum is hardened following transmission through the brachytherapy encapsulation, and F(r,θ) > 1.0 is not observed. For example, the two ^{103}Pd sources included in AAPM TG-43U1 have F(0.5,0°) ~ 0.68 for L_{eff} ~ 0.4 cm. Thus, the ^{103}Pd sources in TG-43U1 would have lower F(r, θ) values if not for the geometry effect on F(r,θ) noted in this study for a bare source. Additional work is needed to differentiate encapsulation effects from energy-related geometrical effects exhibited in **Figure 2.1.3**.

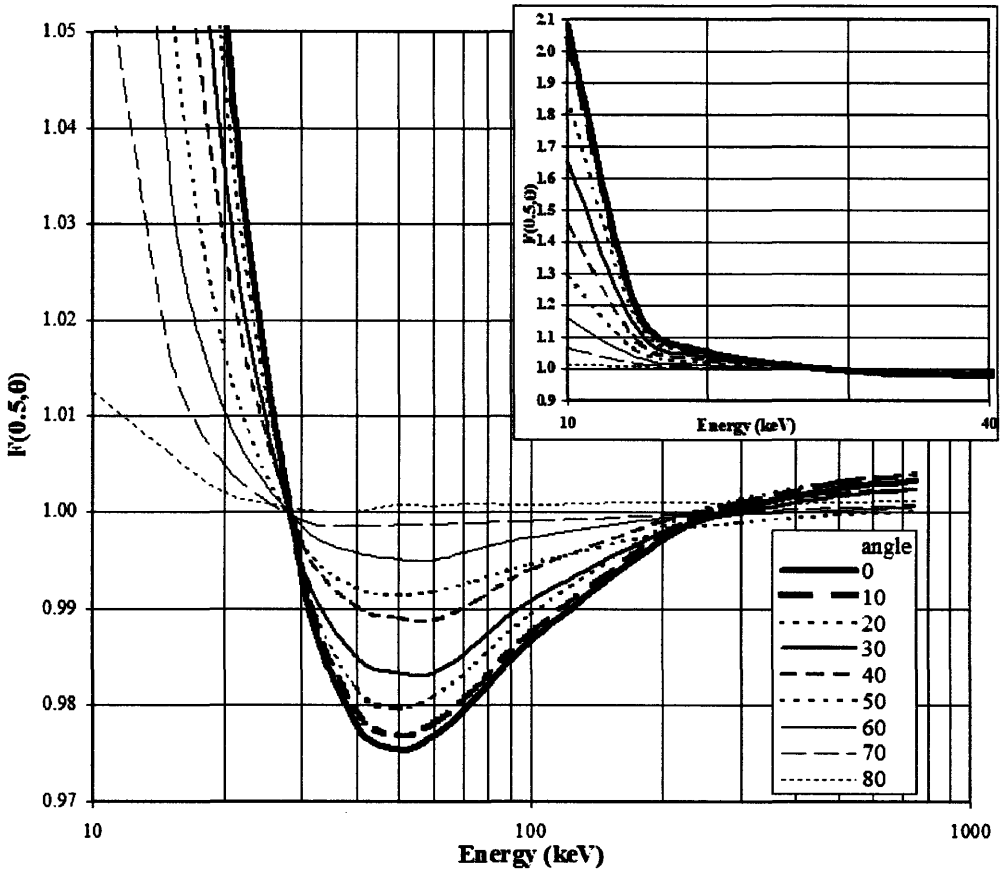

Figure 2.1.3: Mono-energetic photon F(r,θ) for an active length of 0.5 cm and a radial distance of 0.5 cm. F(r,θ) data were calculated using 10, 15, 20, 30, 40, 50, 60, 75, 100, 200, 300, 500, and 750 keV photons and plotted as a function of energy in 10° increments. The insert displays the low-energy behavior of the curves where F(0.5,θ) increases to a maximum of 2.08 at F(0.5,0°).

Table 2.1.3: 2D anisotropy function data for multiple active lengths at 10, 50, and 100 keV. L = 0.1, 0.3, and 0.5 cm were employed to show variations in F(r,θ) as a function of both active length and energy for an un-encapsulated line source.

	F(0.5,θ)								
	10 keV			50 keV			100 keV		
L (cm) =	0.1	0.3	0.5	0.1	0.3	0.5	0.1	0.3	0.5
0°	1.044	1.332	2.083	0.995	0.989	0.976	0.997	0.993	0.987
10°	1.033	1.314	2.035	0.998	0.993	0.977	0.998	0.996	0.988
20°	1.031	1.272	1.856	0.998	0.991	0.979	0.999	0.994	0.990
30°	1.032	1.226	1.654	1.000	0.993	0.983	0.999	0.995	0.991
40°	1.019	1.171	1.456	0.998	0.996	0.989	0.999	0.997	0.994
50°	1.018	1.111	1.289	1.000	0.997	0.992	1.000	0.998	0.995
60°	1.010	1.069	1.158	0.999	0.998	0.995	0.999	0.998	0.997
70°	1.010	1.027	1.066	1.000	0.998	0.999	0.999	0.998	0.999
80°	0.997	1.002	1.012	1.000	1.000	1.001	1.000	1.000	1.001

Table 2.1.3 shows F(0.5,θ) for L = 0.1, 0.3, and 0.5 cm at 10, 50, and 100 keV towards demonstrating trends in energy-related geometrical effects. For low energy sources, F(r,θ) can increase dramatically at short radial distances and low θ. In contrast, photon energies above 50 keV yield F(r,θ) values near unity near the transverse plane.

Volume averaging effects were not observed when comparing two different voxel thickness models. Comparable F(r,θ) data were obtained with a radial thickness of 0.02 cm and 10% of the radial distance at the point of calculation for all radionuclides. For each L, data were averaged at 11 radial distances and 9 angles between 0° and 80°. Average differences were less than 0.1% with a maximum standard deviation of 0.3% for ^{137}Cs, ^{192}Ir, and ^{169}Yb. ^{125}I and ^{103}Pd exhibited maximum average differences of 0.2% ± 0.7% and 0.2% ± 0.4%, respectively. However, the increased differences were due to increased statistical uncertainties at large r and small θ for the weakly penetrating, low energy radionuclides.

Unlike g(r) where MCNP tally choice significantly impacted the result, the *F4 tally and F6 tally provided comparable F(r,θ) values for each radionuclide. Performing the same comparison described above for all r and θ at each active length (99 data points for 6 L values), the standard deviation of the differences between F6 and *F4-derived F(r,θ) was 0.3% for all radionuclides, with decreasing differences for increasing photon

energy. Within the statistical uncertainties, $F(r,\theta)$ results obtained using either *F4 or F6 were identical. Though the *F4 tally does not use the energy-dependent $\mu_{en}\ \rho^{-1}$, it is dependent on spectral changes. Unlike g(r), however, $F(r,\theta)$ is determined at a fixed r and is not as subject to variations in photon spectra.

2.1.5 CONCLUSIONS

Radiation transport calculations are essential towards establishing brachytherapy dosimetry parameters via methods delineated in the AAPM TG-43U1 report. Numerous publications have presented various radiation transport codes and methodologies specific to a commercial seed, while few investigations have addressed generalizable issues pertinent to all sources. Simulations similar to those described here can be used to benchmark various radiation transport codes and assure a common standard for all investigators. Furthermore, tissue inhomogeneities and non-infinite media are inherent aspects of actual brachytherapy administration, and both were shown to cause significant variations in calculated brachytherapy dosimetry parameters. Thus, it is important for future investigators to model these effects, and/or work to advance the field of brachytherapy towards Monte Carlo-based treatment planning systems when appropriate to account for tissue heterogeneities and scatter conditions.

2.2 COMS eye plaque brachytherapy dosimetry for ^{103}Pd, ^{125}I, and ^{131}Cs[†]

2.2.1 ABSTRACT

MC simulations were performed to estimate brachytherapy dose distributions for Collaborative Ocular Melanoma Study (COMS) eye plaques. Brachytherapy seed models 200, 6711, and CS-1 Rev2 carrying ^{103}Pd, ^{125}I, and ^{131}Cs radionuclides, respectively, were modeled and benchmarked against previously published values. Calculated dose rate constants, $_{MC}\Lambda$, were 0.684, 0.924, and 1.052 cGy h^{-1} U^{-1} (±2.6%, k=1 uncertainty) for the models 200, 6711, and CS-1 Rev2, respectively. The seeds were

[†] Submitted to *Medical Physics* on 12/14/2007: C. S. Melhus and M. J. Rivard, "COMS eye plaque brachytherapy dosimetry for ^{103}Pd, ^{125}I, and ^{131}Cs," (07-853).

distributed into 12, 14, 16, 18, and 20 mm-diameter COMS eye plaques. Simulations were performed in both heterogeneous and homogeneous environments, where the latter were in-water and the former included the silastic seed carrier insert and gold-alloy plaque. MC-based homogenous central axis dose distributions agreed within 2% ± 1% (± 1 s.d.) to hand-calculated values. For heterogeneous simulations, notable photon attenuation was observed in the silastic insert, with dose reduction at 5 mm of 18%, 11%, and 10% for ^{103}Pd, ^{125}I, and ^{131}Cs, respectively. A depth-dependent correction factor was derived to correct homogenous central-axis dose distributions for plaque component heterogeneities, which were found to be significant at short radial distances.

2.2.2 INTRODUCTION

COMS was initiated during the 1980s to compare episcleral plaque brachytherapy using ^{125}I to enucleation, or removal of the involved eye.[2] Although many plaque designs have been utilized, the COMS protocol required use of a standardized plaque. Brachytherapy seeds were placed in channels within a polymer carrier that was adhered to a gold-alloy plaque. Brachytherapy dosimetry calculations for the protocol incorporated a number of assumptions that have been examined in the recent literature. These include: collimation by the plaque, photon absorption in the seed carrier, and characteristic gold x-rays from the plaque, among others.[51,81,82] While these studies have helped further understanding of eye plaque brachytherapy dosimetry, the AAPM recently created Radiation Therapy Committee Task Group 129 to formally review these studies and make recommendations to improve the standard of care. This work employs Monte Carlo techniques to simulate dose distributions from COMS eye plaques for commercially available brachytherapy seeds carrying either ^{103}Pd, ^{125}I, or ^{131}Cs. While other studies have employed Monte Carlo techniques to evaluate dose distributions from a single-seed in a plaque, this study is the first to our knowledge to fully model all of the brachytherapy seeds in COMS eye plaques.

2.2.3 MATERIALS AND METHODS

Brachytherapy dose distributions were simulated with the MCNP5 Monte Carlo radiation transport code published by Los Alamos National Laboratory.[67] The MCPLIB04 photon cross-section library was applied using data from ENDF/B-VI.[68]

Particle energy fluence and cell-heating tallies (*F4 and F6, respectively) were employed to calculate kerma per starting particle, which is equivalent to absorbed dose for the photon energies studied. Energy fluence tallies in MeV cm^{-2} were modified by Hubbell and Seltzer's[71] tabulated $\mu_{en}\ \rho^{-1}$ [$cm^2\ g^{-1}$] values to provide MC results in dose per starting particle. Photon emissions from ^{103}Pd, ^{125}I, and ^{131}Cs were simulated using emission frequencies from the National Nuclear Data Center (NNDC).[33] Photon energies below 10 keV that do not substantially penetrate Ti seed encapsulation were not included in these simulations.

2.2.3.1 Seed dosimetry benchmarking

Three brachytherapy seed models were studied: model 200, model 6711, and model CS-1 Rev2 containing ^{103}Pd, ^{125}I, and ^{131}Cs, respectively. The model 200 (Theragenics Corp.; Buford, GA) has an effective active length of 4.23 mm with source photons emitting from a thin Pd-metal coating on two right-cylindrical graphite markers separated by a lead marker.[20] Although variation in Pd thickness is possible, a nominal thickness of 2 μm was chosen for comparison to Williamson[14] and to the AAPM TG-43U1 report.[20] Source component dimensions and composition were replicated from Williamson.[14] The model 6711 brachytherapy seed, known as the OncoSeed™ (Oncura; Arlington Heights, IL) has consensus brachytherapy dosimetry data available for an active length, L, of 3.0 mm.[20] However, a more recent publication by Dolan *et al.* notes that current manufacturing practices produce L = 2.8 mm with beveled edges on a right-cylindrical silver marker.[15] The ^{125}I radionuclide is adsorbed onto the surface of the Ag marker in a 2 μm-thick halide coating. Other aspects of the model 6711 seed followed those presented by Dolan *et al.*[15] The model CS-1 Rev2 (IsoRay Inc.; Richland, WA) has a 4.0 mm long gold marker with a Pyrex/ceramic coating, which carries the ^{131}Cs radionuclide.[26] Source dimensions and composition were modeled per Rivard (L = 4.0 mm).[26]

To determine brachytherapy dosimetry parameters each seed was simulated in a 15 cm radius sphere of liquid water (ρ = 0.998 g cm^{-3}), with a hydrogen-to-oxygen atomic ratio of 2:1. 2D dose distributions were evaluated using a series of concentric spheres and cones as described by Rivard.[83] Results of these calculations were compared

to AAPM consensus data and/or to specific publications if AAPM consensus values were not available, *e.g.*, for the CS-1 Rev2. Specifically, $g_L(r)$ was determined for $1 \leq r \leq 70$ mm, and $F(r,\theta)$ was evaluated in 10° angular increments for $5 \leq r \leq 75$ mm.

In addition to the relative brachytherapy dosimetry parameters, calculations of the air kerma strength, s_K, and dose rate constant, ${}_{MC}\Lambda$, were performed. Due to different techniques used by individual investigators, several parameters were examined in the determination of s_K. The primary difference was the technique employed to enforce the δ=5 keV photon cutoff. Dosimetry investigators either eliminated tally contributions from photons with $E_\gamma < 5$ keV or incorporated a thin Al filter between the source and the MC tally volumes. The latter approach mimics measurement of S_K with the National Institute of Standards and Technology Wide Angle Free-Air Chamber (NIST WAFAC) as described in Appendix B of the AAPM TG-43U1 report.[20] A correction for photon attenuation in the Al filter (k_{foil}) was made by comparing calculations *in vacuo* with and without the filter present. In addition, correction for air attenuation was evaluated using two methods: (a) performing simulations in vacuum with modified *F4 tallies; and (b) calculating F6 tally results directly in air and correcting them with air attenuation coefficients determined from *F4 results in vacuum and in air. Finally, the internal seed structure was removed by replacing all components with a vacuum and also by replacing the seed with a point source for determination of apparent activity (A_{app}), where A_{app} is the activity of an unfiltered source providing the same air kerma strength as the filtered source.[84] As discussed below, A_{app} is required to calculate dose from a brachytherapy seed with a given contained activity.

MC geometry for air kerma calculations utilized a 200 cm-radius phantom with 1 mm-thick spherical shells spaced every 5 cm between 5 and 150 cm. The sampling volume within the spherical shells was delineated by the intersection of the spherical shells with a ±8° cone in the transverse plane of the seed. For simulations with the Al filter to block Ti K-edge x-rays, a 0.08 mm-thick spherical Al shell (ρ= 2.7 g cm^{-3}) was placed at r = 2 cm. This thickness of Al was similarly applied by Williamson;[14] although, other investigations have used different thickness, *e.g.*, 0.08636 mm for comparison to the NIST WAFAC.[85] When air was included in the model, the 40% relative humidity air recommended by TG-43U1 was incorporated.[20]

Calculations used 2 x 10^8 starting particles. This limited statistical uncertainties below 0.1% for air kerma calculations. For *in-water* calculations with ^{125}I and ^{131}Cs, statistical uncertainties were < 0.4% upto a distance of 7 cm along the transverse plane, and at an angle of 5° from the long axis were 0.8% and 2% at 2 and 7 cm, respectively. For comparison, ^{103}Pd photon statistical uncertainties on the transverse plane were 1% at 7 cm. At 5° from the long axis, statistical uncertainties were 1% and 5% at 2 and 7 cm, respectively, for the model 200 seed.

2.2.3.2 COMS plaque simulations

Standard COMS eye plaques with diameters of 12, 14, 16, 18, and 20 mm were simulated. These plaques assume a standard eye diameter of 24.6 mm and place the seed centers a distance of 1.4 mm from the outer sclera on the surface of a sphere of radius 13.7 mm.[86] For reproducible seed placement, troughs are molded into a medical grade silastic insert. The troughs are arranged in regular geometric shapes that provide cylindrical symmetry about the plaque central axis. The silastic insert is bonded to a 0.5 mm-thick plaque cast from Modulay, a gold alloy material used in dental medicine. Six eyelets spaced 30° apart are welded to the outer edge of the plaque for suturing the assembly to the eye during treatment. Descriptions of COMS plaques and related dosimetry are available in the literature and their references.[2,51,82,87,88]

Models 200, 6711, and CS-1 Rev2 seeds modeled as described above were inserted in silastic medium using the MCNP universe card [U] and copied and translated into the various plaque geometries with the cell translation card [TRCL]. Seed center coordinates followed the schema determined by R.W. Kline and reproduced in Rivard *et al.*[89] Silastic composition followed Chiu-Tsao *et al.*[51] Elemental composition of Modulay was gold, silver, copper, and palladium with mass percents of 77%, 14%, 8%, and 1% respectively.[82] Plaques were centered in a 15-cm radius sphere of liquid water to provide adequate photon backscatter, although, full-scatter geometry does not simulate patient treatment when the plaque is implanted near the patient surface. Comparison to homogenous brachytherapy dose distributions using the TG-43U1 formalism were made by replacing silastic and Modulay with liquid water. Inclusion of the silastic and Modulay elements is described as 'HETERO' for heterogeneous media, while homogenous

liquid water simulations is called 'HOMO.' For comparison to the single seed MC calculations of Chiu-Tsao *et al.* in a 20 mm diameter plaque, additional simulations were performed with a single seed in the silastic carrier.

Central axis depth doses to water were calculated in a 0.05 mm-radius cylinder, divided into 0.01 mm-thick sampling regions from the outer sclera to a depth of 13.4 mm in 0.5 mm steps. Additionally, the MCNP FMESH tally was employed to obtain a rectilinear volume of modified *F4 tally results encompassing the entire plaque. The rectilinear mesh had a grid spacing of 0.5 mm with the following dimensions: 25 mm x 25 mm parallel to the plaque face and 24 mm to -7.5 mm along the central axis where the origin is at the outer sclera on the plaque central axis.

MC-calculated dose per starting particle was converted to absorbed dose using **Eq. 2.2.1**.

$$\dot{d}(x,y,z) = {}_{SP}\dot{d}(x,y,z)\left[{}_{seed}S_K \cdot \left(\frac{A_{app}}{s_K}\right)\left(\frac{{}_{SP}s_K^{cont}}{{}_{SP}s_K^{app}}\right)\cdot I \cdot \mathrm{K}\right]\cdot n \qquad \textbf{(2.2.1)}$$

Where:

$\dot{d}(x,y,z)$	dose rate at position x,y,z
${}_{SP}\dot{d}(x,y,z)$	dose rate per starting particle at position x,y,z
${}_{seed}S_K$	S_K per seed needed to deliver $\dot{d}(x,y,z)$
${}_{SP}s_K^{cont}$	s_K per starting particle for the encapsulated source
${}_{SP}s_K^{app}$	s_K per starting particle for the apparent, un-encapsulated point source
I	number of photons per decay
K	constant representing starting particles per mCi-h
n	number of seeds

Generally, terms in **Eq. 2.2.1** convert the contained activity per seed in mCi to apparent air kerma strength of the encapsulated source. The total dose delivered was calculated by integrating $\dot{d}(x,y,z)$ over the prescribed treatment time. Following the American Brachytherapy Society (ABS) recommendations for uveal melanoma brachytherapy,[2] a treatment time of 168 h was utilized and source strength per seed (${}_{seed}S_K$) was chosen to deliver a total dose of 85 Gy at 5 mm on the central axis. While a 168 h treatment time may not deliver the recommended dose rate during treatment, the results are directly comparable to the conventional brachytherapy dose calculations of Rivard *et al.*[89]

For mesh tallies, statistical uncertainties of 4%, 3%, and 2% were obtained at 25 mm on the plaque central axis for ^{103}Pd, ^{125}I, and ^{131}Cs, respectively, for 2 x 10^8 starting particles. At the prescription depth (r = 5 mm), central axis statistical uncertainties were < 1% for all radionuclides and increased to 3%, 2%, and 1% at 12.5 mm off-axis for ^{103}Pd, ^{125}I, and ^{131}Cs, respectively. For tally regions shielded by the plaque in HETERO calculations, statistical uncertainties increased notably due to significant photon attenuation. Statistical uncertainties exceeding 40% were prevalent in this region. Plaque simulations generally required between 8 and 24 h of computing time on a 2.4 GHz Pentium D computer, though no variance reduction techniques were utilized.

2.2.4 RESULTS AND DISCUSSION

2.2.4.1 Seed dosimetry benchmarking

Radial dose function results for the models 200, 6711, and CS-1 Rev2 brachytherapy seeds are presented in **Table 2.2.1**. **Table 2.2.1** also includes the percent difference between the results of this study and consensus or reference $g_L(r)$ data. AAPM TG-43U1,[20] Dolan *et al.*,[15] and Rivard[26] were used for reference $g_L(r)$ values. $g_L(r)$ comparison for the CS-1 Rev2 were excellent (< 0.5%) because the seed model utilized in each study was identical. For the models 200 and 6711, $g_L(r)$ results were generally < 2%, although, larger variation occurred due to the difference in MC code, tally type, and volume-averaging. Similar $g_L(r)$ agreement was observed for comparison of the model 200 to Williamson[14] and for the model 6711 to TG-43U1.[20] Given the compound uncertainties, agreement between these datasets was acceptable.

Table 2.2.1: Radial dose function using the line source approximation for the three seed models and comparison to reference data.

	$g_L(r)$			Percent-difference from reference (%)		
r [mm]	200	6711	CS-1 Rev2	200[A]	6711[B]	CS-1 Rev2[C]
1	0.925	1.072	0.959	2	-3	< 0.5
3	1.324	1.086	0.993	-4	-2	-
4	1.297	1.081	1.001	-5	-1	-
5	1.258	1.070	1.008	-3	-1	< 0.5
10	1.000	1.000	1.000	-	-	-
15	0.753	0.908	0.963	1	1	< 0.5
20	0.556	0.814	0.908	1	1	< 0.5
30	0.299	0.633	0.777	-1	1	< 0.5
40	0.162	0.482	0.641	-1	1	< 0.5
50	0.086	0.361	0.520	-3	2	< 0.5
70	0.026	0.199	0.323	-2	3	< 0.5

[A] Ref. **14**
[B] Ref. **15**
[C] Ref. **26**

2D anisotropy results were compared to TG-43U1 for ^{103}Pd and ^{125}I and to Rivard for ^{131}Cs.[20,26] Model 200 ^{103}Pd results were compared from r=2.5 to 75 mm at nine radial distances with an average agreement of 2.5 ± 5.7% (± 1 s.d.). TG-43U1 offers ^{125}I $F(r,\theta)$ data between r=5 and 50 mm at six distances[20] and results agreed within an average of 3.3 ± 5.5% (± 1 s.d.). For the model CS-1 Rev2 ^{131}Cs seed, $F(r,\theta)$ agreed within 0.4 ± 1.2% (± 1 s.d.) to Rivard over thirteen radial distances between 0.5 and 70 mm.[26] As observed for $g_L(r)$, very good agreement was observed for the ^{131}Cs seed due to a shared seed model. For the ^{103}Pd and ^{125}I seeds, differences between our MC result and reference data were as high as ±20% directly on the source long axis for r < 2 cm. These variations were expected due to geometrical differences in tally sampling volumes given the short radial distance and high dose gradient. However, design of the COMS eye plaque mitigates concerns for source-end anisotropy because seeds are oriented parallel to the eye scleral surface where photons emitted along the source long axes are unlikely to escape the eye plaque Modulay walls.

For the models 200, 6711, and CS-1 Rev2, $_{MC}\Lambda$ values of 0.684, 0.924, and 1.052 cGy h^{-1} U^{-1}, respectively, exhibited good agreement to published values. AAPM consensus $_{MC}\Lambda$ from TG-43U1 for the models 200 and 6711 are 0.686 (-0.3%) and 0.950

(-0.5%) cGy h^{-1} U^{-1}, respectively.[20] For additional comparison, Dolan *et al.* obtained $_{MC}\Lambda$ = 0.942 cGy h^{-1} U-1 (-1.9%) for the model 6711.[15] For the model CS-1 Rev2, Rivard calculated 1.046 cGy h^{-1} U^{-1} (+0.6%),[26] and Wittman and Fisher simulated 1.040 cGy h^{-1} U^{-1} (+1.2%).[85] Calculation of $_{MC}\Lambda$ differed by less than 0.2% when cell-heating [F6] tallies were used in place of track-length estimators [modified *F4].

Determination of s_K using a thin-Al filter did not impact $_{MC}\Lambda$ in comparison to employing the DE/DF card to enforce the $\delta > 5$ keV photon energy cutoff. Aluminum filter correction factors (k_{foil}) of 1.066, 1.033, and 1.021 were determined for ^{103}Pd, ^{125}I, and ^{131}Cs, respectively, for 0.08 mm thickness. For comparison, k_{foil} factors measured for the NIST WAFAC with a 0.08636 mm-thick Al filter were 1.078 and 1.039 for the models 200 and 6711, respectively.[18] Wittman and Fisher calculated the NIST WAFAC correction factor for ^{131}Cs using an average photon energy and $\mu\ \rho^{-1}$ values to obtain k_{foil} =1.026.[85] Our MC-derived k_{foil} values for a 0.08 mm Al filter are in good agreement with the slightly larger factors required for a thicker filter. Calculated s_K per mCi values were: 0.721, 0.717, and 0.404 U mCi^{-1} for the models 200, 6711, and CS-1 Rev2, respectively. These s_K results are compared to 0.700 U mCi^{-1} (-2.9%) for Williamson's WAFAC simulation of the model 200,[14] 0.763 U mCi^{-1} (+6.4%) for the Dolan *et al.* WAFAC simulation of the model 6711,[15] and 0.410 U mCi^{-1} (+1.6%) for Wittman and Fisher's model CS-1 Rev2 calculation.[85]

Although no longer recommended by the AAPM TG-43U1 report,[20] A_{app} was determined to be 0.539 mCi for the model 200, 0.549 mCi for the model 6711, and 0.719 mCi for the model CS-1 Rev2. Calculations of A_{app} using the source distribution in vacuum without the seed components were statistically equivalent to the un-encapsulated point-source result. Incorporating the corresponding s_K, s_K / A_{app} for each seed was determined to be 1.336, 1.296, and 0.562 cm^2 cGy h^{-1} mCi^{-1} for the models 200, 6711, and CS-1 Rev2, respectively. Previous calculations of A_{app} divided the measured S_K by an assumed exposure factor $(\Gamma_\delta)_x$, and resulted in values of 1.293 (-3%) and 1.270 (-2%) for the models 200 and 6711, respectively.[84] Our MC-derived s_K / A_{app} for the models

200 and 6711 are in good agreement with accepted values; however, a confirming measurement of s_K / A_{app} is needed for the model CS-1 Rev2.

2.2.4.2 COMS plaque simulations

Table 2.2.2 tabulates central axis depth dose distributions for HETERO calculations that deliver a prescription dose (D_{Rx}) of 85 Gy at 5 mm depth for a 168 h implant. The s_K per seed required to administer the stated dose is also listed. In addition, the HETERO/HOMO ratio per starting particle is shown to demonstrate the impact of silastic attenuation as a function of depth. These ratios demonstrate that HETERO calculations require approximately +22.6 ± 0.3% (± 1 s.d.), +12.8 ± 0.2% (± 1 s.d.), and +10.6 ± 0.2% (± 1 s.d.) more s_K in each ^{103}Pd, ^{125}I, and ^{131}Cs seed, respectively, to deliver the same D_{Rx} to 5 mm depth.

Table 2.2.2: Central axis dose distributions for 12-20 mm diameter COMS eye plaques loaded with ^{103}Pd, ^{125}I, or ^{131}Cs brachytherapy seeds. The listed s_K was chosen to deliver 85 Gy to 5 mm depth for each plaque size. In addition, the ratio of HETERO/HOMO per starting particle is included, indicating the impact of attenuation in the silastic seed carrier as a function of treatment depth. Finally, s_K to deliver 85 Gy in HOMO media is presented.

	COMS eye plaque diameter [mm]					COMS eye plaque diameter [mm]				
Central axis [mm]	12	14	16	18	20	12	14	16	18	20
	^{103}Pd model 200 in HETERO medium [Gy]					^{103}Pd model 200 HETERO/HOMO Ratio				
0.0	365.7	322.6	258.5	249.8	226.2	0.77	0.76	0.74	0.75	0.74
0.5	312.7	279.2	233.0	220.5	203.5	0.78	0.78	0.76	0.76	0.76
1.0	268.2	241.8	210.9	197.2	182.6	0.80	0.79	0.78	0.77	0.77
1.5	229.6	212.4	189.0	177.2	163.6	0.81	0.80	0.79	0.79	0.78
2.0	199.4	185.5	168.9	160.6	150.7	0.81	0.81	0.80	0.80	0.79
2.5	170.9	162.5	151.2	143.2	136.4	0.82	0.81	0.80	0.80	0.80
3.0	146.9	142.7	134.2	129.4	124.6	0.82	0.81	0.81	0.80	0.80
3.5	127.9	124.3	120.6	116.9	112.6	0.82	0.82	0.81	0.81	0.80
4.0	110.9	109.5	107.3	105.3	102.6	0.82	0.82	0.81	0.81	0.81
4.5	96.8	96.7	95.1	94.6	92.1	0.82	0.82	0.82	0.81	0.81
5.0	85.0	85.0	85.0	85.0	85.0	0.82	0.82	0.81	0.82	0.81
6.0	65.8	67.4	68.4	69.9	69.7	0.82	0.82	0.82	0.82	0.82
7.0	51.9	53.2	54.6	56.2	57.4	0.82	0.82	0.82	0.81	0.82
8.0	41.1	42.6	44.2	46.6	47.7	0.82	0.82	0.82	0.82	0.82
9.0	32.7	34.6	36.3	38.3	39.5	0.81	0.82	0.81	0.82	0.82
10.0	26.1	28.3	29.7	31.9	33.1	0.81	0.82	0.82	0.83	0.82
s_K[U]	7.290	4.811	5.060	3.393	3.120	5.966	3.932	4.113	2.770	2.542
	^{125}I model 6711 in HETERO medium [Gy]					^{125}I model 6711 HETERO/HOMO Ratio				
0.0	357.3	313.8	252.4	246.1	221.6	0.88	0.87	0.86	0.86	0.86
0.5	301.4	267.1	224.7	217.0	197.3	0.89	0.88	0.87	0.87	0.87
1.0	256.7	230.5	202.1	190.7	176.9	0.89	0.88	0.88	0.87	0.87
1.5	218.7	200.6	179.0	170.2	158.4	0.89	0.89	0.88	0.87	0.87
2.0	188.2	175.2	160.8	153.4	144.2	0.89	0.89	0.88	0.88	0.88
2.5	162.9	153.5	143.9	140.1	130.6	0.90	0.89	0.88	0.88	0.88
3.0	141.2	135.4	128.8	125.7	119.4	0.90	0.89	0.89	0.89	0.88
3.5	123.8	120.2	115.9	113.7	110.6	0.89	0.89	0.89	0.88	0.88
4.0	108.3	106.6	104.3	103.8	99.7	0.89	0.89	0.89	0.89	0.88
4.5	95.6	95.0	93.9	94.1	91.8	0.89	0.89	0.89	0.89	0.89
5.0	85.0	85.0	85.0	85.0	85.0	0.89	0.89	0.89	0.88	0.89
6.0	67.2	68.3	69.1	71.2	70.3	0.88	0.88	0.88	0.88	0.88
7.0	53.7	55.4	56.6	60.0	59.8	0.88	0.87	0.87	0.88	0.88
8.0	44.0	45.8	47.2	50.9	50.9	0.87	0.87	0.88	0.88	0.88
9.0	36.4	37.8	39.3	42.3	43.9	0.86	0.87	0.87	0.88	0.88
10.0	30.3	31.7	33.3	35.9	36.8	0.86	0.87	0.87	0.87	0.87
s_K[U]	4.738	3.088	3.225	2.174	1.969	4.204	2.742	2.856	1.922	1.749
	^{131}Cs model Rev2 in HETERO medium [Gy]					^{131}Cs model Rev2 HETERO/HOMO Ratio				
0.0	335.3	292.8	242.3	228.8	212.0	0.91	0.91	0.90	0.90	0.89
0.5	284.7	253.4	217.8	202.5	188.5	0.92	0.91	0.90	0.90	0.90
1.0	243.8	220.6	195.0	181.3	172.0	0.92	0.92	0.91	0.90	0.90
1.5	211.2	193.4	175.2	163.8	156.1	0.92	0.92	0.91	0.91	0.91
2.0	183.1	170.0	158.1	147.7	141.0	0.92	0.92	0.91	0.90	0.90
2.5	159.3	151.0	141.3	135.3	129.6	0.92	0.92	0.91	0.91	0.91
3.0	139.2	133.7	128.2	122.7	119.1	0.92	0.91	0.91	0.91	0.91
3.5	122.8	119.5	115.6	112.2	110.2	0.91	0.91	0.91	0.91	0.91
4.0	107.9	106.5	104.4	101.5	100.4	0.91	0.91	0.90	0.91	0.91
4.5	95.6	94.4	94.4	92.9	93.0	0.91	0.91	0.91	0.91	0.91
5.0	85.0	85.0	85.0	85.0	85.0	0.90	0.91	0.90	0.91	0.90
6.0	68.0	69.2	70.2	71.1	72.2	0.90	0.90	0.90	0.90	0.90
7.0	55.3	56.8	58.7	59.5	61.4	0.89	0.89	0.89	0.89	0.90
8.0	45.4	47.6	48.9	50.8	52.8	0.88	0.89	0.89	0.89	0.89
9.0	38.0	39.7	41.1	43.3	45.2	0.87	0.89	0.88	0.89	0.89
10.0	32.0	33.5	35.1	37.0	39.1	0.87	0.87	0.88	0.88	0.88
s_K[U]	5.257	3.403	3.568	2.348	2.166	4.749	3.081	3.218	2.128	1.956

Comparison of our HOMO plaque simulations were made to hand calculations[89] following the eye plaque dosimetry recommendations of the AAPM TG-43U1 report in Appendix C.[20] As for this study, hand calculations determined s_K per seed necessary to deliver 85 Gy to 5 mm. The ratio of MC-calculated to hand-calculated s_K per seed to deliver D_{Rx} was 1.02 ± 0.01 (± 1 s.d.), 1.03 ± 0.01 (± 1 s.d.), and 1.00 ± < 0.005 (± 1 s.d.) for the models 200, 6711, and CS-1 Rev2, respectively. In addition to s_K per seed comparison, the central axis dose HOMO/hand-calculation ratio was evaluated in 1 mm steps between the inner sclera (0 mm) and 10 mm. For the model 200, the ratio was 0.98 ± 0.01 (± 1 s.d.) for $0 \leq r \leq 3$ mm and 1.00 ± 0.01 (± 1 s.d.) for $3 \leq r \leq 10$ mm. For the model 6711, the HOMO/hand-calculation ratio was 1.00 ± 0.01 (± 1 s.d.) for $r \leq 9$ mm and 0.98 ± 0.01 (± 1 s.d.) for r = 10 mm. The ratio was 1.00 ± 0.01 (± 1 s.d.) for all r for the model CS-1 Rev2. The agreement between MC and hand calculations not only validates our dose calculation methodology (**Eq. 2.2.1**), but also supports recommendations in Appendix C of the AAPM TG-43U1 for determining COMS doses at short radial distances in homogenous liquid water media.[20]

While the original COMS protocol assumed negligible impact on implant dosimetry due to the silastic insert and Modulay plaque, it is now well recognized that these materials perturb dose distributions.[81-82,88] Chiu-Tsao *et al.* evaluated the impact of heterogeneities using MC methods for a single model 6711 seed at the center of a 20 mm diameter COMS plaque.[51] They observed an approximate reduction of 10% at a depth of 10 mm on the central axis due to photon attenuation in silastic, a factor that has subsequently been employed to reanalyze results of the COMS study.[90] The Plaque Simulator software [version 4; BEBIG GmbH, Berlin Germany] - which uses the AAPM TG-43U1 brachytherapy dosimetry formalism, patient-specific imaging, and factors to account for plaque collimation, among other features – similarly applies the 10% correction of Chiu-Tsao *et al.* for silastic attenuation.[82] Our single seed simulations for the model 6711 in a 20 mm plaque obtained a difference of -11% for HETERO/HOMO, which is in good agreement with Chiu-Tsao *et al.* For the models 200 and CS-1 Rev2 HETERO/HOMO differences of -18% and -12%, respectively, were observed at 10 mm depth. **Figure 2.2.1** presents the ratio of HETERO/HOMO ratios for the single seed to the fully-loaded plaque using a 20 mm diameter plaque. **Figure 2.2.1** demonstrates that a

10% correction factor for the model 6711 is adequate for $r \geq 5$ mm central axis dose calculations; however, the scleral dose is over-estimated when using a single-seed correction factor. For COMS implants using ^{103}Pd, some investigators have introduced applicators that employ a thin gold insert to guide seed placement to obviate the need for silastic.[87] The insert was designed to alleviate the expected large attenuation of ^{103}Pd in silastic,[82,87] which we determined to be in excess of 18% at 5 mm depth in this study.

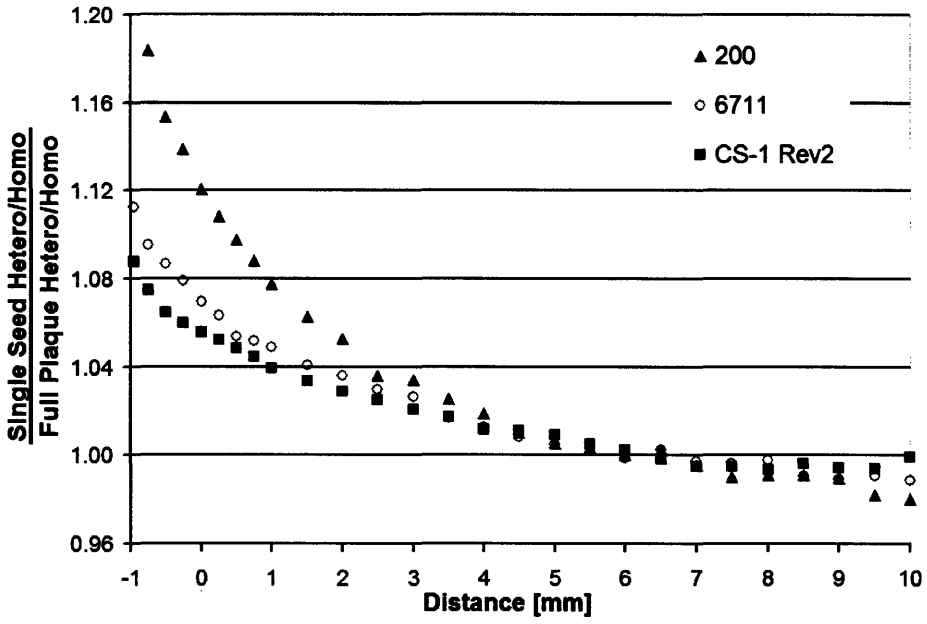

Figure 2.2.1: Ratio of HETERO/HOMO for a single seed and fully-loaded (n=24) 20 mm eye plaque. Note differences below 5 mm where the single seed model over-estimates the heterogeneity correction factor; however, the ratio for $r \geq 5$ mm, which is the ABS-recommended depth for lesion height below 5 mm, is within ±2%.

Figure 2.2.2 presents the average ratio of HETERO/HOMO central axis dose when s_K is chosen to deliver D_{Rx} = 85 Gy at 5 mm depth for five plaque diameters. The ABS recommendations and COMS protocol dictates a minimum prescription depth of 5 mm. Our study shows that the impact of silastic attenuation on dose distributions can vary significantly for $r \leq 5$ mm. Furthermore, dose to organs at risk, namely inner and outer sclera, could be over-estimated.

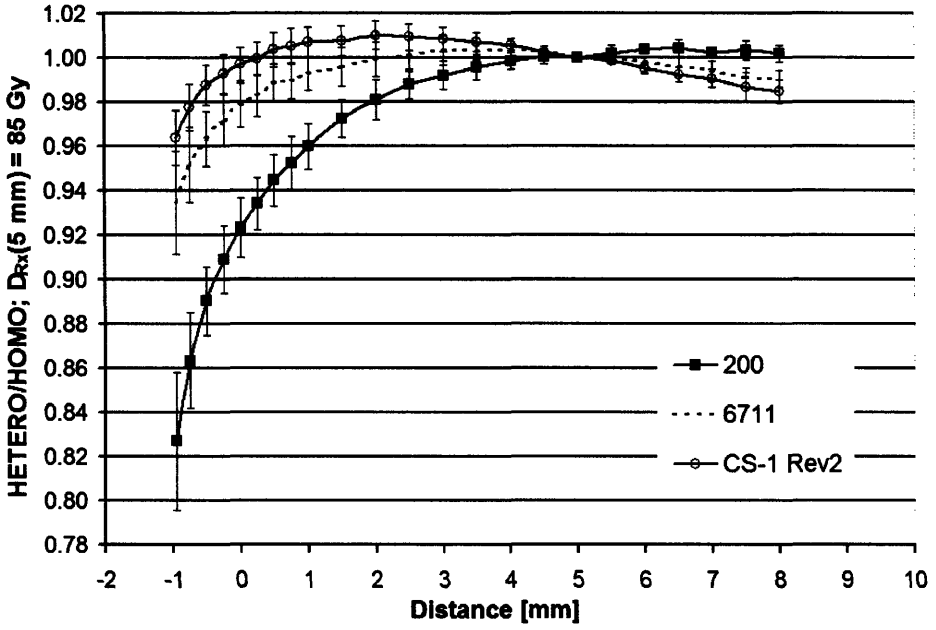

Figure 2.2.2: HETERO/HOMO ratio for D_{Rx} = 85 Gy at 5 mm depth and averaged over five plaque sizes. For all three radionuclides, dose to inner and outer sclera is reduced in comparison to dose calculated in HOMO water medium. Error bars represent ± 1 s.d.

Figure 2.2.2 demonstrates that a constant factor may not be adequate to account for silastic attenuation when $r \leq 5$ mm; however, a 1D function can modify central axis dose to account for silastic attenuation. Coefficients of a fourth order polynomial equation (**Eq. 2.2.2**) that calculates the HETERO/HOMO ratio per starting particle as a function of central axis distance, r, in mm are given in **Table 2.2.3**.

$$C_{silastic}(r) = \frac{D_{Hetero}(r)}{D_{Homo}(r)} = a_0 r^4 + a_1 r^3 + a_2 r^2 + a_3 r + a_4 \qquad \textbf{(2.2.2)}$$

In **Table 2.2.3**, a_i coefficients were derived by fitting the average HETERO/HOMO ratio from five plaque sizes.

Table 2.2.3: Fourth-order polynomial coefficients to calculate the HETERO/HOMO ratio per starting particle as a function of distance along the central axis for $-1 \leq r \leq 10$ mm. Note that distance should be reported in mm.

Seed model	a_4	a_3	a_2	a_1	a_0	R^2
200 (^{103}Pd)	7.478E-1	4.375E-2	-1.029E-2	1.056E-3	-3.931E-5	0.99
6711 (^{125}I)	8.629E-1	2.062E-2	-5.433E-3	5.336E-4	-1.904E-5	0.98
CS-1 Rev2 (^{131}Cs)	8.993E-1	1.505E-2	-5.167E-3	5.872E-4	-2.434E-5	0.99

Absolute dose distributions for the 16 mm COMS plaques are presented in **Figure 2.2.3** for both HOMO and HETERO MC simulations after a 168 h treatment. Note the increase in penumbra and depth dose with increasing photon energy.

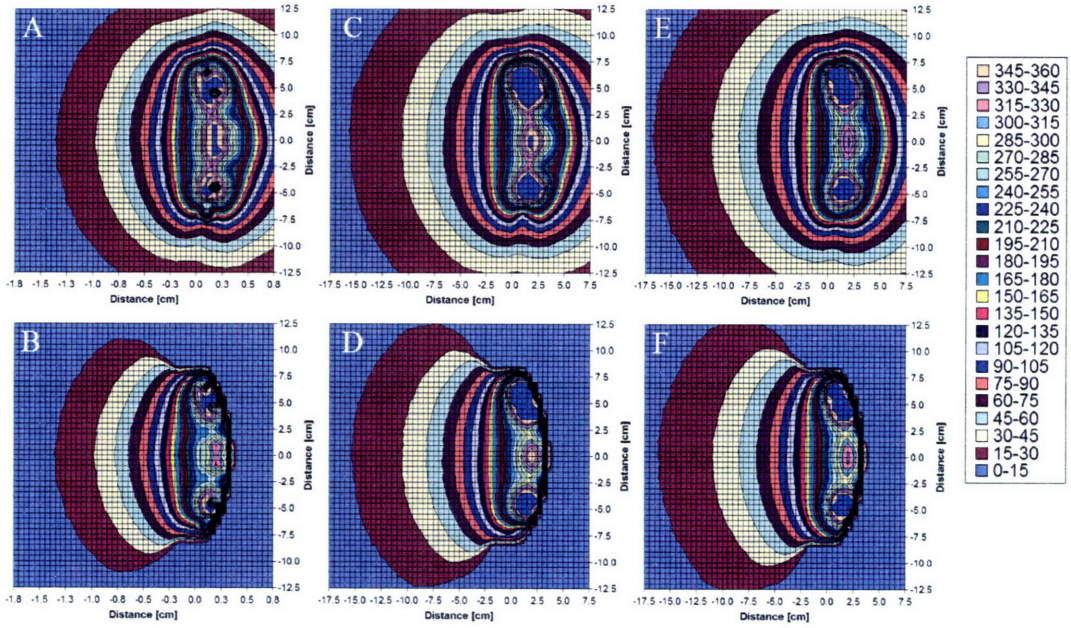

Figure 2.2.3: Dose [Gy] for a 16 mm COMS eye plaque with s_K per seed to deliver D_{Rx} (5 mm) = 85 Gy. Seed model and heterogeneity correction were as follows: A) HOMO model 200, B) HETERO model 200, C) HOMO model 6711, D) HETERO model 6711, E) HOMO model CS-1 Rev2, and F) HETERO model CS-1 Rev2. Note increased penetration due to increased average photon energy.

2.2.4.3 Uncertainty analysis

Uncertainty analyses followed recommendations introduced by the AAPM TG-43U1 Report[20] and expanded upon by Rivard.[26] In addition to the Type A stochastic uncertainties described above, Type B systematic uncertainties were calculated assuming r = 0.5 cm. Because seed component geometry and internal dynamic motion were not explicitly examined and because radial distances were small, the AAPM TG-43U1 recommended value of 2% was utilized for seed geometry-related uncertainty.[20] Uncertainty in source photon spectrum, phantom composition, MC physics modeling, and $\mu_{en}\ \rho^{-1}$ values were taken to be 0.1%, 0.01%, 0.3%, and 1.2%, respectively, per Rivard.[26] These uncertainties combine in quadrature to account for a total (k=1) uncertainty of 2.6% at r = 5 mm on the central axis for all three radionuclides.

Considering calculations at 12.5 mm off the plaque central axis at 5 mm, the k=1 uncertainty rises to 3.8%, 3.1%, and 2.6% for ^{103}Pd, ^{125}I, and ^{131}Cs, respectively.

2.2.5 CONCLUSIONS

Three brachytherapy seeds – the model 200 ^{103}Pd seed, the model CS-1 Rev2 ^{131}Cs seed, and the model 6711 ^{125}I seed – were simulated using MCNP5. Calculations of $g_L(r)$, $F(r,\theta)$, s_K, s_K / A_{app}, and $_{MC}\Lambda$ were in good agreement to previously published values. Seeds were subsequently modeled in standard COMS eye plaques, and dose calculations performed to evaluate the impact of absorption in plaque components. Previous observations of 10% dose reduction for a single ^{125}I seeds at 10 mm due to the silastic seed carrier were validated, and MC calculations performed to assess attenuation as a function of depth for fully-loaded plaques. These calculations confirmed that silastic attenuation must be taken into account in treatment planning and that a depth-dependent scaling factor could be used for central axis dose calculations, including organs at risk - inner and outer sclera. Most importantly, clinical practices not accounting for attenuation in plaque components may be delivering 10% - 20% below the desired therapeutic dose, depending on the combination of radionuclide and plaque composition. Towards improving the clinical utility of these simulations, the plaque model should be integrated with a human eye model, allowing determination of dose to other organs at risk, including the lens and optic nerve.

3 NEUTRON DOSIMETRY

3.1 Approaches to calculating AAPM TG-43 brachytherapy dosimetry parameters for neutron sources

3.1.1 ABSTRACT

Purpose: Generally, the 2004 AAPM TG-43U1 brachytherapy dosimetry formalism has been applied only to photon emitting radionuclides. Recent MC studies of un-encapsulated virtual photon sources yielded distinct energy and geometry-specific dose deposition characteristics not readily apparent with encapsulated sources. Towards improving understanding of neutron-based brachytherapy, MC techniques were similarly applied to virtual, un-encapsulated neutron sources.

Materials and methods: The MCNP5 code was utilized for all calculations. Dose to water was determined using the F6 (cell-heating) tally for monoenergetic neutron sources between 0.001 and 10 MeV. These energies bound those emitted by encapsulated neutron sources such as Am:Be or ^{252}Cf. The DLC-220 cross-section library was used, and the impact of thermal scattering factors, $S(\alpha,\beta)$, were evaluated. $g_L(r)$ and $F(r,\theta)$ were determined for $L \leq 0.5$ cm using varying tally-sampling geometries for neutron and secondary photon dose, which was generated using MODE NP transport in phanta between 5 and 50 cm radius. In addition, comparisons of F6 and modified-F4 tallies were made.

Results: Inclusion of $S(\alpha,\beta)$ provided notably higher F6 values at thermal energies due to the increased kerma contributions from thermalized neutrons. Considering radial dose

deposition, comparison of phantom size showed high energy neutrons were less sensitive to a decrease in phantom radius. At 3 cm from the surface of a 15 cm phantom, g(r) changed by 1%, 4%, and 8% for 2, 0.2, and 0.002 MeV neutrons, respectively, in comparison to a 30 cm phantom. Considering the same phantom ratio at 0.1 cm from the surface, 0.88 and 0.26 are obtained for 2 and 0.1 MeV neutrons. Radial dose values plotted as a function of energy showed a nadir at 0.1 MeV for distances > 10 cm, a maximum at 0.01 MeV for distances < 0.5 cm, and a trend towards unity for energies > 1 MeV. Volume averaging for neutron dose deposition was shown to be similar to that of photon deposition, with spherical shell widths below 1 mm providing statistically equivalent tally results.

Conclusions: Characteristics of neutron physical dose distributions in brachytherapy were evaluated for virtual sources using the TG-43U1 dosimetry formalism. These insights allow for improvement in the design of novel neutron brachytherapy sources.

3.1.2 INTRODUCTION

As discussed in **sections 1.1.1** and **2.1**, the 2004 AAPM TG-43U1 brachytherapy dosimetry formalism applied only to encapsulated ^{103}Pd and ^{125}I sources. However, brachytherapy dosimetry investigators have applied the formalism to various photon-emitting radionuclide sources. The formalism was applied to ^{252}Cf by Rivard in 2000[30] which was the first application of the TG-43 formalism to neutron-emitting sources. **Section 2.1** demonstrated energy and geometry-specific dose distribution characteristics for AAPM TG-43 brachytherapy dosimetry parameters of un-encapsulated virtual photon sources. Towards improving understanding of neutron-based brachytherapy, similar MC techniques were applied to virtual neutron sources.

3.1.3 MATERIALS AND METHODS

3.1.3.1 MC simulations

Dose distributions for monoenergetic neutrons were modeled and evaluated using the AAPM TG-43U1 brachytherapy dosimetry formalism. The formalism was also applied to secondary photons generated during neutron transport.

Simulations in liquid water were performed using the MCNP5 radiation transport code.[67] Cell heating tallies were obtained using the MCNP F6 tallies. MODE N P transport physics was utilized to calculate secondary photons generated through neutron transport. For comparison to F6-derived results, neutron particle fluence (F4) tallies were modified using International Commission on Radiation Units and Measurement (ICRU) neutron kerma coefficients published in Report 63 for comparison to unmodified cell heating tallies (F6).[91] ICRU-63 kerma coefficients include neutron energies between 2.53×10^{-8} and 150 MeV; however, MCNP5 tracks neutrons with energies as low as 10^{-11} MeV. Radiation dose deposited by secondary photons was calculated by multiplying energy fluence tallies (*F4) by the mass-energy absorption coefficients for water published by Hubbell and Seltzer.[71]

As for photon simulations in **section 2.1**, source encapsulation was not included. Water was modeled using a 2:1 atomic ratio for ^{1}H:^{16}O and a mass density of 0.998 g cm^{-3}. For neutron transport, the MCNP5 neutron cross-section library 66c from ENDF/B-VI was employed,[68] and the default MCNP5 photon cross-section library, p04, was applied. The thermal neutron scattering library LWTR.60t was selected to include $S(\alpha,\beta)$ factors, which incorporate additional molecular scattering considerations for neutrons below 4 eV.[67] Additional simulations were performed without $S(\alpha,\beta)$ factors to determine the impact on tally results.

3.1.3.2 Phantom size

The impact of limited phantom size was evaluated using $g_P(r)$ for monoenergetic neutrons (0.001, 0.01, 0.1, and 1 MeV) in a spherical water phantom. For comparison, the ^{252}Cf neutron energy spectrum published by Mannhart was similarly modeled.[92] Concentric spheres were simulated to define spherical shells allowing calculation of $g_P(r)$ at radial distances between 0.5 and 25 cm. For comparison to $g_P(r)_{50}$, $g_P(r)_R$ was calculated with R = 5, 10, 15, 20, 25, 30, 35, 40, and 45 cm. In addition to neutron $g_P(r)$, the secondary photon $g_P(r)$ was determined.

Volumetric averaging for ^{252}Cf neutrons was assed by varying the thickness of the tally volume (*i.e.*, spherical shell). Shells with thickness of 0.002, 0.005, 0.01, 0.02, 0.05, 0.1, 0.2, 0.5, and 1 cm were used in simulations and results normalized to the 0.01 cm-

thick voxel. The sampling volume was defined by equally displacing the inner and outer radii from the point of calculation. Volume averaging errors were evaluated at 23 distances between 0.5 and 20 cm for ± 0.5% variation in $g_P(r)$ in comparison to the 0.01 cm-thick voxel.

3.1.3.3 Radial dose function

Radial dose functions were calculated for monoenergetic neutron sources following the brachytherapy dosimetry formalism in AAPM TG-43U1.[20] Neutron energies of 0.001, 0.002, 0.005, 0.01, 0.02, 0.05, 0.1, 0.2, 0.5, 0.7, 1, 2, and 5 MeV were simulated. The $g_P(r)$ values were calculated between $0.1 \leq r \leq 14.9$ cm at 41 radial distances. Calculations were performed in liquid water spheres with R = 15 and 30 cm.

Statistical uncertainties for neutron tally results were below 0.5% for all neutron energies and distances using 10^7 starting particles. Secondary photons yielded statistical uncertainties between 2% and 5% at short radial distances (< 1 cm) where insufficient neutron interactions have occurred to engender secondary photons. For $1.5 \leq r \leq 15$ cm, the statistical uncertainties for secondary photons were below 0.5%.

3.1.3.4 $F(r,\theta)$

$F(r,\theta)$ for monoenergetic primary neutrons was calculated for $0.5 \leq r \leq 5.0$ cm using three active lengths (0.1, 0.3, and 0.5 cm) in a liquid water phantom of R = 10 cm. Neutron energies of 0.001, 0.002, 0.01, 0.02, 0.05, 0.1, 0.2, 0.5, 1, 2, and 5 MeV were included. The simulation geometry was similar to that used for photon analyses, described in **section 2.1.3.2**. The line source was a cylinder of radius 10^{-6} cm; 1° angular resolution was included; and, voxel thickness of 5% of the radial distance was employed. Radial distances were 0.5, 0.75, 0.9, 1, 1.5, 2, 2.5, 3, and 5 cm. ICRU 63-modified F4 tally results were used to determine $F(r,\theta)$ following the AAPM TG-43U1 brachytherapy dosimetry formalism (see **section 7.2**).[20]

MCNP5 simulations used MODE N P transport with at least 7×10^6 starting particles. As observed for photons, the minimum statistical uncertainty was along the transverse plane, while the maximum statistical uncertainty was along the long axis. At r = 1 cm for L = 0.1 cm, the statistical uncertainties at 5° and 85° were 1.4% and 0.4% for

0.001 MeV; 1.5% and 0.4% for 0.01 MeV; 1.4% and 0.4% for 0.1 MeV; and, 1.2% and 0.3% for 1 MeV, respectively. At r = 5 cm for L = 0.5 cm, the corresponding statistical uncertainties at 5° and 85° were 0.3% and 0.1% for 0.001 MeV ($n = 2 \times 10^7$); 2.3% and 0.7% for 0.01 MeV; 2.9% and 0.8% for 0.1 MeV; and, 1.4% and 0.4% for 1 MeV, respectively.

3.1.4 RESULTS AND DISCUSSION

3.1.4.1 Phantom size

The ratio of $g_P(r)_R$ to $g_P(r)_{50}$ is shown in **Figure 3.1.1** for 0.001, 0.01, 0.1, and 1 MeV neutrons. For a $R \geq 10$ cm, $g_P(r)_R$:$g_P(r)_{50}$ for 0.001, 0.01, and 0.1 MeV neutrons are equivalent. The $g_P(r)$ ratios for 1 MeV neutrons differ from the other three energies for all phantom radii. For comparison, **Figure 3.1.2** demonstrates $g_P(r)_R$:$g_P(r)_{50}$ for ^{252}Cf neutrons.

Unlike the case for photon radiation, the $g_P(r)$ ratios are nearly independent of phantom size. The magnitude of the neutron dose fall-off near the phantom surface is similar for all phantom sizes, with slight variations for R = 5 cm where the calculated dose at 1 cm may vary due to limited backscatter compared to larger phantom sizes.

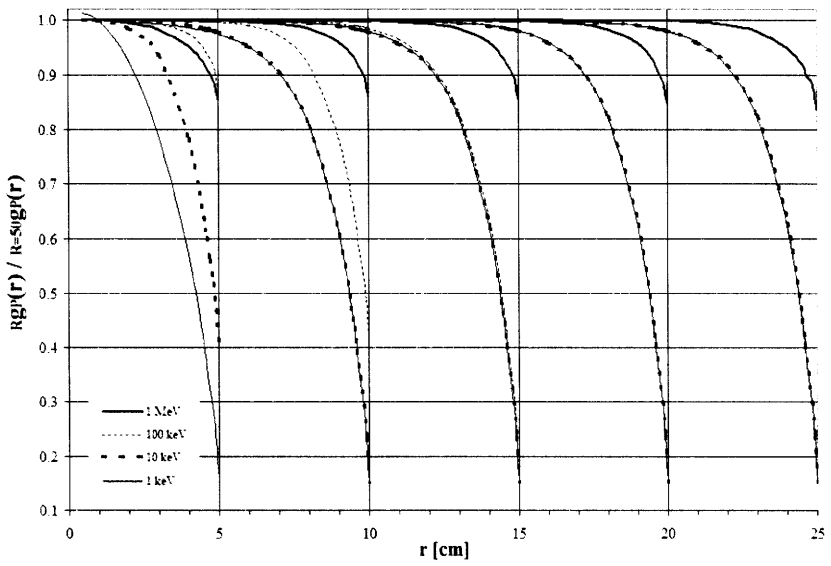

Figure 3.1.1: Ratio of neutron $g_P(r)$ to $g_P(r)_{50}$ for 0.001, 0.01, 0.1, and 1 MeV neutrons. Note that the 0.001, 0.01, and 0.1 MeV ratios are equivalent for $R \geq 15$ cm.

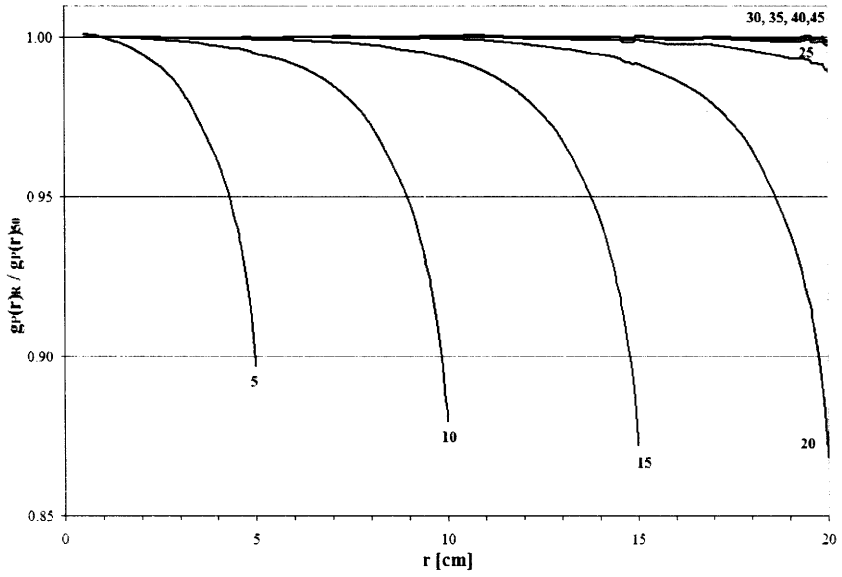

Figure 3.1.2: Ratio of neutron $g_P(r)$ to $g_P(r)_{50}$ for ^{252}Cf neutrons.

Table 3.1.1 shows the $g_P(r)_{50}$ for the four neutron energies and ^{252}Cf spectrum simulated. Note that a radial dose function value of 0.5 occurs at approximately 8, 2, 2, and 5 cm for 0.001, 0.01, 0.1, and 1 MeV and at 8 cm for ^{252}Cf neutrons. In contrast, a $g_P(r)_{50}$ value of 0.5 for ^{103}Pd and ^{125}I photon sources occurs at approximately r = 2.0 and 4.5 cm, respectively.

Table 3.1.1: $g_P(r)_{50}$ calculated for 0.001, 0.01, 0.1, and 1 MeV neutrons using the F6 tally modified by $S(\alpha,\beta)$ for water. In addition, $g_P(r)$ for ^{252}Cf neutrons is shown.

	$g_P(r)_{50}$				
R [cm]	0.001 MeV	0.01 MeV	0.1 MeV	1 MeV	^{252}Cf
0.5	1.28	1.36	1.20	1.02	1.01
1.0	1.00	1.00	1.00	1.00	1.00
2.0	0.75	0.52	0.64	0.88	0.96
3.0	0.73	0.28	0.38	0.73	0.90
4.0	0.76	0.17	0.21	0.59	0.82
5.0	0.76	0.12	0.12	0.46	0.75
6.0	0.70	0.09	0.06	0.36	0.67
7.0	0.61	0.08	0.04	0.28	0.60
8.0	0.51	0.06	0.02	0.21	0.53
9.0	0.41	0.05	0.01	0.16	0.47
10.0	0.32	0.04	0.01	0.12	0.42
11.0	0.25	0.03	0.01	0.09	0.37
12.0	0.19	0.02	0.00	0.06	0.33
13.0	0.14	0.02	0.00	0.05	0.29
14.0	0.10	0.01	0.00	0.03	0.26
15.0	0.08	0.01	0.00	0.02	0.23
16.0	0.06	0.01	0.00	0.02	0.20
17.0	0.04	0.01	0.00	0.01	0.18
18.0	0.03	0.00	0.00	0.01	0.15
19.0	0.02	0.00	0.00	0.01	0.14
20.0	0.02	0.00	0.00	0.00	0.12

The impact of phantom size on secondary photons is shown in **Figure 3.1.3** for monoenergetic neutrons and in **Figure 3.1.4** for ^{252}Cf neutrons. Unlike the neutrons $g_P(r)$ ratios in **Figure 3.1.1** and **3.1.2**, the ratio of $g_P(r)$ to $g_P(r)_{50}$ for secondary photons varies as a function of phantom radius. As the phantom radius increases, however, the ratio approaches unity.

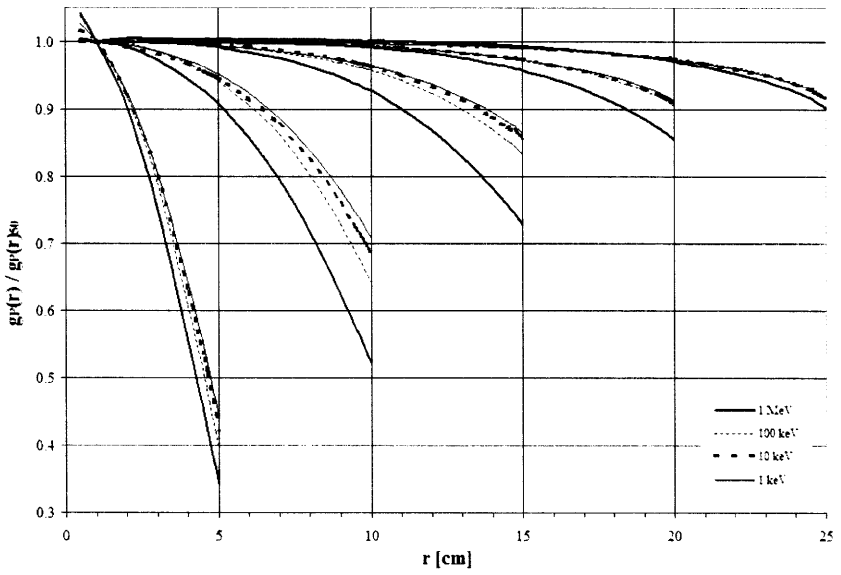

Figure 3.1.3: Ratio of secondary photon $g_P(r)$ to $g_P(r)_{50}$ generated for starting neutron energies of 0.001, 0.01, 0.1, and 1 MeV for $R \leq 25$ cm.

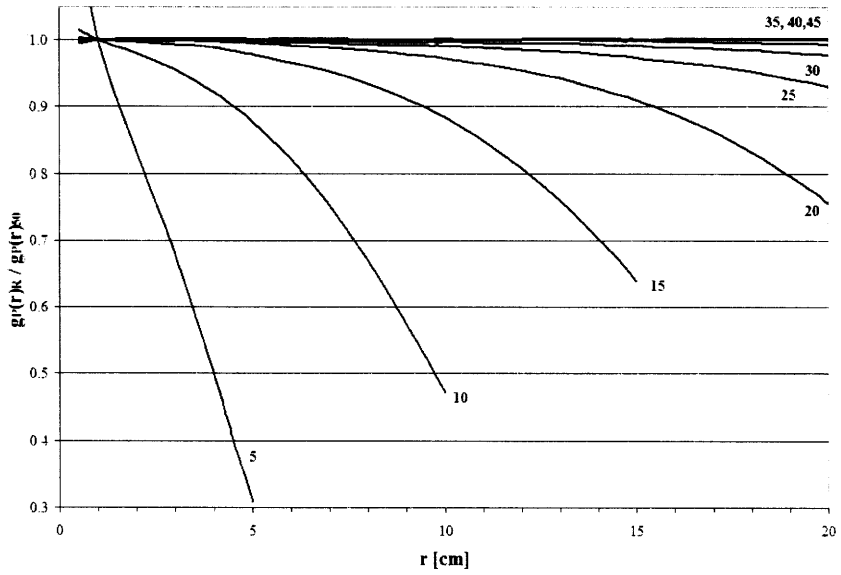

Figure 3.1.4: Ratio of secondary photon $g_P(r)_R$ to $g_P(r)_{50}$ for ^{252}Cf neutrons.

Variation of voxel width for ^{252}Cf neutrons showed no variation in $g(r) > \pm 0.5\%$ for voxel thickness of 0.1 cm and below. A voxel width of 0.2 cm differed from 0.01 cm at only 13% (3 of 23) radial distances. As shown for photon radiation, voxel widths > 0.5 cm resulted in notable volume-averaging effects.

3.1.4.2 Radial dose function

The $g_P(r)_{15}$ for monoenergetic neutrons is shown in **Figure 3.1.5** as a function of energy with each line indicating isodistances. A strong correlation between $g_P(r)$ and energy is observed. There is a nadir for neutrons with approximately 0.1 MeV in energy for distances $\geq$ 5 cm. For example, $g_P(12)$ is 50 times smaller for 0.1 MeV neutrons than for 0.001 MeV neutrons. Maximum $g_P(r)$ occurred at low energies (< 0.01 MeV) for short radial distances (< 0.5 cm). There is a trend towards unity for neutron energies > 1 MeV due to decreased probability of interaction for neutrons at higher energies.

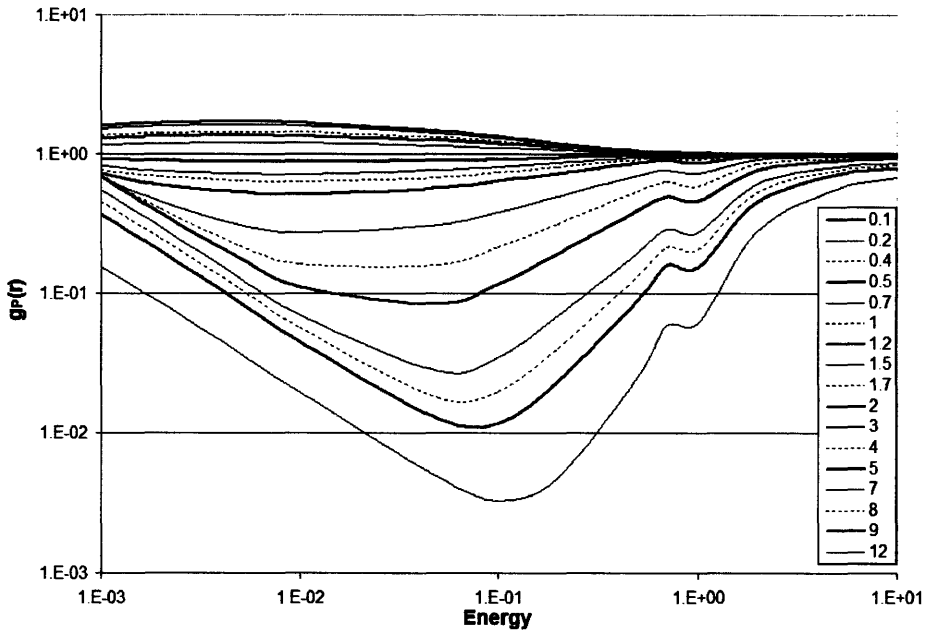

Figure 3.1.5: MC-calculated $g_P(r)_{15}$ plotted as a function of energy for $0.1 \leq r \leq 12$ cm. Note that the curves represent different radial distances. The most significant attenuation along the transverse plane occurs at 0.1 MeV.

Similarly, $g_P(r)_{15}$ for secondary photons is shown in **Figure 3.1.6** as a function of incident neutron energy. In contrast to neutrons and primary photon radiation (see **section 2.1**), $g_P(r)$ for secondary photons is lowest at short radial distances and highest at greater radial distances. This change is due to the rate of secondary photon generation as a function of distance in water. Neutrons emitted from the point source need to undergo sufficient incoherent scattering and capture interactions to create secondary photons, resulting in a $g_P(r)$ shape for secondary photons that is significantly different from those

of conventional brachytherapy sources. Furthermore, there is not a strong correlation between $g_P(r)$ and neutron energy for secondary photons. For $r < 5$ cm, $g_P(r)$ is nearly constant due to the rate of secondary photon generation; however, $g_P(r)$ increases as neutron energy increases for $r \geq 5$ cm.

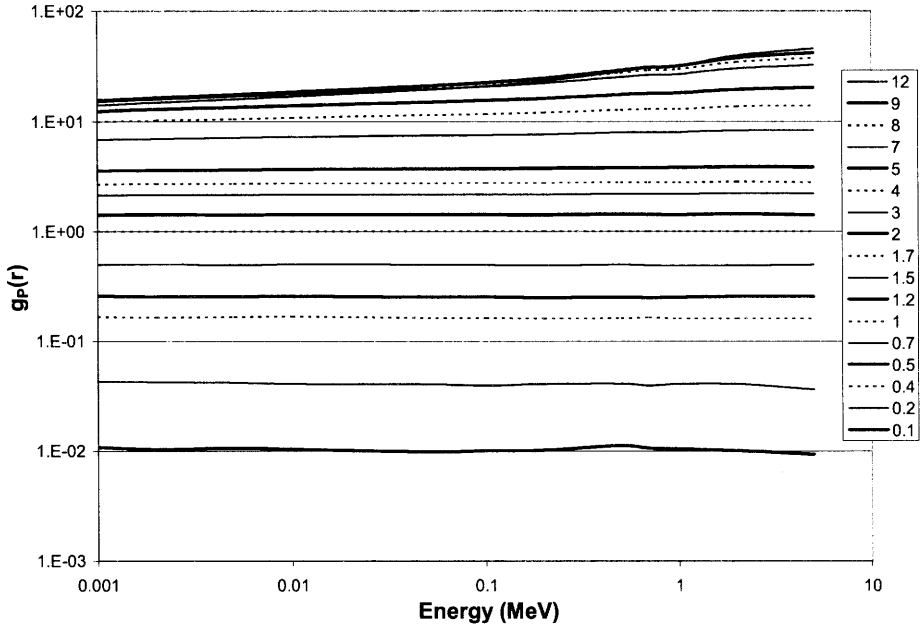

Figure 3.1.6: MC-calculated $g_P(r)_{15}$ for secondary photons plotted as a function of neutron energy for $0.1 \leq r \leq 12$ cm. For $r \leq 5$ cm, $g_P(r)$ is approximately constant as a function of energy.

Comparison of the ICRU 63-modified F4 tally and F6 tally for neutron $g_P(r)_{15}$ is shown in **Figure 3.1.7** in the absence of $S(\alpha,\beta)$.

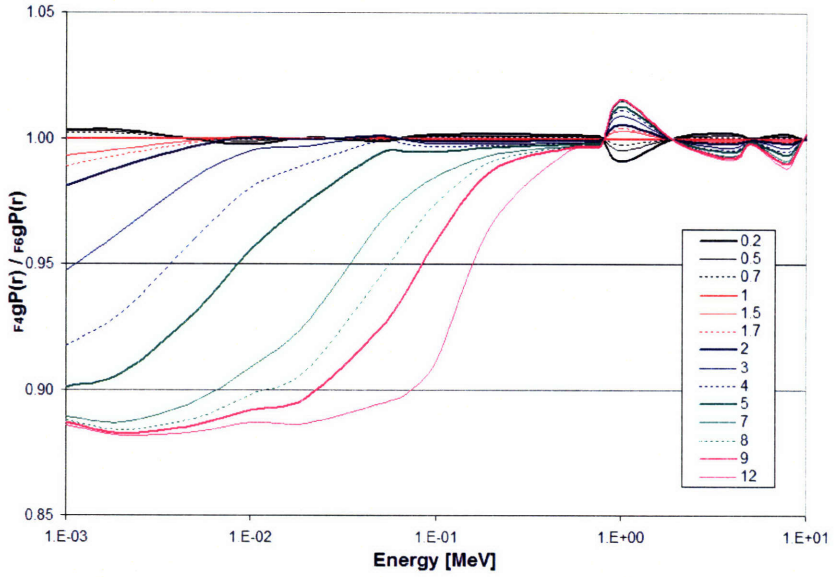

Figure 3.1.7: Ratio of $g_P(r)_{15}$ calculated using the ICRU 63-modified F4 tally to the F6 tally.

As shown in **Figure 3.1.7**, F6-calculated physical dose is approximately 10% lager at $r \geq 7$ cm for neutron energies below 0.01 MeV. The ratio converges above 1 MeV; although, slight variations (< 2%) are evident at higher neutron energies. The difference between the two methods results from the contributions of neutrons below the lowest energy reported in ICRU 63 (2.5×10^{-8} MeV). MCNP5 tracks neutrons with energies as low as 10^{-11} MeV; thus, ICRU 63-modified F4 tallies employ a constant kerma coefficient for neutrons below 2.5×10^{-8} MeV. Inclusion of thermal neutron scattering factors, $S(\alpha,\beta)$, increased the difference between ICRU 63-adjusted F4 and F6 results due to the increase in the population of thermal neutrons ($E_n < 10^{-8}$ MeV).

3.1.4.3 F(r,θ)

Figure 3.1.8 shows F(0.5,θ) for an active length of 5 mm as a function of neutron energy. In contrast to **Figure 2.1.3** that demonstrates a significant increase in F(0.5,θ) near the long axis for low-energy photons, F(0.5,θ) for neutrons increased by approximately 7% for 0.001 MeV neutrons along the source long-axis. As neutron energy increased beyond 1 Mev, F(0.5,θ) approached unity.

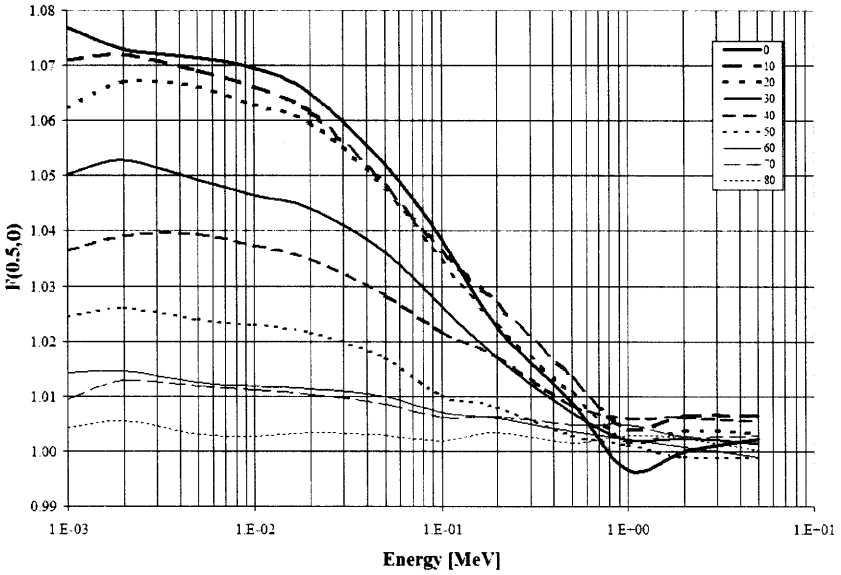

Figure 3.1.8: F(0.5,θ) as a function of energy for L = 0.5 cm.

As r is increased, the shapes of the curves in **Figure 3.1.8** remain, but the magnitude of the values was reduced. For example, F(r,30°) is 1.05 and 1.03 at r = 0.5 and 2.0 cm, respectively.

As the active length is reduced, F(r,θ) approaches unity. For L = 0.1 cm, F(0.5,0°) is 1.01 and is unity at F(2.0,0°). **Table 3.1.2** shows F(0.5,θ) values for increasing neutron energy and active length.

Table 3.1.2: 2D anisotropy function data for two active lengths at 0.001, 0.01, 0.1, and 1 MeV neutrons. L = 0.1 and 0.5 cm were employed to show variations in F(r,θ) as a function of both active length and energy for an un-encapsulated neutron-emitting line source. Note that only contributions due to neutrons are included.

	F(0.5,θ)							
	0.001 MeV		0.01 MeV		0.1 MeV		1 MeV	
L (cm) =	0.1	0.5	0.1	0.5	0.1	0.5	0.1	0.5
0°	*1.015*	1.08	*1.012*	1.07	*1.008*	1.04	*1.008*	1.00
10°	1.00	1.07	1.00	1.07	1.00	1.04	1.00	1.00
20°	1.00	1.06	1.00	1.06	1.00	1.03	1.00	1.00
30°	1.00	1.05	1.00	1.05	1.00	1.03	1.00	1.00
40°	1.00	1.04	1.00	1.04	1.00	1.02	1.00	1.00
50°	1.00	1.02	1.00	1.02	1.00	1.01	1.00	1.00
60°	1.00	1.01	1.00	1.01	1.00	1.01	1.00	1.00
70°	1.00	1.01	1.00	1.01	1.00	1.01	1.00	1.00
80°	1.00	1.00	1.00	1.00	1.00	1.00	1.00	1.00

3.1.5 *CONCLUSIONS*

Monoenergetic virtual neutron point sources were utilized to examine characteristics of neutron brachytherapy. As for photon sources, $g_P(r)$ for neutron sources was found to be sensitive to phantom size; however, partial scatter effects for neutron radiation did not vary strongly as a function of phantom size. For a given neutron energy spectrum, a correction factor could be obtained when calculating dose in a partial scatter environment.

Furthermore, Monte Carlo methods were varied to evaluate methodologies for calculating AAPM TG-43 brachytherapy dosimetry parameters. Inclusion of the neutron $S(\alpha,\beta)$ thermal scattering factor was found to impact calculations of brachytherapy dosimetry parameters for neutrons below 1 MeV in energy. Comparisons of ICRU 63-modified F4 results were notably different from cell-heating tallies (F6) due to MCNP5 tracking neutrons with energy below 2.5×10^{-8} MeV. Dosimetry investigators using ICRU63-modified F4 tallies should evaluate the neutron spectrum to determine whether thermal neutrons will contribute significantly to kerma at the point of calculation. Furthermore, the differences between calculation methodologies were strongly dependent on radial distance which engenders moderation to thermal neutron energies.

3.2 Clinical brachytherapy dosimetry parameters and mixed-field dosimetry for a high dose rate Cf-252 brachytherapy source.[†]

3.2.1 *ABSTRACT*

Since the early 1970's, thousands of patients have been treated worldwide using low dose rate (LDR) californium-252 brachytherapy sources. With recent advances in radiochemistry for concentrating the radionuclide and increasing the effective specific activity, there is now potential for fabrication of high dose rate (HDR) ^{252}Cf

[†] Reproduced from: C. S. Melhus, M. J. Rivard, B. L. Kirk, and L. C. Leal, "Clinical brachytherapy dosimetry parameters and mixed-field dosimetry for a high dose rate Cf-252 brachytherapy source," The Monte Carlo method: Versatility unbounded in a dynamic computing world, Amer Nuc Soc, p. 269 (2005).

brachytherapy sources. Consequently, the mixed-field radiation dose distributions from this novel source type must be characterized preceding delivery of patient treatments. Towards clinical implementation of HDR ^{252}Cf brachytherapy at Tufts-New England Medical Center, the mixed-field dosimetry for this source type has been examined using Monte Carlo methods (MCNP5) and compared to dose distributions produced by traditional HDR ^{192}Ir brachytherapy sources and other medically acceptable sources. The mixed-field dose distribution in the vicinity of a proposed HDR ^{252}Cf brachytherapy source was calculated in a spherical phantom composed of water. The ^{252}Cf neutron energy spectrum was modeled using the ENDF7205 energy spectrum as currently recommended by NIST. The ^{252}Cf photon energy spectrum was modeled using the bare ^{252}Cf source spectrum as measured by Skarsvåg *et al.* (Phys Rev C, 1980). The source capsule was composed of a Pt/Ir-10% alloy, with the radioactive source modeled as a cylindrical Pd wire. A ^{252}Cf source active length of 5.0 mm was used. The MCNP F4 and F6 (track length estimate of energy flux and deposition, respectively) calculation tallies were utilized for determining various dosimetric components. These include the source photon, neutron capture photon, and fast neutron dose components. Calculations were performed in a polar coordinate system to readily permit conversion of dose distribution results into the AAPM TG-43U1 dosimetry formalism for extracting clinical dosimetry parameters. Using this dosimetry formalism, results indicated that dosimetry parameters for HDR ^{252}Cf sources did not significantly differ from those determined for LDR ^{252}Cf sources. These data may now be integrated into brachytherapy treatment planning software to permit clinical implementation of HDR ^{252}Cf brachytherapy.

3.2.2 INTRODUCTION

In the first proposed medical application of ^{252}Cf brachytherapy, a preliminary 1D dose distribution was shown comparing the estimated localized dose deposition from an implanted source to that expected from an external collimated beam.[35] Although the figure clearly demonstrated sparing of healthy tissue through administering interstitial or intracavity radiation therapy, the figure could not be utilized towards implementing treatment planning of ^{252}Cf brachytherapy. Many authors subsequently improved upon the 1D characterization using experimental and calculative techniques to either determine the transverse plane dose or compute an *along-and-away* dose rate table. Anderson

collected and compared the results of nine publications in 1973, and recommended the data of Colvett *et al.* (1972) for describing the applicator tube type source, an LDR source design.[43]

Although Anderson noted that additional dosimetry measurements were warranted, few studies of ^{252}Cf brachytherapy dosimetry parameters were published until the 1992 Yanch and Zamenhof Monte Carlo study in support of boron neutron capture therapy, which presented *along-and-away* dose rate tables.[44] The AAPM Task Group No. 43 report, published in 1995, established a factorized, polar coordinate system for representing the dose distribution about a brachytherapy source.[10] The TG-43 dosimetry formalism improved the accuracy of reproducing dose distributions towards clinical implementation, compared to 2D interpolations between data points on an *along-and-away* table. The TG-43 formalism also provided a means for evaluating similar brachytherapy source designs through direct comparison of the different parameters, *e.g.*, radial dose function g(r) or anisotropy function ϕ_{an} (r). Rivard *et al.* (1999) first applied the TG-43 methodology to the neutron absorbed dose from an LDR ^{252}Cf applicator tube type source.[93]

TG-43 was recently evaluated and updated.[20] The updated report was limited to ^{103}Pd and ^{125}I sources due to uncertainties involved in applying the methodology to high-energy and/or mixed-field radiations. In this study, the TG-43U1 methodology was applied to the neutron and photon radiations from a theoretical HDR ^{252}Cf source.

3.2.3 MATERIALS AND METHODS

3.2.3.1 Monte Carlo source model geometry

The HDR ^{252}Cf source is shown in **Figure 3.2.1**. A right cylinder with an active length L = 5.00 mm and a radius of 0.39 mm was used as the source volume. Although sources manufactured at ORNL are in the from of a Pd:Cf_2O_3 cermet rod, the source material was modeled solely as Pd.[45] For a 2 mg source strength, *i.e.*, 2 mg of ^{252}Cf, the cermet wire is approximately 7% ^{252}Cf by mass. The source was contained in a cylindrical Pt/Ir-10% capsule with an outer length of 8.80 mm and outer radius of 0.648 mm. An air gap between the source element and capsule was not included, and the theoretical capsule was in contact with the source in all directions.

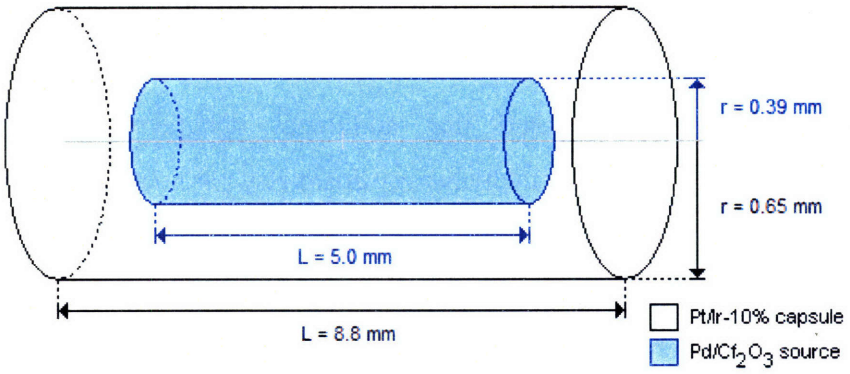

Figure 3.2.1: Schematic of theoretical HDR ^{252}Cf source modeled in this study.

The theoretical source was positioned in the center of a 50 cm diameter water phantom. Assuming standard temperature and pressure, a mass density of 0.998 g cm^{-3} for water was applied, and the S(α,β) thermal neutron scattering library LWTR.60t was selected. **Table 3.2.1** shows the elemental composition and density of the materials used in this study, in addition to the photon and neutron cross-section libraries called.

Table 3.2.1: The MCNP5 cross-section library called for neutrons and photons (n / p) and the nuclide mass composition of the three materials included in the simulations.

Nuclide	cross-section libraries n/p	Mass percent of material H_2O	Pd-Cf_2O_3	Pt/Ir-10%
^{1}H	66c / 04p	11.19		
^{16}O	66c / 04p	88.81		
^{106}Pd	66c / 04p		100.00	
^{191}Ir	66c / 04p			3.73
^{193}Ir	66c / 04p			6.27
Pt	42c / 04p			90.00
	ρ [g cm^{-3}]	0.998	12.0	21.505

3.2.3.2 Monte Carlo tally types and simulation defaults

Version 5 of the Monte Carlo N-Particle Transport Code System (MCNP5) was used to perform radiation transport calculations.[67] Two separate simulations were performed to assess the dose distribution from neutrons and photons emitted by ^{252}Cf. The first used MODE N P to determine the dose from neutrons and from photons induced through neutron transport as a result of capture or inelastic scattering, hereafter called

"secondary" photons. The second set of simulations used MODE P to predict the dose distribution from photons emitted directly from ^{252}Cf, referred to as "primary" photons.

For both MODE N P and MODE P calculations, the track length estimate of cell-heating tally (F6) was employed to determine the energy deposited in the cell in units of MeV g^{-1} per source particle. In addition, at 11 radial distances between 0.75 and 17.5 cm, F6 and F4 (track-length estimator [cm^{-2}]), tallies were calculated at 38 energies between 0 and 20 MeV for neutrons, and F6, F4, and *F4 (track-length estimator of energy flux [MeV cm^{-2}]) tallies were determined at 0.05 MeV increments between 0 and 8.35 MeV for primary and secondary photons.

For neutron transport, comparison of F6 and F4 results were evaluated to ensure that energy deposition closely matched neutron kerma coefficients published by the International Commission on Radiation Units and Measurement (ICRU) in Report 63.[91] Photon transport results were similarly appraised by comparing the ratio of F6 and *F4 results to the appropriate mass-energy attenuation coefficient published by NIST.[71]

Photo-nuclear physics (PHYS:P) was not incorporated because (γ,n) cross-sections for the materials in **Table 3.2.1** are negligible below 10 MeV.[71] Preliminary analyses were performed using 10^8 histories for MODE N P neutron transport equations and 10^9 histories for MODE P primary photon transport. Variance reduction techniques were not employed.

3.2.3.3 ^{252}Cf radiation spectrum

Spontaneous fission of ^{252}Cf occurs in 3.092% of disintegrations, and results in the emission of 2.314 x 10^9 neutrons s^{-1} mg^{-1} and 1.320 x 10^{10} photons s^{-1} mg^{-1}. The neutron energy spectrum was modeled using data measured by Mannhart and published in the Evaluated Nuclear Data Files (ENDF/B-VI) by the Cross-Section Evaluation Working Group at Brookhaven National Laboratory in 1991.[92,94]

Photon energy spectra were modeled using data published by Skarsvåg (1980) for energies between 0.114 and 2.54 MeV and Verbinski *et al.* (1973) for energies between 2.54 and 8.5 MeV.[95,96] The Skarsvåg-Verbinski data comprises 23 energy bins between 0 and 8.5 MeV, but does not include delayed emissions from the relaxation of fission products. Additional Monte Carlo simulations were performed using values

recommended by Knauer *et al.* (1991).[97] The Knauer *et al.* spectrum includes thirteen 0.5 MeV energy bins between 0 and 6.5 MeV, and nearly 50% of the photons are emitted by fission products below 2.0 MeV. The average energy is 0.72 and 0.77 MeV for the Skarsvåg-Verbinski and Knauer *et al.* spectra, respectively.

The ENDF do not include data for photon radiation from ^{252}Cf. Additional measurements of ^{252}Cf photon radiation are needed to improve accuracy and consistency of future computational studies.

3.2.3.4 Dosimetry methodology

The TG-43U1 protocol for the calculation of brachytherapy dosimetry parameters was followed, including the nine specifications for reporting Monte Carlo methodology. Both 1D and 2D parameters were determined for a theoretical encapsulated HDR ^{252}Cf source. While the protocol includes only low-energy photon-emitting radionuclides, the methodology was applied towards describing the mixed-field dose distribution about a ^{252}Cf source. Similar utilization of the original Task Group No. 43 methodology has been made by Rivard *et al.* and by Rivard for low-dose rate ^{252}Cf neutron dosimetry.[93,30]

The dosimetry parameters g(r), F(r,θ), and $\phi_{an}(r)$ were determined using a polar coordinate sampling space similar to that described by Rivard *et al.*[69] Radial sampling at twelve points from 0.5 to 20 cm was taken on the transverse plane with step sizes varying between 0.5 and 5 cm. Radial sampling did not occur in the outermost 5 cm of the phantom due to the inadequate amount of backscatter material at the phantom edge. Sampling off the transverse plane was taken in 1° polar angle increments. The source and resultant dose distribution were assumed to be symmetric about the transverse plane, cylindrically symmetric about the source long axis, and azimuthal angle data were averaged. The $g_P(r)$ for total photon radiation was calculated from a weighted sum of primary and secondary ^{252}Cf photon radiation data. A multiplicative factor of 1.320 x 10^{10} s^{-1} mg^{-1} was applied to the primary radiation data and 2.314 x 10^9 s^{-1} mg^{-1} to the secondary radiation data to account for the differential emission rate of ^{252}Cf primary photons with respect to secondary photons induced by spontaneous fission neutrons.

In this study, TG-43U1 brachytherapy dosimetry parameters computed for the hypothetical HDR ^{252}Cf source described above are determined and compared to similar

data published for LDR ^{252}Cf applicator tube (AT) type sources. In addition, dosimetry parameters for common medical radionuclide sources are presented in contrast to the mixed-field behavior exhibited by HDR ^{252}Cf.

3.2.4 RESULTS AND DISCUSSION

Statistical uncertainties in F6 tallies of neutron dose on the transverse plane ranged from 0.1% to 0.4% from 0.5 to 20 cm, and 0.4% to 0.6% at the same distances for primary photon dose. Due to smaller solid angles, the statistical uncertainties increased for positions towards the source long axes. At 5°, the statistical uncertainties of neutron dose ranged from 0.3% to 1.2% from 0.5 to 20 cm, with values of 1.7% to 2.1% for photon dose at these same distances. Statistical uncertainties for photon transport were higher due to the lower density of energy deposition in the phantom, because the mean free path for photons ~ 1 MeV is longer than the average distance per neutron collision at the same energy.

3.2.4.1 Dosimetric coefficients

For neutron transport simulations, comparison of F6 and F4 tallies provide an estimate of fluence-to-dose kerma coefficients, which are compared to values published in ICRU 63 in **Figure 3.2.2**. Similarly, the ratio of F6 and *F4 tallies for photon transport were taken to estimate mass-energy absorption coefficients, and are compared to coefficients published by NIST in **Figure 3.2.3** for 12 positions along the transverse axis.

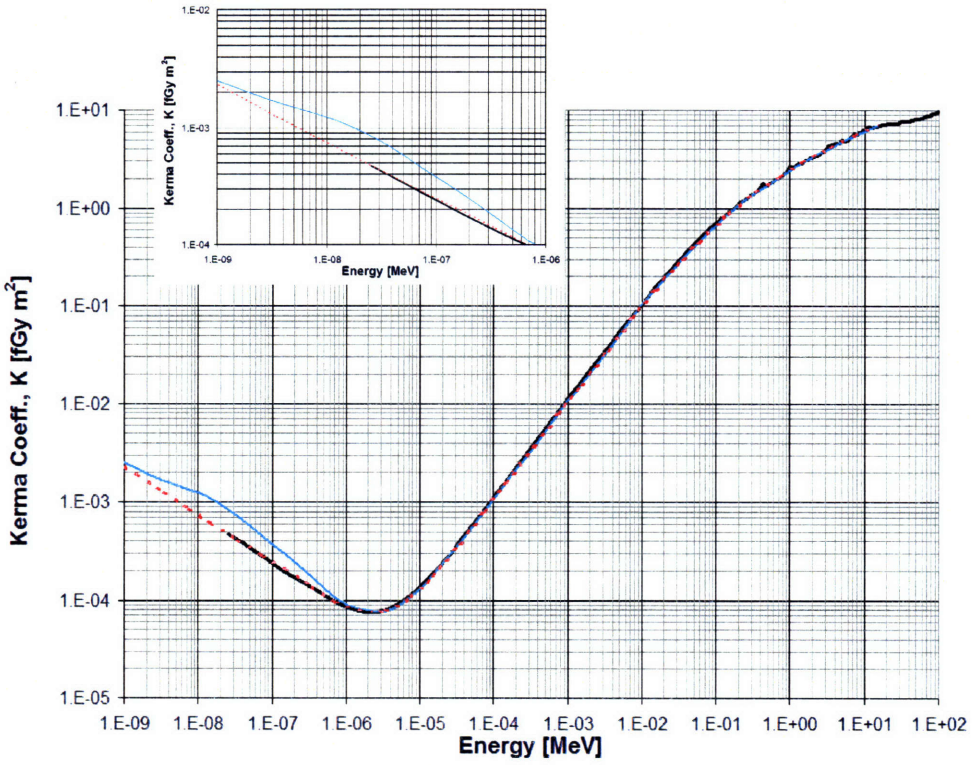

Figure 3.2.2: Comparison of liquid water neutron kerma coefficients published in ICRU 63[91] and those determined using MCNP5. The MC-calculated data are presented for simulations including and excluding the thermal neutron scattering factor S(α,β), which impacts energy deposition below 1 eV (see insert).

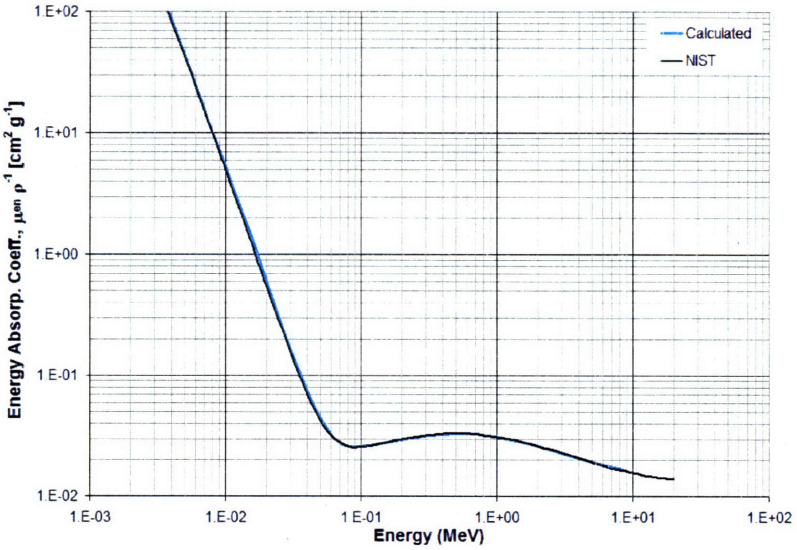

Figure 3.2.3: Comparison of liquid water photon energy-absorption coefficients calculated using MCNP5 and those of Hubbell and Seltzer.[71]

Neutron kerma coefficients calculated using MCNP5 are in good agreement with those published in ICRU Report 63 over seven decades of energy between 1 eV and 20 MeV. For thermal to low-energy neutrons (below 1 eV), there is a factor of 1.5 difference between this study and ICRU 63 for simulations employing the thermal neutron scattering factor $S(\alpha,\beta)$ for light water. Removal of $S(\alpha,\beta)$ results in better agreement to ICRU 63, with an average ratio of 0.98 ± 0.04 ($\pm$ 1 s.d.) at 27 data points over nine orders of magnitude.

For photon energy deposition, a ratio of energy absorption coefficients calculated with MCNP5 and values published by NIST had an average of 1.01 ± 0.04 ($\pm$ 1 s.d.) at 19 points over four decades. For photon energies below 0.1 MeV, MCNP5 calculated values were found to be sensitive to energy bin width as a result of rapid adsorption of low-energy photons.

3.2.4.2 Radial dose function g(r)

The HDR ^{252}Cf radial dose functions are shown in **Figure 3.2.4** for neutron radiation and in **Figure 3.2.5** for primary photon radiation. In **Figure 3.2.4**, $g_P(r)$ for ^{252}Cf neutrons is compared to similar data published by Rivard (2000) and by Yanch and Zamenhof (1992) for an AT type source (L = 1.5 cm). Radial dose function for primary photons displayed in **Figure 3.2.5** is compared to photon data calculated from Yanch and Zamenhof, to ^{192}Ir data published in TG-43, and to ^{125}I data for the Best Medical model 2301 seed published in AAPM report TG-43U1.

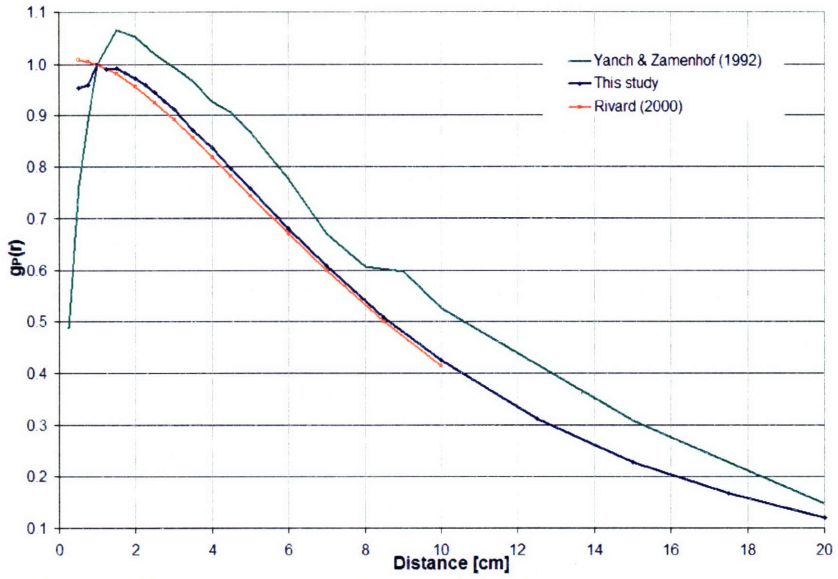

Figure 3.2.4: Radial dose functions for HDR ^{252}Cf neutrons compared to similar results for an LDR ^{252}Cf AT-type source published by Rivard (2000) and by Yanch and Zamenhof (1992).

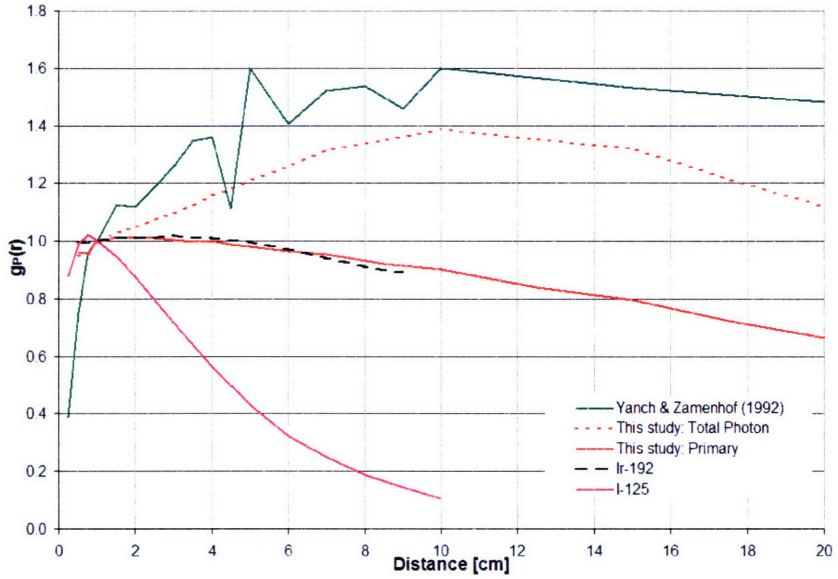

Figure 3.2.5: Radial dose function for ^{252}Cf photons in comparison to data published by Yanch and Zamenhof. In addition, $g_P(r)$ for two photon-emitting brachytherapy sources, the Best Medical model 2301 ^{125}I seed and a ^{192}Ir source, is shown.

Rivard determined the radial dose function using MCNP4B for a ^{252}Cf point source in a 30 cm water phantom assuming a Maxwellian neutron energy spectrum. Yanch and Zamenhof used MCNP3B to estimate $g_P(r)$ in water from an applicator tube

(AT) type source in a cylinder of height 60 cm and radius 30 cm with a Watt fission spectrum representing the ^{252}Cf neutron emissions. Ratios of $g_P(r)$ to Rivard (2000) have an average value of 0.98 ± 0.03 (± 1 s.d.) between radial distances of 1 and 10 cm. Aside from utilizing a different neutron spectral model, differences in the neutron $g_P(r)$ data of Yanch and Zamenhof and this work are largely due to the neutron cross-sections and kerma coefficients called by MCNP3B compared to the modern, up-to-date values in MCNP5. Further, Yanch and Zamenhof did not employ $S(\alpha,\beta)$ in their simulation to account for neutron moderation in liquid water. The discontinuity at $g_P(9)$ in the Yanch and Zamenhof data likely resulted from the precision of the data presented, and is not supported by the results of Rivard or this study.

Because secondary photons are induced outside of the source capsule, the total photon $g_P(r)$ builds to a maximum value at a depth of approximately 10 cm. The total photon radial dose function of Yanch and Zamenhof, calculated by subtracting the neutron dose from the total (neutron and photon) dose, exhibits similar behavior and supports the results of this study.

The low-energy radiations emitted by ^{125}I provide a steep radial dose function in contrast to ^{252}Cf neutrons and photons, due to the rapid attenuation of photons below 0.05 MeV in water. High energy photons from ^{192}Ir have an average energy of 0.37 MeV, and a $g_P(r)$ similar to that of ^{252}Cf primary photons. At r = 9 cm, $g_P(r)$ decreases only 10% for ^{252}Cf and ^{192}Ir photons, but there is a reduction of over 50% reduction for ^{252}Cf neutrons over the same distance. Thus, the radial dose function behavior of radiation emitted by HDR ^{252}Cf is within the range of data presented for commonly applied medical radionuclides.

Over all radial distances, the ratio of $g_P(r)$ results for the Skarsvåg-Verbinski and Knauer *et al.* primary ^{252}Cf photon spectra had an average value of 0.98 ± 0.01 (± 1 s.d.). The ratios showed a slight increase with radial distance, such that the values were 0.99 and 0.97 at 2 and 20 cm, respectively. Thus, calculation of $g_P(r)$ using the ^{252}Cf photon spectrum recommended by Knauer *et al.*, which includes decay photons from fission products, was comparable to that determined using the primary photon emissions of Skarsvåg-Verbinski.

3.2.4.3 Anisotropy function F(r, θ)

Table 3.2.2 and **Table 3.2.3** displays the 2D anisotropy function data for neutron and photon radiation, respectively, for the HDR source shown in **Figure 3.2.1**. In **Table 3.2.3**, the F6 tally results for primary and secondary photons were summed prior to calculating F(r,θ), as described above. Data are presented in 10° increments, representing the average of three degrees about each value, *e.g.*, the data for 50° is the average of 49°, 50°, and 51°. Because of source symmetry, data equally spaced above and below the transverse plane was averaged to determine $F_{90}(r,\theta)$, *e.g.*, the data for 20° is the average of 20° and 160°.

Table 3.2.2: 2D anisotropy functions for neutrons emitted from the HDR ^{252}Cf source.

	$F_{90}(r,\theta)$									
r [cm]	0^0	10^0	20^0	30^0	40^0	50^0	60^0	70^0	80^0	90^0
0.5	0.97	0.98	0.99	0.99	1.00	1.00	1.00	1.00	1.00	1.00
1.0	0.97	0.98	0.99	1.00	1.00	1.00	1.00	1.00	1.00	1.00
1.5	0.98	0.98	0.99	1.00	1.00	1.00	1.00	1.00	1.00	1.00
2.0	0.98	0.98	0.99	1.00	1.00	1.00	1.00	1.00	1.00	1.00
2.5	0.98	0.98	0.99	1.00	1.00	1.00	1.00	1.00	1.00	1.00
3.0	0.97	0.98	0.99	1.00	1.00	1.00	1.00	1.00	1.00	1.00
4.0	0.98	0.98	1.00	1.00	1.00	1.00	1.00	1.00	1.00	1.00
5.0	0.98	0.99	0.99	1.00	1.00	1.00	1.00	1.00	1.00	1.00
7.0	0.97	0.98	0.99	1.00	1.00	1.00	1.00	1.00	1.00	1.00
10.0	0.98	0.99	1.00	1.00	1.00	1.00	1.00	1.00	1.00	1.00
15.0	0.99	0.99	0.99	1.00	1.00	1.00	1.00	1.00	1.00	1.00
20.0	1.00	0.98	0.99	1.00	1.00	1.00	1.00	1.01	1.00	1.00

Table 3.2.3: 2D anisotropy functions for total photon (primary and secondary) radiation emitted from the ^{252}Cf source.

	$F_{90}(r,\theta)$									
r [cm]	0^0	10^0	20^0	30^0	40^0	50^0	60^0	70^0	80^0	90^0
0.5	0.70	0.72	0.87	0.93	0.97	0.98	0.99	1.00	1.00	1.00
1.0	0.67	0.72	0.86	0.92	0.96	0.98	0.99	0.99	1.00	1.00
1.5	0.70	0.73	0.86	0.92	0.96	0.98	0.99	0.99	1.00	1.00
2.0	0.70	0.74	0.87	0.92	0.96	0.98	0.99	1.00	1.00	1.00
2.5	0.69	0.75	0.87	0.92	0.95	0.98	0.99	0.99	1.00	1.00
3.0	0.71	0.76	0.87	0.93	0.96	0.98	0.99	1.00	1.00	1.00
4.0	0.73	0.79	0.88	0.93	0.96	0.98	0.99	1.00	1.00	1.00
5.0	0.76	0.81	0.89	0.94	0.96	0.98	0.99	1.00	1.00	1.00
7.0	0.71	0.76	0.87	0.93	0.96	0.98	0.99	1.00	1.00	1.00
10.0	0.73	0.79	0.89	0.93	0.96	0.98	0.99	1.00	1.00	1.00
15.0	0.88	0.89	0.94	0.96	0.98	0.98	0.99	1.00	1.00	1.00
20.0	0.88	0.90	0.94	0.97	0.98	0.99	0.99	1.00	1.00	1.00

For both neutrons and photons, 99.9% of $F_{90}(r,\theta)$ data points were within 1% of the $F(r,\theta)$ for all radial distances and angles. For neutrons, 99% of the data were within ± 1% of the average value. For the photon data, adherence within ± 1% of the average values was 77% and increased to 98% for ± 5% agreement between $F_{90}(r,\theta)$ and $F(r,\theta)$.

Table 3.2.3 shows that anisotropy of the total photon emissions from a HDR ^{252}Cf source increases with decreasing θ and with decreasing radial distance, an effect that is exhibited by most photon-emitting brachytherapy sources described in TG-43U1. In contrast, 2D neutron dose deposition demonstrates only a 3% deviation along the source long-axis at a distance of 0.5 cm. This effect, attributed to the low rate of interaction between ^{252}Cf neutrons and the source encapsulation, was also noted in Rivard *et al.* and Rivard.[93,30]

Impact of the choice of ^{252}Cf primary photon spectrum on $F_{90}(r,\theta)$ is shown in **Table 3.2.4** for selected radial distances. Over all distances, there was an average ratio of 1.04 ± 0.02 (± 1 s.d.) along the long axis ($\theta = 0^0$) and approaches unity towards the transverse plane with a standard deviation below 0.01 for 50^0, 60^0, 70^0, and 80^0.

Table 3.2.4: Ratio of the 2D anisotropy functions for ^{252}Cf primary photon emissions between the Knauer *et al.* and the Skarsvåg-Verbinski spectra. Data recommended by Knauer *et al.* includes estimates of the delayed photon intensity from the decay of ^{252}Cf fission products.

	$F_{90}(r,\theta)^{\text{Knauer } et\ al.} / F_{90}(r,\theta)^{\text{Skarsvåg-Verbinski}}$									
r [cm]	0^0	10^0	20^0	30^0	40^0	50^0	60^0	70^0	80^0	90^0
0.5	1.06	1.06	1.04	1.02	1.01	1.00	1.00	1.00	1.00	1.00
1.0	1.07	1.05	1.03	1.02	1.01	1.01	1.00	1.00	1.00	1.00
1.5	1.03	1.05	1.03	1.02	1.01	1.00	1.00	1.00	1.00	1.00
2.0	1.02	1.05	1.02	1.02	1.01	1.00	1.00	1.00	1.00	1.00
3.0	1.05	1.04	1.02	1.02	1.02	1.00	1.00	1.00	1.00	1.00
5.0	1.04	1.03	1.03	1.02	1.01	1.01	1.00	1.00	1.00	1.00
10.0	1.05	1.04	1.03	1.02	1.02	1.00	1.00	1.00	1.00	1.00
20.0	1.03	1.02	1.01	1.01	1.01	1.00	1.00	1.01	1.00	1.00

As such, utilization of the photon data of Knauer *et al.* will not significantly perturb the 2D anisotropy about the HDR ^{252}Cf source. The largest effects will occur towards the ends of the source at small radial distances. As expected, the 2D anisotropy function values using the photon energy spectrum from Knauer *et al.* were higher than the 2D anisotropy function values using the photon energy spectrum from Skarsvåg-Verbinski. This was due to the slightly higher average photon energy of Knauer *et al.* and increased path length through the capsule at oblique angles ($\theta \sim 0°$) along the source long-axis.

3.2.4.4 1D anisotropy function $\phi_{an}(r)$

1D anisotropy functions $\phi_{an}(r)$, calculated from the 2D anisotropy data in **Tables 3.2.2** and **3.2.3**, are displayed in **Table 3.2.5** for neutron and total photon radiations. For comparison, $\phi_{an}(r)$ for two photon emitting brachytherapy sources are included: the Best Medical model 2301 ^{125}I seed characterized in TG-43U1 and a high-energy ^{192}Ir source described in TG-43.

Table 3.2.5: Comparison of 1D anisotropy functions between the neutron and photon emissions from a HDR ^{252}Cf source and two commonplace photon emitting medical sources. ^{192}Ir data was taken from TG-43, and ^{125}I data was the Best Medical model 2301 described in TG-43U1. Radial dose function $g_P(r)$ data are included for reference.

	$\phi_{an}(r)$				$g_p(r)$	
Radius	^{252}Cf	^{252}Cf	^{192}Ir	^{125}I	^{252}Cf	^{252}Cf
[cm]	neutrons	photons	photons	photons	Neutrons	photons
0.5	1.21	1.18			0.953	0.947
1.0	1.12	1.09	0.991	0.945	1.000	1.000
1.5	1.11	1.07			0.992	1.029
2.0	1.10	1.07	0.947	0.987	0.973	1.047
2.5	1.10	1.07			0.944	1.073
3.0	1.10	1.07	0.897	0.968	0.912	1.096
4.0	1.10	1.06	0.942	0.971	0.838	1.159
5.0	1.10	1.07	0.998	0.969	0.758	1.209
7.0	1.09	1.06	0.965	0.969	0.609	1.312
10.0	1.10	1.06			0.425	1.386
15.0	1.09	1.08			0.228	1.319
20.0	1.10	1.08			0.120	1.120

Compared to conventional photon-emitting brachytherapy sources, e.g., ^{192}Ir and ^{125}I, neutrons and photons from ^{252}Cf exhibit little change in their 1D anisotropy as a function of distance. Within 2 cm, both ^{252}Cf datasets show a steep increase in anisotropy approaching the source capsule.

3.2.5 CONCLUSIONS

Radiation transport simulations were performed to evaluate the dosimetric characteristics of a simplified HDR ^{252}Cf brachytherapy source. Calculations performed to validate the MCNP5 F6 tally in comparison to the *F4 and F4 tallies typically indicated agreement of results with 2%. Subsequent simulations utilized models of ^{252}Cf neutron and photon emission to determine the 2D and 1D brachytherapy dosimetry parameters defined in the AAPM TG-43U1 report. The radial dose function for both neutrons and photons was consistent with previously published values, and within the range of variation exhibited by common medical radionuclide sources. ^{252}Cf neutron radiation exhibited little anisotropy about the plane-symmetric HDR capsule, and concomitant primary and secondary photons showed a general decrease in anisotropy with increasing radial distance, as expected due to scattered radiation. Further,

evaluation of two separate ^{252}Cf primary photon spectra yielded comparable dosimetry parameters.

In conjunction, with an appropriate dose rate constant for this HDR ^{252}Cf source, data presented here may be incorporated into contemporary radiation therapy treatment planning systems towards clinical implementation and patient treatment.

3.3 Monte Carlo validation of clinical brachytherapy dosimetry under partial scatter conditions for neutron-emitting sources

3.3.1 ABSTRACT

Purpose: Monte Carlo models were generated in support of a clinical trial on the effectiveness of neutron-based brachytherapy for a patient treated with a plaque containing LDR Cf-252 AT-Type sources. Because the AAPM brachytherapy dosimetry formalism does not replicate partial scatter conditions of superficial brachytherapy, MC simulations were performed to evaluate treatment time and dose distributions generated using conventional methods.

Method and Materials: Clinical calculations employed the AAPM dosimetry formalism with modified parameters for the neutron dose component. MC simulations utilized MCNP5 and track length estimator tallies. Computations applied a rectilinear mesh to tabulate neutron transport, including induced photons, and primary photon transport in a 14x14x5 cm^3 volume with 9 mm^3 voxels. Patient surface was simulated using a 20 cm radius hemisphere of water, with a corresponding hemisphere of air. For comparison to the AAPM formalism,the air was replaced with water. An RBE of 6 converted results to cGy-eq for the neutron component. Results were normalized to 0.1 mg Cf-252 source strength.

Results: At the 4 mm prescription depth, calculated dose rates were 198 ± 3 and 236 ± 3 cGy-eq h^{-1} at plaque center and 24 mm offset, respectively. The central 4x4 cm^2 area received 281 ± 71 cGy-eq h^{-1}. For comparison, full-scatter simulations yielded 222 ± 2 cGy-eq h^{-1} at plaque center and 299 ± 72 cGy-eq h^{-1} over a 4x4 cm^2 area; although, computation time increased by a factor of 6.6. Dose ratios of full- (4π) to partial-scatter

(2π) environments changed from 1.12 to 1.08 as depth increased from 0.4 to 5 cm. Approximately 90 ± 1% of the dose-equivalent was due to neutrons, while neutron physical dose was 70 ± 1% and 57 ± 2% of the total at 0.4 and 5.0 cm depths, respectively.

Conclusion: Dose can be overestimated upto 10% by assuming full-scatter conditions for Cf-252 plaque brachytherapy. MC simulations are recommended to validate treatment plans generated using conventional methods.

3.3.2 INTRODUCTION

MC simulations were performed in support of a clinical trial on the safety and effectiveness of neutron-based brachytherapy for locally advanced, recurrent, or radio-resistant malignancies. A patient with recurrent disease was treated superficially using a plaque containing eight LDR AT-type ^{252}Cf sources. Because the AAPM brachytherapy dosimetry formalism does not replicate partial scatter conditions of superficial brachytherapy, MC simulations were performed to evaluate treatment time and dose distributions generated using conventional methods.

3.3.3 MATERIALS AND METHODS

Clinical treatment time was calculated with the Philips Pinnacle^3 planning system (v7.6c) using the AAPM brachytherapy dosimetry formalism. In lieu of normalizing source emission rate with the dose rate constant (Λ), calculations were relative to contained ^{252}Cf mass. Source emission rates were 2.31×10^9 neutrons s^{-1} and 1.32×10^{10} primary photons s^{-1} per mg of ^{252}Cf, with the sources containing a total of 0.1 mg.

MC calculations utilized MCNP5 and the DLC-220 cross-section libraries. Two simulations were performed for each calculation: MODE NP for neutron transport, which also tallied secondary photons, and MODE P for primary photon transport. MC-based single-source brachytherapy dosimetry parameters were developed following the recommendations in the AAPM TG-43U1 report.[20] A RBE of 6 was employed to convert neutron physical dose to cGy-eq for low dose rate ^{252}Cf brachytherapy.

Patient skin surface was simulated using a 20 cm radius hemisphere of liquid water (ρ = 0.998 g cm^{-3}), with a corresponding hemisphere of air (ρ = 1.2 mg cm^{-3}). A rectilinear mesh tabulated energy deposited using the F4 tally modified by ICRU 63

kerma factors for neutrons[91] and the *F4 tally modified by NIST energy absorption coefficients for photons.[71] The AT-Type source was modeled following **Ref. 93**, and the MCNP UNIVERSE and transformation (TRN) cards were used to distribute sources into the plaque geometry (**Figure 3.3.1**). In horizontal planes parallel to the plaque, dose was tabulated in 0.2 cm increments over a 14x14 cm^2 grid, repeated in 0.22 cm vertical increments to a depth of 5.6 cm. For comparison to full-scatter conditions employed in the AAPM brachytherapy dosimetry formalism, additional simulations were performed with the air replaced by water.

Adequate starting particle histories were computed to ensure statistical uncertainties below approximately 2% in all voxels in the mesh. Variance reductions techniques were not employed.

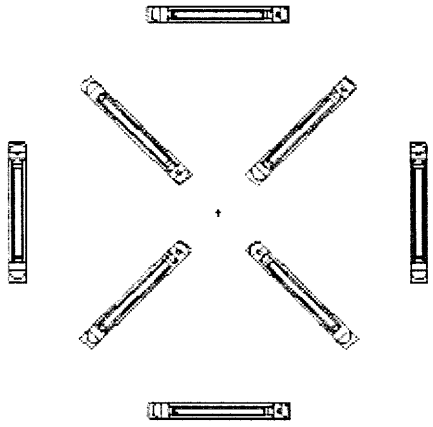

Figure 3.3.1: ^{252}Cf sources arrayed in the plaque geometry.

3.3.4 RESULTS

Isodose contours for the plaque simulation are shown in **Figure 3.3.2** at a depth of 0.4 cm from the surface. Each source can be delineated from the eight regions with dose rates $\geq$ 250 cGy-eq h^{-1}. Central regions of 2x2, 3x3, 4x4, and 5x5 cm^2 have dose-equivalent rates of 237 ± 23, 267 ± 57, 281 ± 71, and 293 ± 76 cGy-eq h^{-1}, respectively, and physical dose rates of 54 ± 6, 61 ± 13, 64 ± 16, and 67 ± 17 cGy h^{-1}, respectively. In these regions, reported uncertainties are standard deviations representing dose rate variation within the mesh.. Depending on the lesion size, daily 2 Gy-eq low dose rate treatments can be delivered in less than a one-hour treatment session.

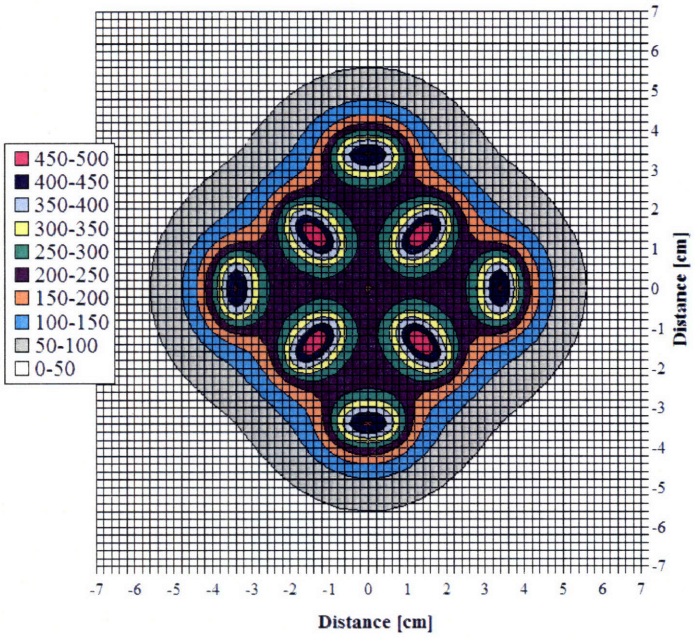

Figure 3.3.2: Isodose distribution in 50 cGy-eq h^{-1} increments at a depth of 0.4 cm, including both neutron and photon dose components.

For full-scatter calculations in the liquid water sphere, central doses were 257 ± 22, 286 ± 58, 299 ± 72, and 311 ± 78 cGy-eq h^{-1} for 2x2, 3x3, 4x4, and 5x5 cm^2 areas at the center of the plaque, respectively. As such, replacing the hemisphere of air with water increases total dose-equivalent rate by approximately 7%. On the plaque central axis, this effect increases with depth from +12% at 0.4 cm to +7% at 5 cm from the surface and is more pronounced for the photon component. Photon dose rates increased from +20% to +29% over the 0.4 to 5 cm range, while the corresponding neutron increases were +11% to +5%. Thus, overall scatter effects are dominated by the neutron component for dose-equivalent rate calculations, and special consideration is necessary when prescribing physical dose. In addition to the increased dose rate in the full-scatter case, computational time required for radiation transport is increased by a factor of 1.2 and 6.6 for MODE P and MODE NP transport, respectively. This increase in computer time is expected due to the 4π scattering medium in comparison to the 2π plaque model, where the neutrons are unlikely to interact with air.

Dose profiles of the total dose-equivalent are shown in **Figures 3.3.3** and **3.3.4** for the center of the plaque and for a 2.4 cm offset, respectively. As a function of depth,

dose rates at the plaque center did not follow r^{-2} or r^{-1} behavior; instead, dose rates fell exponentially by a factor of –0.458 for neutrons and by –0.345 for photons.

Depth dose values along the central axis in **Figure 3.3.4** (distance = 0 cm) are comparable to those in **Figure 3.3.3**, though narrower due to the offset from plaque center. While the profiles in **Figure 3.3.3** are oriented along the longest dimension of the plaque, the area receiving ≥ 150 cGy-eq h^{-1} at 0.6 cm depth is approximately 6x6 cm^2.

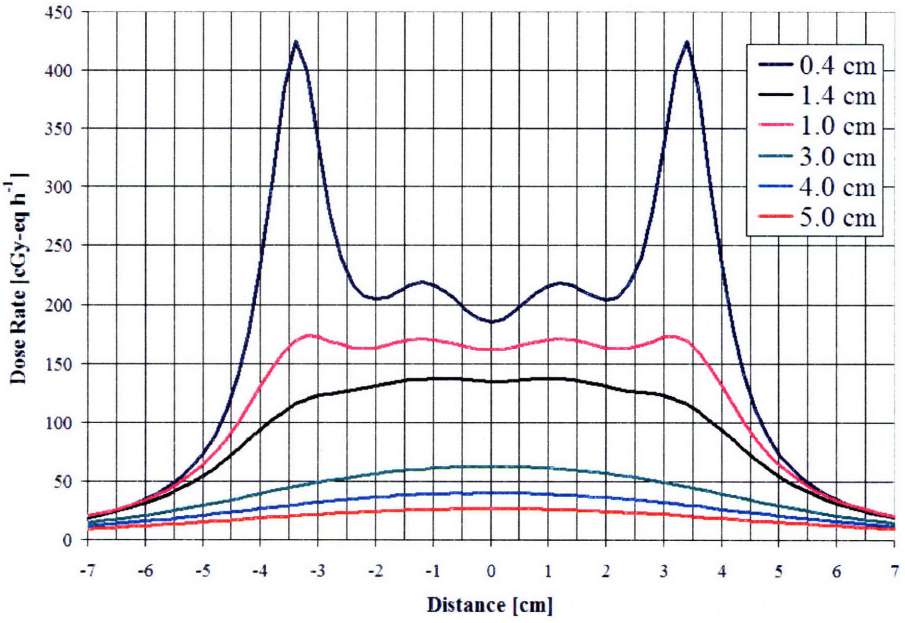

Figure 3.3.3: Dose profiles along the center of the plaque at depths varying between 0.4 and 5 cm. Peaks in the 0.4 cm depth profile are a result of sampling under two sources.

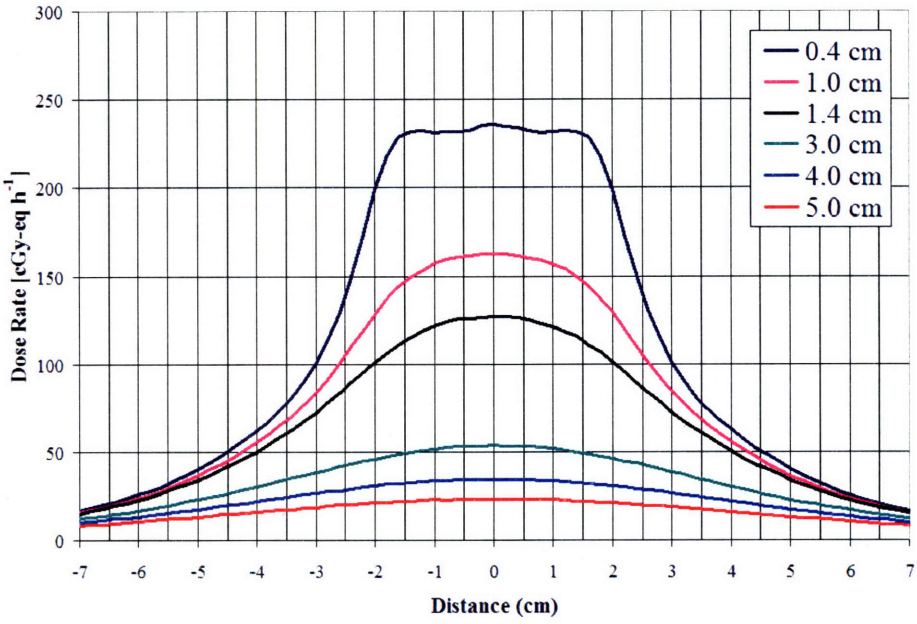

Figure 3.3.4: Dose profiles at a distance of 2.4 cm from the plaque center. Due to the orientation of the plaque (see **Figure 3.3.2**), the dose plateaus are narrower.

3.3.5 CONCLUSIONS

Monte Carlo methods were used to simulate treatment of superficial lesions using ^{252}Cf brachytherapy. These demonstrated that dose-equivalent could be overestimated by upto 10% when using full-scatter conditions in comparison to MC simulation of a plaque.

4 Shielding considerations

4.1 Storage safe shielding assessment for a HDR californium-252 brachytherapy source†

4.1.1 ABSTRACT

In pursuit of implementing HDR ^{252}Cf brachytherapy, a suitable external storage safe must be designed and constructed to store the medical source when not in use. The shielding capabilities of polyethylene, RICORAD™, and Pb were examined for both neutron and photon radiations using Monte Carlo methods. RICORAD™ is a heat-resistant plastic, with 2.00%-mass boron in a polyethylene-based matrix having a mass density of 0.945 g cm^{-3}. Due to the high-hydrogen content, the fission-energy ^{252}Cf neutrons are readily attenuated by RICORAD™ and polyethylene, and the boron loading in RICORAD™ further helps prevent creation of 511 keV gamma-rays from neutron capture by hydrogen. Pb readily attenuates ^{252}Cf photons. Results of shielding calculations using MCNP were incorporated into the design of a spherical RICORAD™/Pb safe for storage of 1 mg of ^{252}Cf that would reduce the external radiation fields to levels below regulatory concerns. Practical considerations governing safe design included exposure levels, material availability, and total safe weight and size. Results are presented per milligram of ^{252}Cf and can be scaled as needed for other source strengths.

† Reproduced from: C. S. Melhus, M. J. Rivard, B. L. Kirk, and L. C. Leal, "Clinical brachytherapy dosimetry parameters and mixed-field dosimetry for a high dose rate Cf-252 brachytherapy source," The Monte Carlo method: Versatility unbounded in a dynamic computing world, Amer Nuc Soc, p. 269 (2005).

4.1.2 INTRODUCTION

Californium brachytherapy was first proposed nearly forty years ago as the promise of radiotherapy with neutrons first became apparent.[35] Since that time, a handful of clinical centers around the world have employed low dose rate (LDR) intra-cavity or interstitial californium therapy to treat tumors from head-to-toe. Thorough reviews of the clinical results and radiobiological advantages have been published by Maruyama.[98,36]

Miniaturized high dose rate (HDR) ^{252}Cf sources (~1 mg) recently became available through advances in radiochemistry.[45] As such, HDR ^{252}Cf brachytherapy sources compatible with modern remote afterloader technology are feasible. For standard-of-care brachytherapy employing a HDR ^{192}Ir source, a tungsten-alloy storage safe has been integrated into the remote afterloading unit. However, it is not feasible to construct a compact storage safe to attenuate the mixed-field radiation emissions from ^{252}Cf due to the increased path length of neutrons and photons in suitably hydrogenous materials in comparison to the shorter path length of ^{192}Ir photons in the W-alloy. Therefore, an external storage safe must be employed. Additionally, to minimize the size of the storage safe, a multiple component shield is needed to address the different requirements of the mixed neutron/photon radiation fields.

In this study, the shielding properties of polyethylene, Pb, and RICORAD™ – a borated polyethylene product manufactured by Reactor Experiments, Inc. (San Carlos, CA)[†] – were investigated using Monte Carlo methods. In addition, preliminary models of a multi-component safe, employing Pb and RICORAD™ to maximize photon and neutron attenuation, respectively, were investigated.

4.1.3 MATERIALS AND METHODS

4.1.3.1 ^{252}Cf radiation spectrum

Californium-252 is one of the few radionuclides that decay via spontaneous fission. One milligram of ^{252}Cf emits 2.314×10^9 neutrons per second through this decay mode, although spontaneous fission accounts for only 3.092% of disintegrations.[45] Historically, ^{252}Cf neutron emission was modeled using either a Maxwellian or Watt

[†] The company has been acquired by Thermo Electron Corporation, Yokohama City, Japan.

fission model[43] and the appropriate built-in MCNP source probability function, *e.g.*, f = -2 or –3 on the SP card, respectively. In this work, neutron emission data published by Mannhart and integrated into the Evaluated Nuclear Data File (ENDF) were used.[92] **Figure 4.1.1** compares the three neutron spectra normalized to unity at the most probable energy: 0.7, 0.9, and 1.2 MeV for the Mannhart, Watt, and Maxwellian models, respectively.

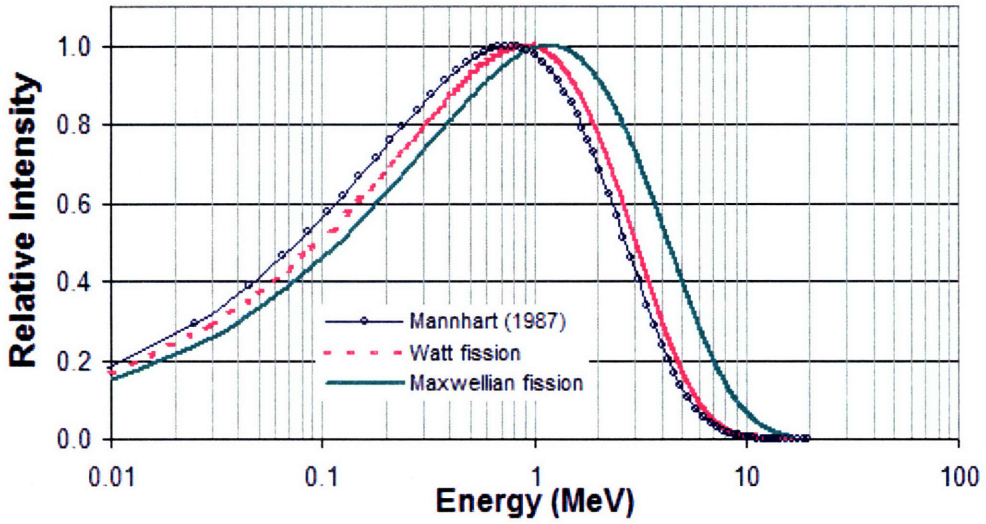

Figure 4.1.1: Comparison of normalized Mannhart ^{252}Cf neutron emission spectrum, Watt fission spectrum, and Maxwellian fission spectrum. In this study, the Mannhart neutron spectrum was utilized.

Prompt ^{252}Cf gamma rays are emitted stochastically through spontaneous fission, but a representative spectrum was not available in the ENDF. Verbinski *et al.* measured the prompt gamma ray emission from ^{252}Cf using 13 energy bins between 0.14 and 10 MeV.[96] Skarsvåg similarly measured the prompt gamma ray spectrum for photons above 0.114 MeV using 18 energy bins, but binned photons above 2.54 MeV.[95] Above 2.54 MeV, the number of gammas per fission was 0.43 and 0.426 and the percent of total emission was 4.42% and 5.46% for Skarsvåg and Verbinski *et al.*, respectively. Thus, the data of Verbinski *et al.*, which had finer energy resolution, was used for prompt gamma ray energies above 2.54 MeV.

The photon emission rate from 1 mg of ^{252}Cf was taken to be 1.3 x 10^{10} s^{-1}, which was employed in shielding calculations performed by Hootman and Stoddard (1971) and by da Silva and Crispim (2001).[49,99] Dividing the neutron emission rate by the average

number of neutrons per fission (3.7676) and multiplying by the average number of prompt photons per fission (9.7), as measured by Skarsvåg, yielded a prompt gamma emission rate of 5.96 x 10^9 s^{-1}. There is a factor of 2.2 between the two values because delayed gamma rays from the decay of fission product progeny were not included by Skarsvåg. Hootman and Stoddard published photon spectral data for fission product gamma rays, but did not cite the source of their spectral data. Additionally, only four energy bins between 0 and 2 MeV were used. **Figure 4.1.2** displays the relative intensities of prompt and delayed gamma rays published by Skarsvåg and by Hootman and Stoddard.

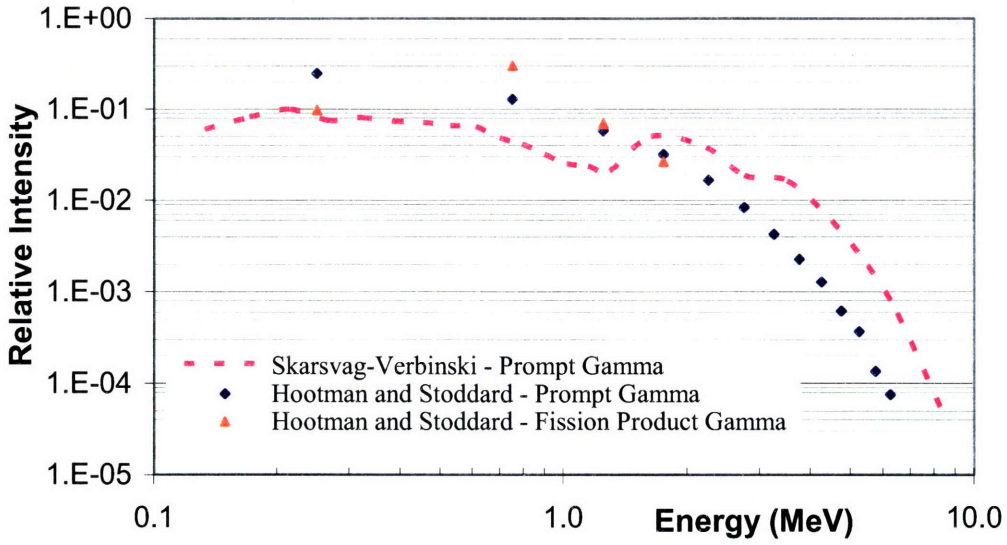

Figure 4.1.2: Prompt and delayed photon emission spectrum from spontaneous fission of ^{252}Cf and decay of fission daughter products, respectively. The prompt gamma ray spectrum measured by Skarsvåg and modified using data by Verbinski *et al.* was used in this study.

Although the prompt photon spectrum of Skarsvåg underestimates the total number of low-energy photons (*e.g.*, 0.25 and 0.75 MeV) presented by Hootman and Stoddard, similar trends are exhibited between the two datasets. Since modern measurements or calculations of the delayed photon spectrum are lacking, the prompt photon emission data of Skarsvåg was employed with the total photon emission rate of 1.3 x 10^{10} s^{-1} mg^{-1}.

4.1.3.2 Radiation transport simulations

4.1.3.2.1 Monte Carlo tally types and simulation defaults

Radiation transport calculations were conducted using version 5 of the Monte Carlo N-Particle Transport Code System (MCNP5), which employs the DLC-220 cross-section library published in 2004.[67] Initial calculations were performed on a 1.4 GHz computer running the Windows 2000 (Microsoft Inc.; Redmond, WA) system, and final calculations were undertaken at Oak Ridge National Laboratory's C-Pile.[100,101] For each shield thickness, two separate calculations were performed. One simulated the penetration of ^{252}Cf neutrons through the shield using MODE N P to include the generation and transport of secondary photons. The second simulated the attenuation of ^{252}Cf photons through the shield in MODE P.

For neutron transport, the F4 tally estimator was used in conjunction with a tally modifier (*i.e.*, DE and DF) to determine the equivalent dose to ICRU four-component tissue in a vacuum.[70] The neutron tally modifier included two components: (1) kerma coefficients to convert neutron fluence (cm^{-2}) to absorbed dose [Gy] and (2) an energy-specific radiation weighting factor (w_R) to convert absorbed dose to equivalent dose. The ICRU published neutron kerma conversion coefficients in Report 63 for twelve elements.[91] To determine the kerma coefficient for a compound containing any of these elements, the individual coefficients are weighted by their respective mass-percent and summed. Energy-specific neutron w_R factors were taken from Publication 60 of the International Commission on Radiological Protection (ICRP).[50] In addition, thermal neutron scattering functions, *i.e.*, $S(\alpha,\beta)$, was utilized when appropriate to provide accurate modeling of neutron thermalization and incoherent scattering.

For primary photon transport, the *F4 tally estimator was used in conjunction with a tally modifier (*i.e.*, DE and DF) to determine the absorbed dose to ICRU four-component tissue in a vacuum. Energy absorption coefficients published by Hubbell and Seltzer[71] transformed energy-flux per neutron [MeV cm^{-2}] to absorbed dose [J kg^{-1}]. Additional unit conversion was included to determine the absorbed dose [Gy], which is equal to the equivalent dose as w_R is unity for photons. Due to the small population of high-energy photons, photonuclear physics (PHYS:P) was not incorporated.

A sufficient number of photon histories were used to ensure statistical uncertainties remained less than 2%. For most cases, preliminary calculations using 10^6 histories were sufficient to meet this requirement. Final calculations performed at C-Pile computed between $1x10^7$ and $2x10^9$ starting particles, and variance reduction techniques were not utilized.

Three shielding materials, polyethylene, RICORAD™, and Pb, were evaluated towards the construction of a HDR ^{252}Cf storage safe. Elemental compositions of the shielding materials used in this study are given in **Table 4.1.1**. The composition of ICRU four-component tissue is included, which was used to determine the neutron kerma coefficients and photon energy absorption coefficients.

Table 4.1.1: Percent mass composition of materials included in shielding analyses.

		Material		
Element	ICRU Tissue	polyethylene	lead	RICORAD™
H	0.101174	0.143716	-	0.1206
B	-	-	-	0.0200
C	0.111000	0.856284	-	0.8493
N	0.026000	-	-	-
O	0.761826	-	-	0.0046
Al	-	-	-	0.0015
Si	-	-	-	0.0020
Fe	-	-	-	0.0020
Pb	-	-	1.000	-
ρ [g cm^{-3}]	1.00	0.93	11.35	0.945
S(α,β)	-	POLY.60t	-	POLY.60t

For elements that did not have DLC-220 neutron cross-sections for their natural isotopic abundances, relative isotopic abundances by atom were assigned considering the available neutron libraries. Hydrogen was modeled using 99.985 % ^{1}H and 0.015% ^{2}H; boron was modeled using 19.9% ^{10}B and 20.1% ^{11}B; oxygen was modeled as 100% ^{16}O; and, Pb was modeled as 24.4% ^{206}Pb, 22.4% ^{207}Pb, and 53.2% ^{208}Pb.

4.1.3.2.2 Simulation geometry

A spherical geometry was used that was similar in design and composition to that employed by both Hootman and Stoddard and by da Silva and Crispim. An

unencapsulated point source was positioned at the center of a solid aluminum sphere with radius 0.6204 cm and a volume of 1 cm^3. While da Silva and Crispim employed a 0.02 cm-thick aluminum shell with inner radius 0.62 cm, a solid sphere more accurately represented the geometry and density of a physical source without requiring a vacuum, which would remove the effects of self-shielding. Shells of varying thickness were added outside of the source for the three shielding materials evaluated, as shown in **Figure 4.1.3**. F4 and *F4 tallies for neutrons and photons were determined in a vacuum for a shell of thickness 0.1 μm surrounding the outer boundary of the shield.

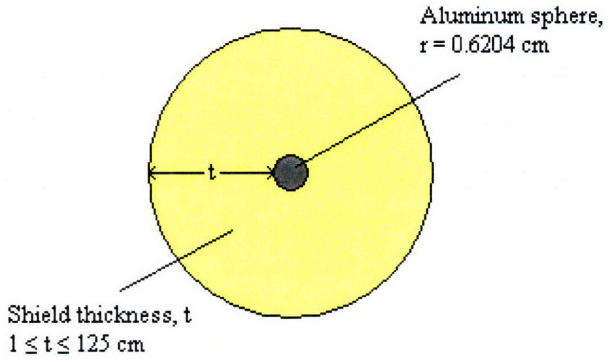

Figure 4.1.3: Schematic of the spherical shielding geometry employed in these Monte Carlo calculations. A shield of varying thickness, t, was placed around an isotropic source at the center of an aluminum sphere.

A two-component Pb:RICORAD™ shield was evaluated by fixing the total shield thickness and varying the relative amount of the two materials for a 1 mg ^{252}Cf source. To minimize total weight, Pb was employed as the internal layer and RICORAD™ surrounded it externally. Pb thickness of 2, 4, 6, 8, and 10 cm were calculated for a shield of total thickness 50 cm. For a larger shield, 100 cm thick, Pb thickness of 5, 10, 15, and 20 cm were calculated.

4.1.4 RESULTS AND DISCUSSION

4.1.4.1 Single component shield analysis

Figures 4.1.4, **4.1.5**, and **4.1.6** show the product of the equivalent dose rate and the distance squared [mSv h^{-1} x d^2] from 1 mg of ^{252}Cf for neutrons, secondary photons,

and primary photons, respectively. The square of the distance was incorporated to remove the influence of divergence. The total equivalent dose for each shielding material is shown in **Figure 4.1.7**.

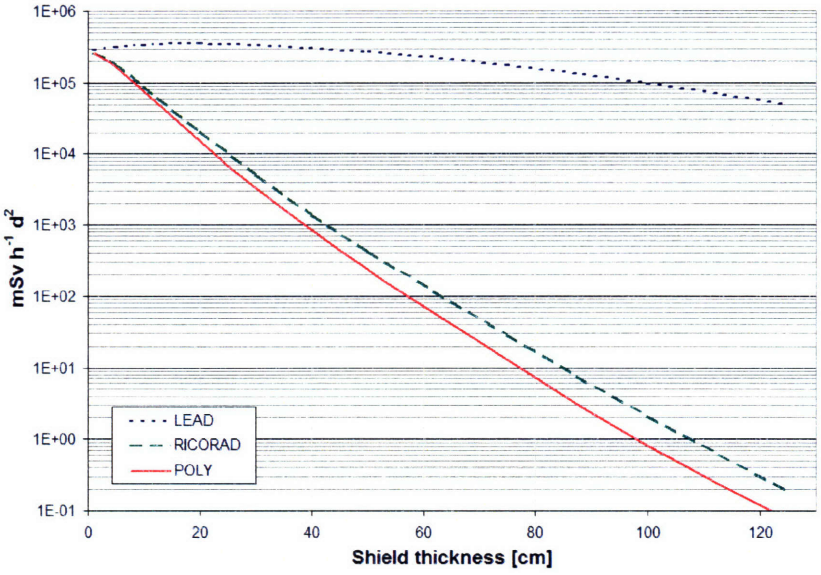

Figure 4.1.4: Equivalent dose to ICRU four-component tissue from ^{252}Cf neutrons for the three shielding materials.

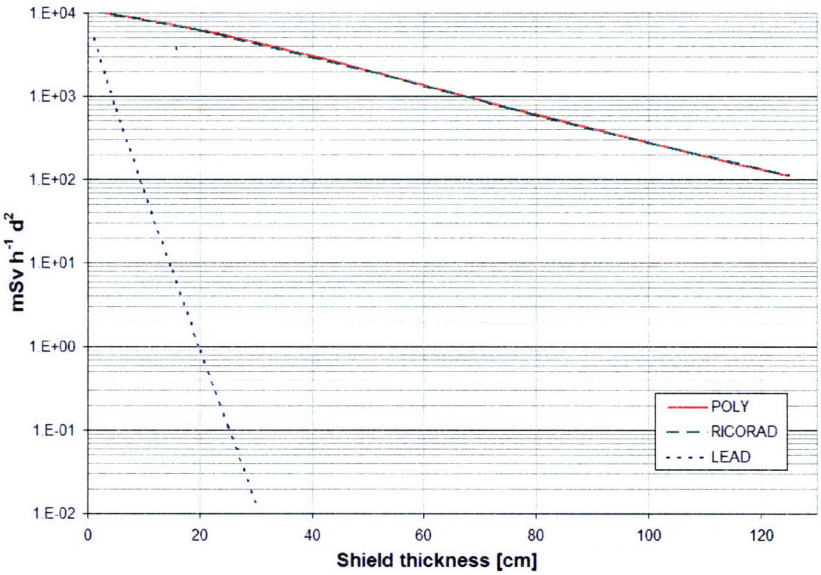

Figure 4.1.5: Equivalent dose to ICRU four-component tissue from primary gamma rays for the three shielding materials.

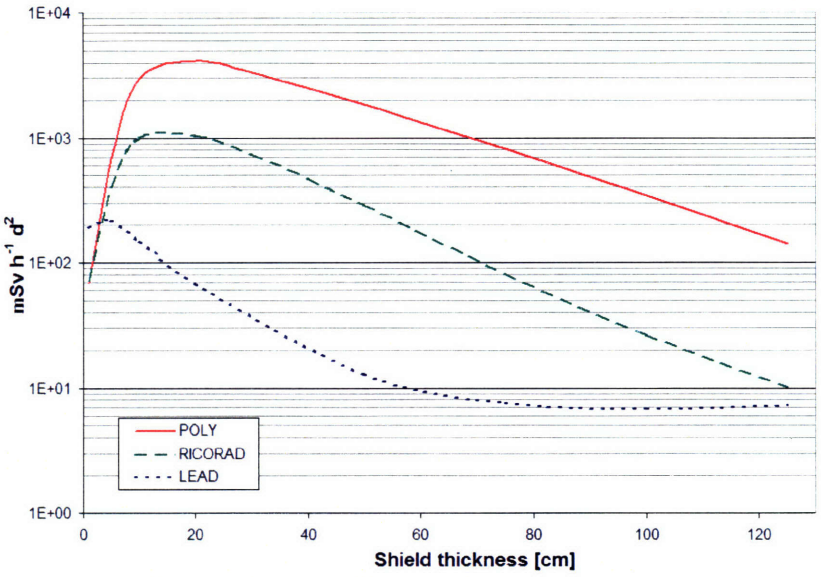

Figure 4.1.6: Equivalent dose to ICRU four-component tissue from secondary gamma rays (neutron capture photons) for the three shielding materials.

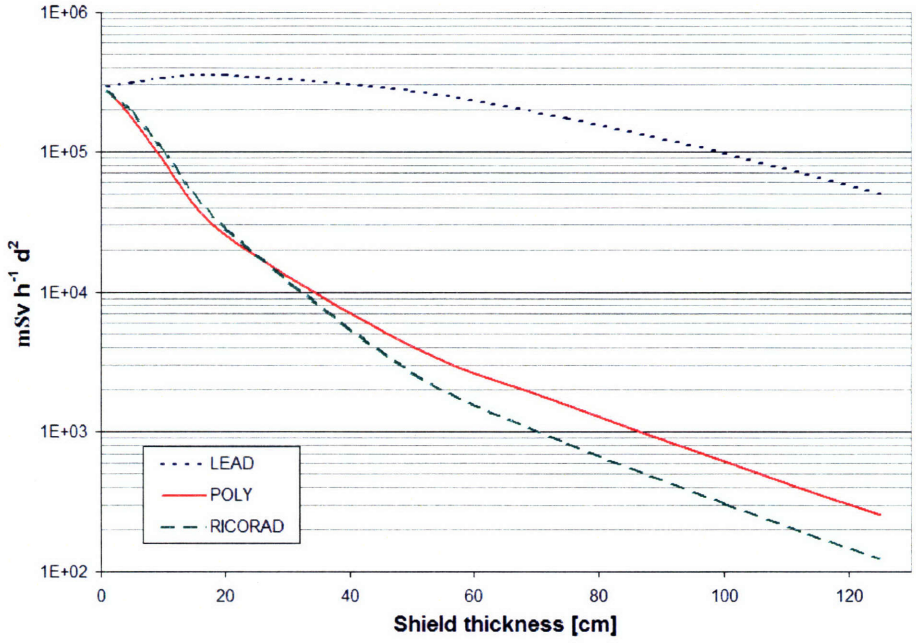

Figure 4.1.7: Total equivalent dose to ICRU four-component tissue after attenuation through Pb, polyethylene, and RICORAD™.

Pb provides significant attenuation of the primary photons, but does not provide neutron protection. RICORAD™ and polyethylene provide similar primary photon and neutron attenuation. Fewer secondary photons escape from the RICORAD™ shield

because thermal neutrons are preferentially captured by boron, which minimizes capture gamma ray emission after capture by hydrogen.

4.1.4.2 Multiple component shield analysis

Table 4.1.2 displays the neutron and photon equivalent doses at the exit of the 50 cm-thick Pb:RICORAD™ shield.

Table 4.1.2: Comparison of neutron and photon equivalent dose rate ($\dot{H}$) at the exit of a 50 cm spherical Pb:RICORAD™ safe for a 1 mg ^{252}Cf source.

	Equivalent dose rate [μSv h^{-1}]			
Pb thickness [cm]	$\dot{H}_n$	$\dot{H}_{n,\gamma}$	$\dot{H}_\gamma$	$\dot{H}_{total}$
2	173.0	121.6	270.2	564.8
4	181.8	121.1	112.9	415.7
6	185.8	119.6	48.5	353.9
8	190.4	118.7	21.0	330.1
10	199.6	119.4	9.2	328.1

ICRP 60 recommends limiting the annual effective dose to a radiation worker below 50 mSv. Therefore, a Pb:RICORAD™ shield designed to maintain a radius of 50 cm would allow only 89 to 149 hours of work per year adjacent to the safe for the 2 and 10 cm of Pb designs, respectively.

For a Pb:RICORAD™ shield designed to maintain a radius of 100 cm, the annual workload would increase to over 7,800 hours. Equivalent dose values for a multi-component safe with a total shield thickness of 100 cm diameter are shown in **Table 4.1.3**. Assuming 2,000 work-hours per year, a radiation worker positioned at the exterior of the safe would receive 12.8 mSv per annum, one-quarter of the ICRP 60 allowance. Thus, a safe employing one of the designs in **Table 4.1.3** would provide adequate protection for a source containing almost 4 mg of ^{252}Cf.

Table 4.1.3: Comparison of neutron and photon equivalent dose rate ($\dot{H}$) at the exit of a 100 cm spherical Pb:RICORAD™ safe.

	Equivalent dose rate [μSv h^{-1}]			
Pb thickness [cm]	$\dot{H}_n$	$\dot{H}_{n,\gamma}$	$\dot{H}_\gamma$	$\dot{H}_{total}$
5	0.25	2.86	3.35	6.46
10	0.20	2.53	0.43	3.16
15	0.23	2.42	0.06	2.71
20	0.20	2.53	0.01	2.74

Although storage safes are typically placed in restricted areas and require minimal maintenance, a robust shield would be desirable to assure minimal radiation exposure to personnel and the public. One disadvantage with the 100 cm safe design is that it would occupy a volume of 4.2 m^3. The total shield weight would be 4,040, 4,085, 4,199, or 4,415 kg for safe models with 5, 10, 15, or 20 cm of Pb, respectively. Potential installation sites would require thorough engineering analyses prior to construction.

4.1.4.3 Comparison to other studies

Hootman and Stoddard modeled the shielding properties of 32 different materials in their 1971 report, but only one of those materials is in common with those studied here - polyethylene. Using a spherical shield and a point source, Hootman and Stoddard calculated the equivalent dose to tissue. **Figure 4.1.8** displays the ratio of the results presented here to those of Hootman and Stoddard.

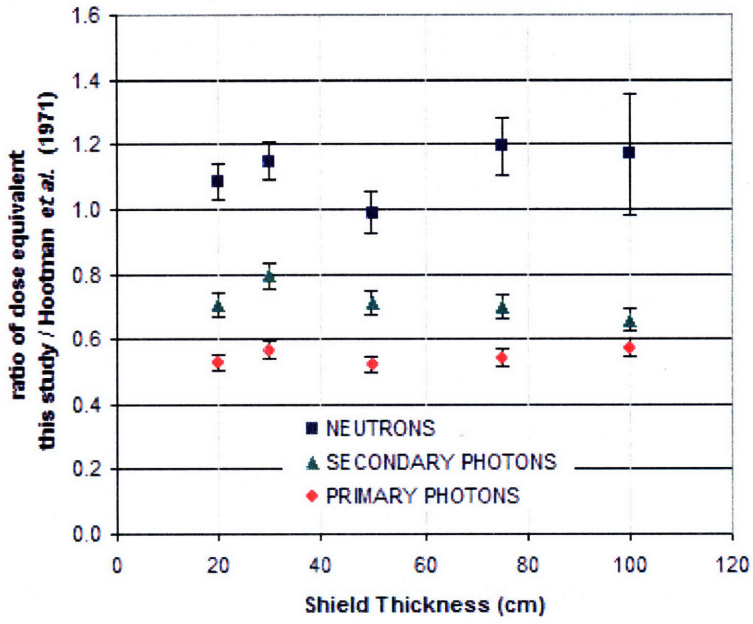

Figure 4.1.8: Ratio of Monte Carlo shielding calculations for polyethylene from this study to Hootman and Stoddard (1971).

Our neutron equivalent dose data in polyethylene was within 20% agreement of those presented by Hootman and Stoddard. The secondary photons and primary photons exhibit a near constant ratio, although they differ from the current Monte Carlo results by approximately 71% and 55%, respectively.

The models employed by da Silva and Crispim were designed for the construction of a neutron irradiator and included a 30 cm sphere of high-density polyethylene around the source. Three shielding materials were studied, but none were similar to those investigated here. In addition, da Silva and Crispim included a thin (0.1 cm) shell of cadmium at the shield outer surface to absorb thermal neutrons. Because of these differences, it is difficult to directly compare the results obtained herein to those obtained by da Silva and Crispim. However, direct comparisons can be made at the exterior of a 30 cm radius sphere of polyethylene that is included to moderate the neutron spectrum. **Table 4.1.4** shows this comparison.

Table 4.1.4: Comparison of equivalent doses ($\dot{H}$) at the exterior of a sphere of polyethylene containing 1 mg of ^{252}Cf.

	Equivalent dose rate [$\mu Sv\ h^{-1}$]		
Investigator	$\dot{H}_n$	$\dot{H}_{n,\gamma}$	$\dot{H}_\gamma$
da Silva and Crispim	2790	3230	5950
This Study	3510	3550	4940
Ratio	1.26	1.10	0.83

As shown in **Figure 4.1.8** and **Table 4.1.4**, neutron equivalent dose values in this study were typically higher than those reported by Hootman and Stoddard or by da Silva and Crispim. While this difference is partially due to employing different neutron spectra, differences in dosimetric conversion factors likely caused the discrepancies, *e.g.*, differences between the radiation weighting factors and neutron kerma coefficients. For photons, the energy spectra of Hootman and Stoddard included a larger component of low-energy photons that resulted in increased equivalent dose at the shield outer surface. In addition, the results of this study included the most up-to-date photon cross-section libraries. The results of Hootman and Stoddard and of da Silva and Crispim are subject to photon cross-sections that have been shown to result in differences in comparison to the DLC-220 library for low-energy photons ($E_\gamma \leq 100$ keV).[102,103] Additional research is required to determine the magnitude of the effect of the different neutron and photon spectra, as well as, the impact of using older (*e.g.*, MCLIB02) photon cross-sections.

4.1.5 Conclusions

Monte Carlo methods have been used to determine the shielding characteristics of three materials: polyethylene, RICORAD™, and Pb. Each has desirable shielding characteristics for either neutrons or photons. A storage safe with spherical geometry which combines Pb and RICORAD™ has been evaluated. Using a total shield thickness of 50 cm, a 1 mg ^{252}Cf source can be safely stored according to ICRP 60 standards, allowing over 100 hours of work directly adjacent to the shield. Fabrication of this or a similar design is needed for confirmation with experimental measurements to compare with calculated exposure rates preceding installation of the storage safe and implementation of HDR ^{252}Cf brachytherapy treatments.

4.1.6 ADDENDUM

4.1.6.1 Materials and methods

Additional single-component shielding materials were modeled following the methodology described in **section 4.1.3**. Liquid water, concrete, and barite concrete were simulated using the weight percents,[71] material densities,[71] and MCNP5 cross-section libraries in **Table 4.1.5**. Liquid water is frequently used to moderate neutrons. Concrete and barite concrete are similar to low-density and high-density concrete, which are used to construct shielding for radiation therapy centers.

Table 4.1.5: Percent composition by mass and density of liquid water, concrete, and barite concrete. The MCNP5 neutron and photon cross-section libraries used in calculations are also shown.

	cross-section libraries	Mass percent of material [%]		
nuclide	n / p	Water	Concrete	barite concrete
^{1}H	62c / 04p	11.19	2.21	0.3585
^{12}C	66c / 04p		0.2484	
^{16}O	62c / 04p	88.81	57.493	31.1622
^{23}Na	62c / 04p		1.5208	
Mg	62c / 04p		0.1266	0.1195
^{27}Al	62c / 04p		1.9953	0.4183
S	62c / 04p			10.7858
Si	60c / 04p		30.4627	
K	62c / 04p		1.0045	
Ca	62c / 04p		4.2951	5.0194
Fe	55c / 04p		0.6435	4.7505
^{138}Ba	66c / 04p			46.34
	ρ [g cm^{-3}]:	0.998	2.3	3.35

For these three materials, 2 x 10^7 starting particles were sufficient to obtain statistical uncertainties below 2%.

4.1.6.2 Results and discussion

The distance-corrected equivalent dose rates [mSv h^{-1} x d^2] from a 1 mg ^{252}Cf source are shown for neutrons, secondary photons, primary photons, and total radiation emissions in **Figures 4.1.9, 4.1.10, 4.1.11**, and **4.1.12**, respectively.

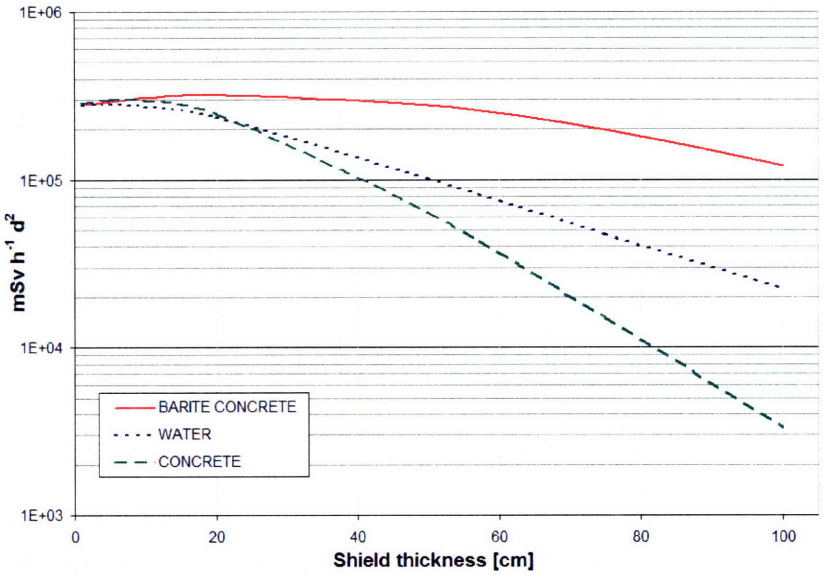

Figure 4.1.9: Distance-corrected equivalent dose rate to ICRU four-component tissue from ^{252}Cf neutrons for water, concrete, and barite concrete.

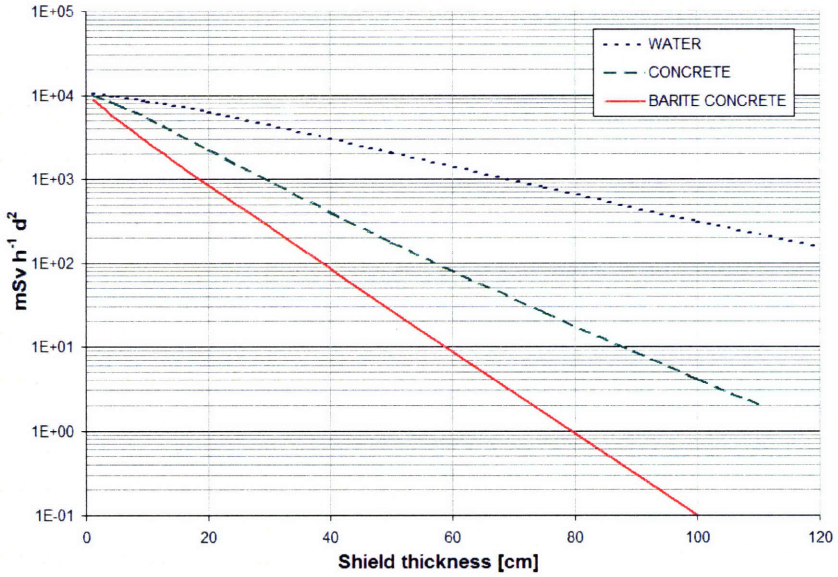

Figure 4.1.10: Distance-corrected equivalent dose rate to ICRU four-component tissue from primary ^{252}Cf gamma rays for water, concrete, and barite concrete.

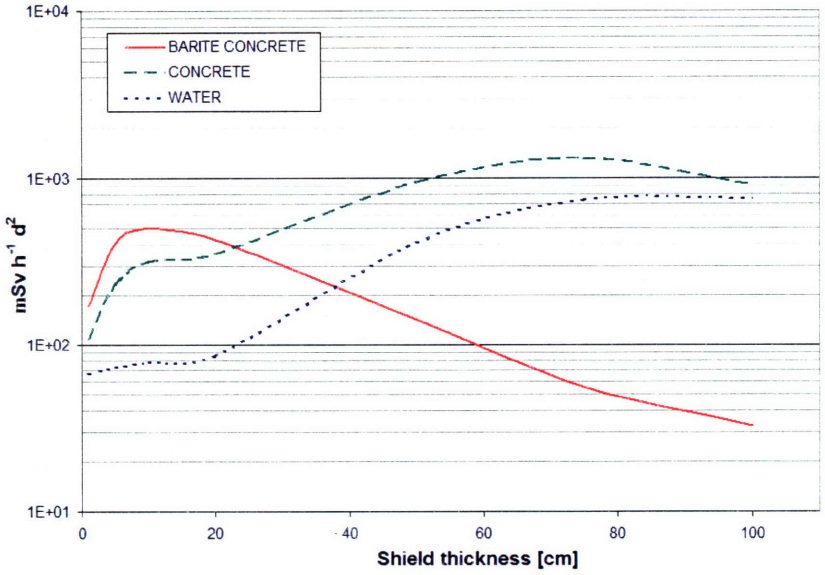

Figure 4.1.11: Distance-corrected equivalent dose rate to ICRU four-component tissue from secondary gamma rays (neutron capture photons) for water, concrete, and barite concrete.

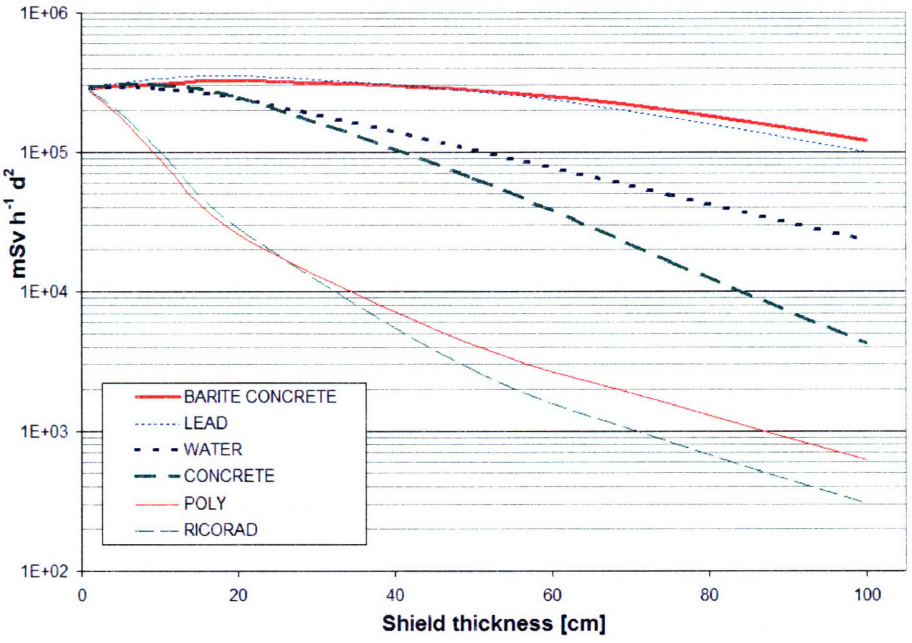

Figure 4.1.12: Total distance-corrected equivalent dose rate to ICRU four-component tissue after attenuation through water, concrete, and barite concrete. For comparison lead polyethylene, and RICORAD™ are included.

4.2 Shielding evaluation of a medical linear accelerator vault in preparation for installing a high-dose rate ^{252}Cf remote afterloader[†]

4.2.1 ABSTRACT

In support of the effort to begin high-dose rate californium-252 (^{252}Cf) brachytherapy treatments at Tufts-New England Medical Center, the shielding capabilities of a clinical accelerator vault against the neutron and photon emissions from a 1.124 mg ^{252}Cf source were examined. Outside of the clinical accelerator vault, the fast neutron dose equivalent rate was below the lower limit of detection of a CR-39 track-etch detector and below 0.14 ± 0.02 μSv h^{-1} with a proportional counter, which is consistent, within the uncertainties, with natural background. The photon dose equivalent rate was also measured to be below background levels (0.1 μSv h^{-1}) using an ionization chamber and an optically stimulated luminescence dosimeter. A Monte Carlo simulation of neutron transport through the accelerator vault was performed to validate measured values and determine the thermal- to low-energy neutron component. Monte Carlo results showed that the dose equivalent rate from fast neutrons was reduced by a factor of 10^5 after attenuation through the vault wall, and the thermal-energy neutron dose equivalent rate would be an additional factor of 10^3 below that of the fast neutrons. Based on these findings, the shielding installed in this facility is sufficient for use of at least 5 mg of ^{252}Cf.

4.2.2 INTRODUCTION

^{252}Cf is a man-made transuranic, which disintegrates via either alpha emission (96.908%) or spontaneous fission (3.092%), with an associated neutron emission rate of 2.314×10^9 s^{-1} mg^{-1}.[45] In addition, the long half-life of ^{252}Cf (2.645 y) compared to ^{192}Ir (73.8 d),[33] which is currently used in commercial high-dose rate (HDR) brachytherapy systems, is desirable because it allows for relatively infrequent source exchanges and related cost savings. Rivard et al. have shown that costs for HDR ^{252}Cf brachytherapy do not exceed 30% more than costs for standard-of-care HDR ^{192}Ir brachytherapy.[104] ^{252}Cf

---

[†] Reproduced from: C. S. Melhus, M. J. Rivard, J. KurKomelis, C. B. Liddle, and F. X. Massé, "Shielding evaluation of a medical linear accelerator vault in preparation for installing a high dose rate ^{252}Cf remote afterloader," Rad. Prot. Dos. **113**, 428-437 (2005).

neutrons are similar in energy to a reactor fission spectrum (mean 2.1 MeV) and exhibit desirable radiobiological qualities, e.g., reduced oxygen effect, decreased cell-cycle dependence, and increased relative biological effectiveness (RBE). As a result, ^{252}Cf treatment has demonstrated efficacy for tumors that have not responded to traditional, photon-based therapies.[36]

Several thousand patients have been treated with ^{252}Cf brachytherapy at various centers worldwide for a diverse assortment of lesions from head-to-toe. Clinical observations from this patient population included an RBE of 6 for low- and-medium dose rate brachytherapy, an RBE of 3 for HDR brachytherapy, acute tissue effects comparable to photon brachytherapy, dose rate independence, local tumor control, and rapid tumor regression. Cervical cancers, in particular, exhibited positive results for advanced, late-stage (III-IV) bulky tumors, including a 54% 5-year survival for early (i.e., before photon therapy) ^{252}Cf implants compared to 12% 5-year survival with conventional therapy for stage IIIB tumors.[105] Similarly, Tačev et al. noted an 18.9% increase in 5-year survival for stage IIB and IIIB cervical cancers compared to conventional photon therapy due to a significant decrease in local relapse.[106] Similar results were obtained after 12-year followup.[37] Positive local control was observed for several diseases and sites, including traditionally radioresistant melanomas that achieved complete local control with external ^{252}Cf plaque irradiation.[107] ^{252}Cf brachytherapy in China began in 1999 using a remote afterloading device called the *Linden Neutron Knife*, and thirty similar ^{252}Cf treatment centers are expected to be in operation by 2008 to provide one center per 40 million people.[108] Similar acceptance in the United States may be expected after the development of a suitable HDR ^{252}Cf source, remote afterloader, and associated infrastructure to complement HDR ^{192}Ir brachytherapy practice.

Currently, no institution in the Western Hemisphere utilizes ^{252}Cf clinically. However, Tufts-New England Medical Center (Tufts-NEMC) is actively pursuing implementation of ^{252}Cf brachytherapy.[93,101,109,110] Simultaneously, the Radiochemical Engineering Development Center (REDC) at Oak Ridge National Laboratory (ORNL), currently the sole producer of californium isotopes on Earth, is striving to produce a HDR ^{252}Cf brachytherapy source (> 1.0 mg) that would be compatible with the HDR ^{192}Ir brachytherapy remote afterloading environment. In conjunction with the development of

a clinical HDR ^{252}Cf brachytherapy system, it is necessary to provide adequate treatment room shielding to minimize incidental radiation exposure to the public and occupational radiation exposure to physicians, physicists, and allied health personnel involved with irradiating cancer patients. The National Council on Radiation Protection and Measurements (NCRP) has published shielding recommendations in Report No. 49,[111] described neutron production from medical electron accelerators in Report No. 79,[112] and recently published Report No. 144 to update these and other reports that thoroughly evaluates the radiation protection characteristics of neutrons generated in particle accelerator facilities.[113] Nevertheless, there is no radiological protection guidance for the medical use of neutron-emitting radionuclides.

As with any new radiation-emitting medical device, shielding requirements should be published preceding implementation of regulatory standards. This has been demonstrated by Robinson et al. for tomotherapy,[114] Mutic et al. for intensity-modulated radiation therapy,[115] and Methé for positron emission tomography.[116] Consequently, the shielding characteristics of a clinical linear accelerator vault for the mixed-field radiation emitted by ^{252}Cf were investigated at Tufts-NEMC.

4.2.3 MATERIALS AND METHODS

4.2.3.1 Vault and source description

Originally constructed in 1968, the linear accelerator vault, hereafter the "vault," houses a medical accelerator that can generate upto 25 MV electron and photon beams. A schematic of the facility is shown in **Figure 4.2.1**. The walls of the vault are composed of high-density concrete at 4.00 g cm^{-3} (250 lbs ft^{-3}) between 50.8 and 133.5 cm thick, although, one wall that is only 38.1 cm thick abuts the original building foundation-providing an additional 41.3 cm of standard concrete at 2.35 g cm^{-3} (147 lbs ft^{-3}). The ceiling thickness is 27.5 cm of high-density concrete and is 4.5 m from the floor. Shielding has been added on the walls and ceiling about the isocenter of the clinical accelerator to attenuate primary radiation, including at least 2.5 cm of 5% borated polyethelene and a minimum of 15.2 cm of lead. Along the ceiling, a 1.3 cm thick steel plate supports this shield. Situated outside the vault are a technologist workstation, patient waiting room, employee workroom, storage closets, corridors, and entrance maze

that precludes primary radiation from streaming into uncontrolled areas. Below the vault is a mechanical crawlspace, and above the vault are hallways, office space, and a restricted-access mechanical space.

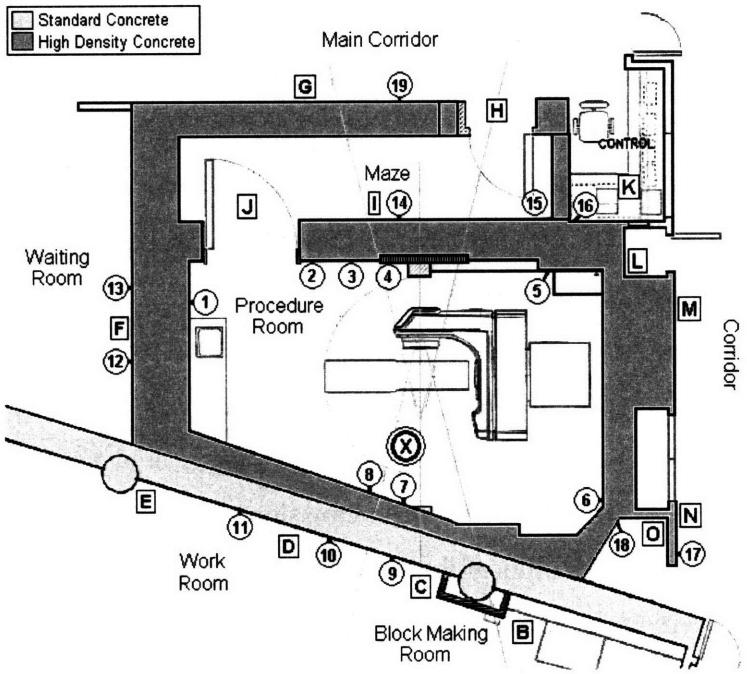

Figure 4.2.1: Floorplan of the clinical linear accelerator vault. Boxed letters correspond to positions where the dose was measured using portable radiation monitors, and circled numbers delineate where solid state dual-detector (Luxel® and Neutrak®) badge-type dosimeters were placed. The ⊗ symbol near position 7 indicates the cask and source position during ^{252}Cf source removal. Position A was located on the floor of the room directly above the source.

An industrial HDR ^{252}Cf source, serial No. SR-CF-3026, was manufactured at Savannah River Laboratory on 1 December 1983. This source was selected for evaluating the utility of the vault as its source strength was similar to that planned for a medical HDR ^{252}Cf brachytherapy source. On 28 April 2004, the HDR ^{252}Cf source contained 1.124 mg of ^{252}Cf (22.3 GBq) in the form of Cf_2O_3.[117] Nearly all of the neutrons were emitted by ^{252}Cf, with 3.3% from spontaneous fission by the other radionuclides. Measuring 53.4 mm in length and 9.4 mm in diameter, the special form material was doubly-encapsulated using TIG welds within a Pt-Rh (90-10 wt %) alloy inner capsule and 304L stainless steel outer capsule. An Atkinson shipping cask (serial No. 241; the company is now defunct) of approximately 1,670 kg was used to transport

and store the HDR ^{252}Cf source when not in use. Including the lifting tabs and I-beam base, the cylindrical cask was 128 cm in height, 127 cm in diameter, and largely composed of water extended polyester. At ORNL using robotic manipulator arms, a length of string was attached to the HDR ^{252}Cf source and taped to the bottom of the cask shield plug (53.3 cm long; 10.2 cm diameter), allowing removal of the source from a safe distance.

The cask was positioned in the vault to place the source at a distance of 1.3 m from the linear accelerator isocenter and 1.1 m from the nearest wall. Then, a tripod suspending a pulley was secured atop the cask. Surgical suture silk was tied to the string attached to the HDR ^{252}Cf source and threaded through the pulley. In this way, the source could be lifted from the cask from outside of the vault and monitored with closed-circuit video cameras.

Once the cask and tripod assembly were secured in place, the source was lifted to a height of 176 cm from the floor (57 cm from the cask top surface), as shown in **Figure 4.2.2**. The source was lifted outside the cask in the vault for a total of 3.4 hours. Radiation survey measurements were obtained with the maze doors open and closed to the vault at the measurement positions within the entrance maze. The cask and source was on-site at Tufts-NEMC for about 24 hours.

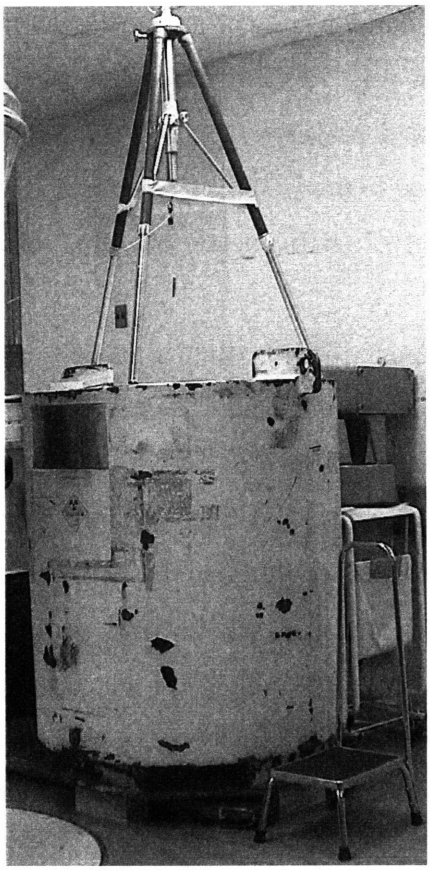

Figure 4.2.2: The industrial HDR ^{252}Cf source is suspended in-air above the shipping cask during the shielding assessment. Note the surgical suture silk that extended outside of the vault to permit manipulation of the source from within the vault maze.

4.2.3.2 Radiation detection instruments

As recommended in NCRP Report No. 79, multiple detectors were used to measure the fast neutron and photon dose rates. For each radiation type, both gas-filled portable instruments and solid-state dosimeters were employed. The solid-state badge-type personnel dosimeters were in place for the duration of the 3.4 hour exposure, whereas the portable instruments either took an instantaneous reading or integrated for between 0.1 and 1 hour.

Neutron dose rates were measured with four calibrated Health Physics Instruments (HPI; Goleta, CA) model REM 500 survey meters. The REM 500 contains a spherical proportional counter with A150 tissue-equivalent plastic chamber walls (5.7 cm inner diameter) and propane filling gas.[118] A 256-channel multi-channel analyzer allows

for neutron energy-specific quality factors to determine the channel-integrated dose equivalent in Sv. Operating in time-integrate mode, the REM 500 can measure between 0.01 mSv and 9.99 Sv and has an approximately dose equivalent response to neutrons between 70 keV and 20 MeV. The contributions of thermal- to low-energy neutrons, for which the REM 500 does not have an ambient dose equivalent response, were estimated using Monte Carlo methods. The photon radiation response is reported to be less than one percent in a 0.01 Gy h^{-1} field.

Photon dose equivalent was measured with calibrated Keithley (Keithley Instruments, Inc., Cleveland OH) 36150 and 36100 survey meters to integrate or measure the dose equivalent rate, respectively. Both models are air-equivalent ionization chambers, with a volume of 250 cm^3, vented to the atmosphere.[119] The resolution is 1 μSv h^{-1} for exposure measurements for low-levels of radiation. Using the front window and build-up cap, the energy response is ± 10% for photons between 32 keV and 2 MeV.

Duel element, i.e., neutron- and photon-sensitive, dosimeters supplied by Landauer Inc. (Glenwood, IL) were situated in and around the perimeter of the vault at a height of 1.52 m for each numbered position labeled on **Figure 4.2.1**. Luxel® optically stimulated luminescence (OSL) detectors were utilized to monitor the photon dose, and the incorporated Neutrak® 144 CR-39 track-etch detector was employed to quantify the fast-neutron component. The Luxel® dosimeter detects photon energies from 5 keV to over 45 MeV, with a range of 10 μSv to 10 Sv; the Neutrak® dosimeter is sensitive to neutron energies from 40 keV to over 35 MeV and responds between 200 μSv and 0.25 Sv.[120]

While a phantom may be used in conjunction with a passive dosimeter to measure personal dose equivalent, i.e., Hp(10), there were not enough phantoms available for the full complement of twenty Neutrak® dosimeters. Thus, each dosimeter badge was affixed to the wall and an approximate determination of Hp(10), which excludes the effect of backscatter, is presented here.

4.2.3.3 Monte Carlo calculations

Because the REM 500 and Neutrak® 144 dosimeters were insensitive to thermal- to low-energy neutrons, Monte Carlo calculations were performed to estimate the

contribution of neutrons below 1 keV to the dose equivalent rate outside of the vault. A cylindrical model of the vault wall was constructed to simulate neutron transport between positions 7 and 9 on **Figure 4.2.1**, as shown in **Figure 4.2.3**. This wall segment was selected for it's minimal thickness and proximity to the source. Neutrons emitted from a point source or along the long-axis of a 12.5 cm radius cylinder were transported through air, high-density concrete, and low-density concrete using material compositions published by NIST for dry air, barite concrete (with density 4.00 g cm^{-3}), and normal concrete (with density 2.35 g cm^{-3}), respectively.[71]

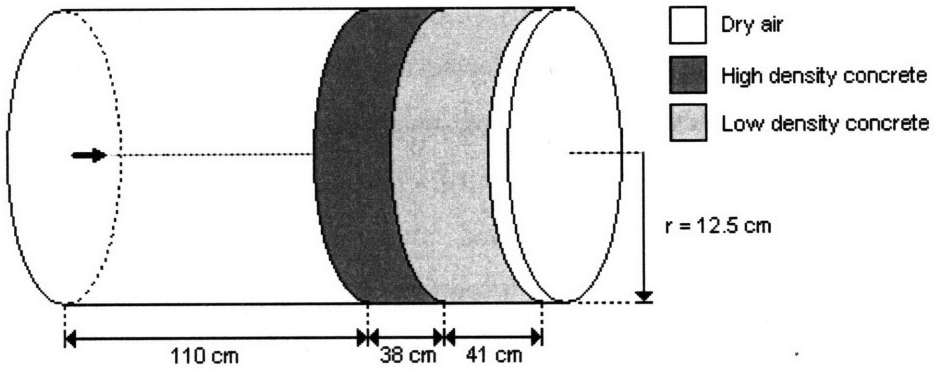

Figure 4.2.3: Schematic of the Monte Carlo geometry performed to simulate neutron transport through the vault wall between positions 7 and 9 on **Figure 4.2.1**. Neutrons were emitted along the central axis and scored in the volume air following the low-density concrete. Neutrons that scattered outside of the 12.5 cm radius cylinder were not scored.

The track length estimator of heating tally (F6) was employed in MODE N of the radiation transport code MCNP5 to determine the average energy deposited [MeV g^{-1}] per neutron at the entrance and exit of the vault wall.[67] A 10 cm radius cylindrical cell with 1 μm thickness of ICRU four component tissue[70] was placed at the entrance and exit of the vault wall, and tally results were tabulated over the innermost 5 cm of radial distance. Radiation weighting factors (w_R) from ICRP 60 were incorporated to estimate the dose equivalent [μSv] to ICRU four-component tissue per starting particle.[50]

Tally energy cards (En) divided the output into 26 neutron energy bins and were subsequently grouped into three regimes: below 10^{-6} MeV, between 10^{-6} and 10^{-3} MeV, and between 10^{-3} and 20 MeV. A total of $2x10^8$ and $1x10^9$ histories were computed for the collimated beam and point source geometries, respectively.

4.2.4 *RESULTS*

4.2.4.1 In preparation of the vault assessment

Unless otherwise noted, the uncertainty in the fast neutron dose equivalent measured with a REM 500 is a combination of statistical and systematic uncertainties, with systematic uncertainties including a 14% calibration uncertainty (upper bound) and timing error (< 0.1%).

Two calibrated REM 500 meters were placed at 1.00 m from 0.9 μg of ^{252}Cf for 35 minutes, and measured 27 ± 2 (± 1 s.d.) μSv h^{-1}. For comparison, an ORNL-provided rule-of-thumb yields a neutron dose rate of approximately 22.1 μSv h^{-1} μg^{-1} of ^{252}Cf at 1 m, showing agreement within 36% of the measured value. Differences between the measured and expected values may be attributed to neutron room scatter during the measurement. To evaluate the relative calibration and response of four REM 500 survey meters, the survey meters were placed alongside each other 2.00 m from a shielded ^{252}Cf source and allowed to integrate for 14.8 h. The average reading was 0.57 ± 0.04 (± 1 s.d.) μSv h^{-1}, showing good agreement between the four meters. Additionally, the photon response of the REM 500 neutron meter was examined using a ^{137}Cs calibration source. As expected, the meters responded by less than one percent in both 0.40 and 1.60 mSv h^{-1} fields.

Multiple background measurements with durations between six and fifteen hours were made using REM 500 meters. An average background rate of 0.14 ± 0.02 μSv h^{-1} was established with a correlated count rate of 3.2 ± 0.3 counts h^{-1}, implying that a wide range of neutron energies were present in the background measurements. At the 95% confidence limit, the lower limit of detection (LLD) was 5.2 counts per hour such that measurements below the LLD were presumed to be from background sources.[121]

4.2.4.2 Vault assessment using a HDR ^{252}Cf source

Results of neutron measurements from surveying the linear accelerator vault are shown in **Table 4.2.1** with photon measurements presented in **Table 4.2.2**. At position H with the vault doors opened, a significant number of neutrons were detected as a result of scattering and transport through the maze. Closing the shielded doors returned the area to

background levels. Neither neutron nor photon radiation fields were measured outside of the sealed vault.

Corresponding badge-type dosimeter readings for the Luxel® and Neutrak® dosimeters are shown in **Table 4.2.3**. These dosimeters were posted with double-sided tape before the cask was transported into the vault and remained in place for the duration of the 3.4-hour exposure. Only those badges posted within the vault produced measurable readings. The remaining badges yielded results below the minimum reporting limit, 0.2 mSv for neutrons and 0.1 mSv for photons. The minimum measurable quantity for an OSL dosimeter is 10 μSv (1 mrem); however, a facility-selected minimal reporting limit of 100 μSv (10 mrem) is employed. Landauer results included a calibration factor of 0.65.[†] For determining personnel dose equivalent, Landauer would use a quality factor (Q) of 10 for neutrons of unknown energy as stipulated by the U. S. Nuclear Regulatory Commission in the U. S. Code of Federal Regulations (Title 10, Part 20); however, the ICRP recommends a neutron energy dependent radiation-weighting (w_R) factor.[122,50] Rivard determined an energy-averaged radiation weighting factor based on a spontaneous fission neutron spectrum of 15.4.[123] Because the ratio of the Q and w_R is equivalent to the Landauer calibration factor, uncorrected values were employed in this study.

[†] Neutrak® 144 CR39 track etch detectors are calibrated with an Am:Be neutron source. The factor corrects for differences in the incident energy spectra for the two sources.[124]

Table 4.2.1: Result of neutron dose equivalent rate ($\mu Sv\ h^{-1}$) measurements around the vault during suspension of the source in air with the associated count rate. All measurements made with Health Physics Instruments model REM 500 detectors. For each measurement position, as designated on **Figure 4.2.1**, the dose equivalent rate (± 1 s.d.), count rate (± 1 s.d.), and total integration length or range of lengths are shown. Position A was measured on the floor of the room directly above the vault.

Position		$Hp(10)_n$ [$\mu Sv\ h^{-1}$]	Count Rate [$cts\ h^{-1}$]	Integration Time [h]
A-G, K-O		0.0 ± 0.3	< LLD	0.25 - 2.0
H	Door Open	8 ± 1	300 ± 30	0.33
	Door Closed	0.0 ± 0.2	< LLD	0.50
I	Door Open	60 ± 8	2,250 ± 80	0.33
	Door Closed	6.1 ± 0.9	280 ± 20	0.67
J	Door Open	2,200 ± 300	84,800 ± 400	0.43
	Door Closed	70 ± 10	3,080 ± 80	0.43

Table 4.2.2: Result of photon dose equivalent rate [$\mu Sv\ h^{-1}$] measurements around the vault during suspension of the source in air. All measurements made with Keithley model 36100 or 36150. The position corresponds to the boxed letters on **Figure 4.2.1** with the exception of position A, which was measured on the floor of the room directly above the vault.

Position		$Hp(10)_\gamma$ [$\mu Sv\ h^{-1}$]
A-G, K-O		< 1
H	Door Open	1
	Door Closed	< 1
I	Door Open	8
	Door Closed	< 1
J	Door Open	175
	Door Closed	1

Table 4.2.3: The neutron (n) and photon (γ) dose equivalent rates measured using Neutrak® and Luxel® Landauer dosimeters, respectively. The position corresponds to the circled numbers on Figure 1 with the exception of position 20, which was placed on the floor of the room directly above the vault. Based on the time the industrial HDR ^{252}Cf source was outside the cask, the total exposure for these 20 positions lasted 3.4 hours.

Position	$Hp(10)_{\gamma}$ [mSv h^{-1}]	$Hp(10)_{n}$ [mSv h^{-1}]	$Hp(10)_{TOTAL}$ [mSv h^{-1}]	Distance [m]
1	0.06	1.03	1.08	5.0
2	0.15	2.53	2.68	4.0
3	0.18	4.21	4.38	3.7
4	0.18	3.91	4.09	3.5
5	0.09	1.29	1.38	4.1
6	0.15	3.56	3.71	3.8
7	1.21	21.32	22.53	1.1
8	0.88	12.74	13.62	1.3
9 - 19	< 0.03	< 0.06	< 0.09	2.1 to 6.5
20	< 0.03	< 0.06	< 0.09	3.7

4.2.4.3 Monte Carlo calculations

Statistical uncertainties for the point source geometry at the interior of the vault wall were below 3%, 4%, and 0.2% for thermal-, low-, and high-energy neutrons, respectively. For the collimated beam of neutrons, uncertainties were below 0.3%, 0.2%, and 0.1% at the interior of the wall and below 6%, 14%, and 3% at the exterior for thermal-, low-, and high-energy neutrons, respectively. Uncertainties for the point source geometry were significantly higher because less than 1% of the starting particles interacted with the vault wall in the simulation. As such, the relative uncertainties in the tally results at position 9 in the point source geometry were prohibitively large.

The F6 tally for the point source geometry yielded $4.28 \pm 0.01 \times 10^{-12}$ mSv (± 1 s.d.) per neutron at the entrance of the vault wall. The corresponding dose equivalent rates for the HDR ^{252}Cf source studied were 40.1 ± 0.1 mSv h^{-1} (± 1 s.d.) at position 7. Compared to the Neutrak® dosimeter reading at position 7, the MCNP result is 88% higher. As the MCNP result was based on an ideal detector with a dose equivalent reading for all neutron energies and included a spectrally weighted w_R, these values show reasonable agreement.

Table 4.2.4 shows the F6 tally results from the collimated beam of neutrons before and after the vault wall. Neutrons between 1 keV and 20 MeV were reduced by almost 10^{-5} after transport through the wall, and indicate that the dose equivalent rate would have been approximately 0.2 μSv h^{-1} at position 9, which is significantly below the sensitivity of the Neutrak® dosimeter. Furthermore, dose equivalent rate for thermal neutron at position 9 would be approximately 10^3 times smaller than that for fast neutrons.

Table 4.2.4: MCNP5 calculated cell heating tally results [MeV g^{-1}] per source particle for ^{252}Cf neutrons in the source geometry shown in **Figure 4.2.3**. For comparison, results are presented at the entrance and exit of the vault wall model with a ratio illustrating the population change in each energy regime. Neutrons energies are characterized in three regimes: below 1 eV, between 1 eV and 1 keV, and between 1 keV and 20 MeV.

Maximum Neutron Energy [MeV]	Vault Wall Entrance [MeV g^{-1}]	Vault Wall Exit [MeV g^{-1}]	Ratio
1×10^{-6}	$2.58 \times 10^{-8} \pm 0.003$	$4.80 \times 10^{-11} \pm 0.06$	1.9×10^{-3}
1×10^{-3}	$3.01 \times 10^{-8} \pm 0.002$	$1.63 \times 10^{-12} \pm 0.14$	5.4×10^{-5}
2×10^{1}	$2.93 \times 10^{-3} \pm 0.0001$	$2.55 \times 10^{-8} \pm 0.03$	8.7×10^{-6}

4.2.5 DISCUSSION

4.2.5.1 Radiation Protection

The radiation dose limit to a member of the public is 1 mSv per annum and 0.02 mSv in any given hour in an unrestricted area.[125] To determine the corresponding annual allowable HDR ^{252}Cf brachytherapy workload, an estimate of the neutron and photon dose rates are needed. Based on the lower limit of detection in **Table 4.2.1** and **4.2.2**, a conservative estimate of the neutron and photon dose rates outside of the vault would be 0.2 μSv h^{-1} and 0.1 μSv h^{-1} from a 1.124 mg HDR ^{252}Cf source. These dose equivalent rates would permit 10,000 twenty-minute patient treatments per annum. While the use factor is unity for an isotropic source, an occupancy factor of one-fourth would be applied to the surrounding corridors and a factor of one-sixteenth to the patient waiting area, such that 40,000 treatments could be provided per year with the current HDR ^{252}Cf source. Assuming that the dose rate outside of the shield varies linearly with ^{252}Cf source

strength, which is a reasonable based upon the work of Hootman and Stoddard,[49] increasing the source strength to 5.0 mg of ^{252}Cf would decrease the allowed number of twenty-minute treatments to ~ 9,000. The maximum expected patient volume, 100 patients per year, could be easily accommodated by this limit.

Similarly, the hourly dose limit to a member of the public was not met with a 1.124 mg HDR ^{252}Cf source. A 5.0 mg HDR ^{252}Cf source would register an estimated maximum of 1.3 μSv over one hour outside the vault. While the maximum ^{252}Cf source strength that could be employed would be 75 mg before incorporating the occupancy factor, it may not be prudent to extrapolate these results by a factor of ~ 70 before performing additional measurements and Monte Carlo simulations.

In the development of a ^{252}Cf brachytherapy afterloading device at Masaryk Memorial Cancer Institute (MMCI; Czech Republic), Tačev et al. converted a vault designed for cobalt teletherapy into a facility suitable for low-dose rate treatments using between 0.05 and 0.20 mg ^{252}Cf sources.[47] The original barrier was composed of barite concrete (~ 3.35 g cm^{-3}) with thickness between 60 and 120 cm, and an additional 24 cm of *neutronstop* polyethylene bricks was installed on the walls and ceiling. Although Tačev et al. did not analyze the radiation shielding characteristics of this design, comparisons can be made to the Tufts-NEMC vault. The concrete thickness at the MMCI is similar to that at Tufts-NEMC; the Tufts-NEMC shield does not include any neutron-absorbing material, except along the axis of gantry rotation (see **section 4.2.3.1**); and the Tufts-NEMC source strength used in the present analysis was five times greater than that employed at MMCI. Considering these points, the inclusion of the *neutronstop* shielding material may have been an unnecessary expense, as the Tufts-NEMC vault demonstrated acceptable protection without a neutron-specific absorber. However, significant differences in the size of the room, the occupancy factors of the surrounding areas, and other nearby ionizing radiation emitting devices could necessitate inclusion of additional neutron shielding.

4.2.5.2 Neutron transport analysis

Neutron transport through a labyrinth of general shape was calculated using universal transport data in NCRP Report No. 144. These data are based on the combined

results of several neutron transport software codes. The fraction transmitted through the maze is presented as a function of the centerline length and cross-sectional area of each tunnel leg. Because the initial segment has direct exposure to the source, it is considered separately from each successive segment.

The NCRP 144 calculated fraction was compared to relative intensities between position J at the maze entrance and positions H and I in the maze with the vault doors open (**Table 4.2.1**). The neutron field at position I was reduced by a factor of 36 ± 7 compared to that recorded at position J. NCRP 144 predicted reduction by a factor of 22 using the vault maze dimensions with maximum and minimum extremes of 48 and 11, respectively, where the extrema represent individual calculations with the largest variation from the average. Similarly, the neutron intensity at position H was decreased by a factor of 275 ± 107 relative to position J, and NCRP 144 predicted 714-fold reduction with maximum and minimum of 3,300 and 170, respectively. Thus, the generalized curves for neutron scattering through a tunnel or labyrinth published in NCRP Report No. 144 were found to well-characterize spontaneous fission neutrons from a HDR ^{252}Cf source transported through the Tufts-NEMC vault maze.

4.2.5.3 Shielding analysis

Hootman calculated the attenuation of ^{252}Cf neutron and photon emissions through a spherical shield having varying thickness of polyethylene, water, concrete, and other materials,[48] and Hootman and Stoddard significantly improved the work by thoroughly describing their methodology and including over thirty different shield compositions. The neutron and photon dose rates per neutron-emission of ^{252}Cf were included, but the minimum shield thickness calculated was 10 cm and lead was excluded as a shield material. Comparison to Hootman and Stoddard's results can be made using measurements at positions 7 and 9 in **Figure 4.2.1**. The total neutron and photon dose equivalent (Hp(10)) at position 7 was 21.32 mSv and 1.21 mSv, respectively. Data from Hootman and Stoddard for a 1.124 mg HDR ^{252}Cf source provide calculated in-air dose equivalent rates of 21.64 and 1.52 mSv h^{-1} at 1.1 m for neutrons and photons, respectively; and modern ORNL-based parameters predicted 20.5 mSv h^{-1} from neutrons and 1.76 mSv h^{-1} from photons at 1.1 m. In-air neutron measurements with Neutrak®

dosimeters agreed with predicted values within 5% and photon measurements using Luxel® dosimeters agreed within 32%.

Between positions 7 and 9 there was 38.1 cm of high-density concrete and 41.3 cm of low-density concrete. As the data in Hootman and Stoddard could not be directly tabulated for a multi-component shield, calculations were made for various thickness of each shield type and presented in **Table 4.2.5**. Because of the 1.1 m air gap between the source and the vault wall, a geometrical factor of $(4\pi \cdot r^2)^{-1}$ was added to reduce the calculated values by a factor of 15. **Table 4.2.5** shows that the full thickness of low-density concrete and the actual thickness of high-density concrete (38.1 cm) would not provide adequate shielding to prevent a reading on the Landauer dosimeters. However, the 38.1 cm thick high-density shield in combination with a low-density shield would likely provide the expected attenuation, as shown by dual element Landauer dosimeters at positions 7 and 9.

Table 4.2.5: Calculated neutron and photon dose equivalent rates at the surface of a high- or low-density concrete shield containing 1.124 mg of ^{252}Cf. A geometrical factor of $(4\pi r^2)^{-1}$ was included to account for the position of the HDR ^{252}Cf source within the vault.

Concrete Density [g cm^{-3}]	Thickness [cm]	$Hp(10)_n$ [μSv h^{-1}]	$Hp(10)_\gamma$ [μSv h^{-1}]	< LLD‡
2.33	41.3	726 ± 40	88 ± 5	N
2.33	79.4	87 ± 7	15 ± 1	N
4.63	38.1	42 ± 2	9 ± 0.7	N
4.63	79.4	0.2 ± 0.01	0.09 ± 0.007	Y
3.14*	79.4	< 0.6	< 0.3	Y

‡ LLD < 0.06 μSv h^{-1} for neutrons and < 0.03 μSv h^{-1} for photons.

* Calculated using a thickness-weighted average of the two types of concrete in the vault wall.

Few ^{252}Cf shielding analyses have been published to date. In addition to the reports of Hootman and of Hootman and Stoddard, da Silva and Crispim used Monte Carlo methods (MCNP4B) to calculate the shielding capability of spherical shells of borated polyethylene, stainless steel, and borated-lead polyethylene around a ^{252}Cf source within a 30 cm radius sphere of high-density polyethylene.[99] Because of the variable

combination of multiple materials used in the analysis by da Silava and Crispim, comparison to Hootman and Stoddard is not practical.

Based on improvements in radiation transport software over the past 30 years since the first ^{252}Cf shielding report by Hootman, and advances in the field of health physics (e.g., ICRP 26 being replaced by ICRP 60) not addressed by da Silva and Crispim, further ^{252}Cf shielding analyses that provide a breadth of data similar to the report for diagnostic x-ray facilities by Dixon and Simpkin are needed.[126]

4.2.6 CONCLUSIONS

The shielding capability of a medical linear accelerator vault for containing ^{252}Cf radiations was demonstrated using multiple measuring techniques, including personnel dosimeters, portable radiation detectors, and Monte Carlo simulation. CR-39 track-etch detectors, optically stimulated luminescent dosimeters, ionization chambers, and neutron-sensitive proportional counters yielded no measurable radiation fields outside of the vault when a 1.124 mg ^{252}Cf HDR source was positioned in-air at the proposed treatment location for 3.4 hours. As the dosimeters employed were not sensitive to thermal- to low-energy neutrons, the Monte Carlo simulations validated the fast neutron findings and indicated that lower energy neutrons would similarly not be of concern.

With an assumption that radiation fields outside of the vault approached the lower limit of detection, over 10,000 twenty-minute treatment fractions per year could occur without reaching the annual radiation dose limit for a member of the public. The vault provided adequate reduction in radiation dose equivalent rate to treat patients with a medical HDR brachytherapy source with ~ 75 mg of ^{252}Cf. While an assessment of this type may be repeated at other facilities, the authors recommend that comprehensive ^{252}Cf shielding analyses for common building materials and treatment room geometries be performed to facilitate widespread implementation of medical HDR ^{252}Cf brachytherapy in the future.

5 Conclusions

5.1 Summary

Aspects of photon- and neutron-based brachytherapy were examined using MC methods, the AAPM TG-43 brachytherapy dosimetry formalism, and measurements. MC simulations employing monoenergetic photon and neutron radiation demonstrated generalizable characteristics of TG-43 brachytherapy dosimetry parameters. These findings can be employed to estimate the shape of brachytherapy dose distributions for new radionuclide sources.

Limited phantom size and material inhomogeneity were shown to impact MC calculations of photon dose distributions, and in some instances, significant variations from TG-43-calculated dose distributions were obtained. The related impact on the brachytherapy patient was explored in two clinical cases: eye plaque brachytherapy with ^{103}Pd, ^{125}I, and ^{131}Cs sources and superficial ^{252}Cf plaque brachytherapy. For eye plaque brachytherapy, MC studies demonstrated that material inhomogeneities engendered dose distributions that were -18%, -11%, and -10% at a prescription depth of 5 mm for ^{103}Pd, ^{125}I, and ^{131}Cs, respectively. As such, patient doses were at least 10% less than prescribed doses, and physicians may change prescriptive goals in concert with improvements in dosimetry calculations.[127,128] For ^{252}Cf plaque brachytherapy, partial scatter conditions were shown to similarly decrease planned therapy doses by approximately 10%. Since a 10% change in dose may be clinically relevant, future brachytherapy treatment planning systems should incorporate corrections to account for scatter conditions.[129,130]

Finally, calculations and measurements were employed to evaluate shielding requirements for ^{252}Cf brachytherapy. Water, concrete, barite concrete, Pb, polyethylene, and borated polyethylene were examined using MC simulations for neutron, primary photon, and secondary photon attenuation. These results can be employed towards selecting appropriate shielding materials and estimating the shielding capability of a proposed storage safe. In addition, measurements of a ^{252}Cf radiography source in a linear accelerator vault were performed to determine suitability for HDR ^{252}Cf brachytherapy. The linear accelerator vault, which had walls constructed primarily of high-density and low-density concrete, could adequately attenuate neutrons and photons from a 5 mg ^{252}Cf source.

5.2 Future work

5.2.1 PHOTON BRACHYTHERAPY

In **sections 2.1** and **2.2**, correction factors are presented to account for brachytherapy dosimetry formalism limitations due to phantom size (**Figure 2.1.1**) for point sources and to heterogeneity effects (**Table 2.2.3**) for eye plaques using the source models 200, 6711, and CS-1 Rev2. Similar evaluations are in progress to evaluate and compare scatter effects in limited phantom sizes. For example, recent MC-based phantom studies demonstrated that the ^{192}Ir point source radial dose function calculated in a 24 cm diameter sphere of liquid water is comparable to one calculated in a cubic water phantom with side length 20 cm.[131] Factors were developed for comparing spherical, cubical, and cylindrical phanta. Because many source calibration measurements with TLDs are performed in a rectangular geometry and MC calculations are generally in a spherical phantom, factors such as these may account for differences observed between calculated and measured dosimetry parameters. Other authors have similarly studied the impact of partial scatter environments and offered specific correction factors.[132,133] For example, Melchert *et al.* evaluated dose decrease for an ^{192}Ir point source in a rectangular phantom using MC calculations, an algorithm based on electric field theory, and ionization chambers.[133]

While one-dimensional corrections such as those described above can correct contemporary treatment planning algorithms following the AAPM TG-43 brachytherapy

dosimetry formalism, it is preferred to directly calculate patient dose without requiring numerous publications and references for case-specific correction factors. In 2005, Chibani *et al.* described a MC-based treatment planning program for prostate implants (MCPI) that incorporates tissue hetereogeneities, patient scatter conditions, and inter-seed effects.[134,135] MCPI can calculate dose distributions in a prostate for ~100 radioactive sources in minutes. Rapid calculations are possible because MCPI employs a stored phase space data model for each brachytherapy source to eliminate simulations of intra-source photons, which can account for up to 50% of computational time in MCNP5 brachytherapy source simulations.[135] In comparison to MCPI which uses phase space data, BrachyDose is a MC radiation transport code using EGSnrc that can simulate prostate implants in minutes of computational time.[136] BrachyDose calculated brachytherapy dosimetry parameters for different commercial seeds and radionuclides that are within ~1% of AAPM consensus data.[136]

MCPI and BrachyDose are likely the predecessors of the next generation of brachytherapy treatment planning systems. These systems will employ MC calculations to accurately correct for tissue heterogeneity, inter-seed attenuation, and phantom size effects. Furthermore, short computation times will enable routine clinical use. However, additional work is needed to integrate patient-specific data with MC simulations using either a pre-calculated dose kernel[129,130,135] or direct MC calculation.[136]

5.2.2 Neutron Brachytherapy

Interest in HDR ^{252}Cf brachytherapy by the medical community continues. However, commercial treatment delivery systems have not been introduced. In 1999, ORNL entered into a Cooperative Research and Development Agreement with Isotron, Inc. (Alpharetta, GA) to develop HDR sources.[137] In addition to the development of a ^{252}Cf remote afterloading system, Isotron, Inc., is also exploring combinational therapeutic techniques, such as combining neutron brachytherapy with boron neutron capture therapy.[44,137]

One limiting factor in the development of ^{252}Cf-based brachytherapy is the availability of ^{252}Cf. In 1970, the Atomic Energy Comission sold ^{252}Cf to the University of Kentucky for \$10 μg^{-1}.[34] Rivard reported the cost to be \$56 μg^{-1} in 1999,[93] and Rivard

et al. noted an increase to \$72 μg^{-1} by 2004.[104] Thus, a commercial medical HDR ^{252}Cf source with source strength > 1 mg may be prohibitively expensive. In the past, ORNL has made ^{252}Cf sources available to hospitals and universities through the Californium University Loan Program.[138] With sufficient medical interest, the Department of Energy may support a growing ^{252}Cf brachytherapy industry by providing discounted ^{252}Cf for clinical use.

5.3 Summary statement

In this dissertation, contemporary challenges in brachytherapy were addressed with an emphasis on calculation of brachytherapy dose distributions for photon- and neutron-emitting sources. These efforts were directed towards improving the accuracy of dose calculation in the absence of full-scatter and in heterogeneous media. In addition, a radiological health evaluation was performed for the unique shielding challenges posed by neutron brachytherapy.

6 References

1. American Cancer Society, "Cancer facts & figures 2007," American Cancer Society, Atlanta, GA (2007).
2. S. Nag, J. M. Quivey, J. D. Earle, D. Followill, J. Fontanesi, and P. T. Finger, "The American Brachytherapt Society recommendations for brachytherapy of uveal melanoma," Int. J. Radiat. Oncol. Biol. Phys. **56**, 544-555 (2003).
3. J. Rownd, "Applicator design and dose distributions," B. R. Thomadson, M. J. Rivard, W. M. Butler, eds., *Brachytherapy Physics, Second Edition*, American Association of Physicists in Medicine Medical Monograph No. 31, Medical Physics Publishing, Madison, WI (2005).
4. J. M. Hannoun-Levi, J. J. Mazeron, H. Marsiglia, and J. P. Gerard, "Partial breast irradiation: revolution or evolution?" Cancer Treat. Rev. **30**, 599-607 (2004).
5. A. G. Bell, "The uses of radium," Ann Med **6**, 261 (1903).
6. J. F. Williamson, "Semiempirical dose-calculation models in brachytherapy," B. R. Thomadson, M. J. Rivard, W. M. Butler, eds., *Brachytherapy Physics, Second Edition*, American Association of Physicists in Medicine Medical Monograph No. 31, Medical Physics Publishing, Madison, WI (2005).
7. J. Chavaudra, "Pierre and Marie Curie-Sklodowska," Med. Phys. **22**, 1877-1887 (1995).
8. M. T. Gillin and F. Mourtada, "Systems 1B Manchester planar and volume implants and the Paris system," B. R. Thomadson, M. J. Rivard, W. M. Butler, eds., *Brachytherapy Physics, Second Edition*, American Association of Physicists in Medicine Medical Monograph No. 31, Medical Physics Publishing, Madison, WI (2005).
9. R. E. Wallace, "LDR sources: design and delivery systems," B. R. Thomadson, M. J. Rivard, W. M. Butler, eds., *Brachytherapy Physics, Second Edition*, American Association of Physicists in Medicine Medical Monograph No. 31, Medical Physics Publishing, Madison, WI (2005).
10. R. Nath, L. L. Anderson, G. Luxton, K. A. Weaver, J. F. Williamson, and A. S. Meigooni, "Dosimetry of interstitial brachytherapy sources: Recommendations of the AAPM Radiation Therapy Committee Task Group No. 43," Med. Phys. **22**, 209-234 (1995).

11. G. P. Glasgow, J. D. Bourland, P. W. Grigsby, J. A. Meli, and K. A. Weaver, "Remote afterloading technology," AAPM Report 41, American Association of Physicists in Medicine, New York, NY (1993).

12. R. G. Dale, I. P. Coles, C. Deehan, and J. A. O'Donoghue, "Calculation of integrated biological response in brachytherapy," Int. J. Radiat. Oncol. Biol. Phys. **38**, 633-642 (1997).

13. B. R. Prestidge and W. S. Bice, "Clinical outcomes of a Phase II, multi-institutional cesium-131 permanent prostate brachytherapy trial," Brachytherapy **6**, 78 (2007).

14. J. F. Williamson, "Monte Carlo modeling of the transverse-axis dose distribution of the Model 200 ^{103}Pd interstitial brachytherapy source," Med. Phys. **27**, 643-654 (2000).

15. J. Dolan, L. Zuofeng, and J. F. Williamson, "Monte Carlo and experimental dosimetry of an ^{125}I brachytherapy seed," Med. Phys. **33**, 4675-4684 (2006).

16. M. J. Rivard, S. D. Davis, L. A. DeWerd, T. W. Rusch, and S. Axelrod, "Calculated and measured brachytherapy dosimetry parameters in water for the Xoft Axxent X-Ray Source: An electronic brachytherapy source," Med. Phys. **33**, 4020-4032 (2006).

17. A. S. Meigooni and R. E. Wallace, "Treatment planning considerations of brachytherapy procedures," B. R. Thomadson, M. J. Rivard, W. M. Butler, eds., *Brachytherapy Physics, Second Edition*, American Association of Physicists in Medicine Medical Monograph No. 31, Medical Physics Publishing, Madison, WI (2005).

18. S. M. Seltzer, P. J. Lamperti, R. Loevinger, M. G. Mitch, J. T. Weaver, and B. M. Coursey, "New national air-kerma-strength standards for ^{125}I and ^{103}Pd brachytherapy seeds," J. Res. Natl. Inst. Stand. Technol. **108**, 337-358 (2003).

19. T. P. Loftus, "Exposure standardization of iodine-125 seeds used for brachytherapy," J. Res. Natl. Inst. Stand. Technol. **89**, 295-303 (1984).

20. M. J. Rivard, B. M. Coursey, L. A. DeWerd. W. F. Hanson, M. S. Huq, G. S. Ibbott, M. G. Mitch, R. Nath, and J. F. Williamson, "Update of AAPM Task Group No. 43 Report: A revised AAPM protocol for brachytherapy dose calculations," Med. Phys. **31**, 633-674 (2004).

21. T. R. Mackie, J. W. Scrimger, and J. J. Battista, "A convolution method of calculating dose for 15-MV x rays," Med. Phys. **12**, 188-196 (1985).

22. T. R. Mackie, E. El-Khatib, J. J. Battista, and J. W. Scrimger, "Lung dose corrections for 6- and 15-MV x rays," Med. Phys. **12**, 327-332 (1985).

23. D. T. Chang, K. R. Olivier, C. G. Morris, C. Liu, J. F. Dempsey, , R. K. Benda, and J. R. Palta, "The impact of heterogeneity correction on dosimetric parameters that predict for radiation pneumonitis," Int. J. Radiat. Oncol. Bio. Phys. **65**, 125-131 (2006).

24. K. Mah and J. Van Dyk, "On the impact of tissue inhomogeneity corrections in clinical thoracic radiation therapy," Int. J. Radiat. Oncol. Bio. Phys. **21**, 1257-1267 (2006).

25. J. F. Williamson, B. M. Coursey, L. A. DeWerd, W. F. Hanson, and R. Nath, ''Dosimetric prerequisites for routine clinical use of new low energy photon interstitial brachytherapy sources,'' Med. Phys. **25**, 2269–2270 (1998).
26. M. J. Rivard, "Brachytherapy dosimetry parameters calculated for a ^{131}Cs source," Med. Phys. **34**, 754-762 (2007).
27. J. Pérez-Calatayud, D. Granero, F. Ballester, E. Casal, R. Cases, and S. Agramunt, "Monte Carlo derivation of TG-43 dosimetric parameters for radiation therapy resources and 3M Cs-137 sources," Med. Phys. **32**, 2464-2470 (2005).
28. D. C. Medich, M. A. Tries, and J. J. Munro, "Monte Carlo characterization of an ytterbium-169 high dose rate brachytherapy source with analysis of statistical uncertainty," Med. Phys. **33**, 163-172 (2006).
29. G. M. Daskalov, E. Löffler, and J. F. Williamson, "Monte Carlo-aided dosimetry of a new high dose-rate brachytherapy source," Med. Phys. **25**, 2200-2208 (1998).
30. M. J. Rivard, "Neutron dosimetry for a general ^{252}Cf brachytherapy source," Med. Phys. **27**, 2803-2815 (2000).
31. M. Sarfaraz, A. S. Kennedy, Z. J. Cao, G. D. Sackett, C. X. Yu, M. A. Lodge, R. Murthy, B. R. Line, and D. A. Van Echo, "Physical aspects of yttrium-90 microsphere therapy for nonresectable hepatic tumors," Med. Phys. **30**, 199-203 (2003).
32. J. F. Dempsey, J. A. Williams, J. B. Stubbs, T. J. Patrick, and J. F. Williamson, "Dosimetric properties of a novel brachytherapy balloon applicator for the treatment of malignant brain-tumor resection-cavity margins," Int. J. Radiat. Oncol. Biol. Phys. **42**, 421-429 (1998).
33. NUDAT 2.4, National Nuclear Data Center, Brookhaven National Laboratory, http://www.nndc.bnl.gov/nudat2/index.jsp (last accessed January 1, 2008).
34. J. B. Knauer and R. C. Martin, "Californium -252 production and neutron source fabrications," J. G. Wierzbicki, ed., *Californium-252 isotope for 21st Century radiotherapy*, NATO ASI Series 3. High Technology, **29**, Kluwer Academic Publishers, Dordrecht, Netherlands (1997).
35. C. S. Schlea and D. H. Stoddard, "Californium isotopes proposed for intracavity and interstitial therapy with neutrons," Nature **206,** 1058-1059 (1965).
36. Y. Maruyama, J. G. Wierzbicki, B. M. Vtyurin, and K. Kaneta, "Californium-252 neutron brachytherapy," *Principles and practice of brachytherapy*, S. Nag (ed), Futura Publishing Co., Inc., Armonk, NY USA (1997).
37. T. Tačev, B. Ptáčková, and V. Strnad, "Comparison of twelve-year treatment results of advanced cervical carcinoma with californium-252 vs. gamma radiation only in brachytherapy," Radiotherapy Oncol. **71**(S2), S8 (2004).
38. V. Krishnaswamy, "Calculated depth dose tables for californium-252 sources in tissue," Phys. Med. Biol. **17**, 56-63 (1972).
39. R. D. Colvett, H. H. Rossi, and V. Krishnaswamy, "Dose distributions around a californium-252 needle," Phys. Med. Biol. **17**, 356-364 (1972).
40. J. P. Windham, A. Shapiro, and J. G. Keriakes, "Calculated neutron dose rates for implantable californium-252 sources," Phys. Med. Biol. **17**, 493-502 (1972).
41. E. Storm and H. I. Israel, "Photon cross section from 1 keV to 100 MeV for elements Z = 1 to Z = 100," Nuclear Data Tables A7, 565, 681 (1970).

42. J. J. Ritts, M. Solomito, and P. N. Stevens, "Calculation of neutron fluence-to-kerma factors for the human body," Nucl. App. Tech. **7**, 89 (1969).
43. L. L. Anderson, "Status of dosimetry for ^{252}Cf medical neutron sources," Phys. Med. Bio. **18**, 779-799 (1973).
44. J. C. Yanch and R. G. Zamenhof, "Dosimetry or ^{252}Cf sources for neutron radiotherapy with and without augmentation by boron neutron capture therapy," Radiation Research, **131**, 249-256 (1992).
45. R. C. Martin, R. R. Laxson, J. H. Miller, J. G. Wierzbicki, M. J. Rivard, and D. L. Marsh, "Development of high-activity ^{252}Cf sources for neutron brachytherapy," Appl. Radiat. Isot. **48**, 1567-1570 (1997).
46. J. Dutreix and A. Dutreix, "Henri Becquerel (1852-1908)", Med. Phys. **22**, 1869-1875 (1995).
47. T. Tačev, G. Grigorov , T. Papirek, and V. Kolarik, "Remote afterloading for neutron brachytherapy using californium-252," Strahlenther. Onkol. **179**, 113-117 (2003).
48. H. E. Hootman, "Estimation of ^{252}Cf shielding requirements," (Aiken, SC: Savannah River Laboratory) (1970).
49. H. E. Hootman and D. H. Stoddard, "^{252}Cf shielding guide," Savannah River Laboratory, Aiken, SC (1971).
50. ICRP, "1990 Recommendations of the International Commission on Radiological Protection," International Commission on Radiation Units and Measurements Report 60, Pergamon Press, Oxford, United Kingdom (1990).
51. S.-T. Chiu-Tsao, L. L. Anderson, K. O'Brien, L. Stabile, and J. C. Liu, "Dosimetry for ^{125}I seed (model 6711) in eye plaques," Med. Phys. **20**, 383-389 (1993).
52. C. S. Melhus and M. J. Rivard, "Approaches to calculating AAPM TG-43 brachytherapy dosimetry parameters for ^{137}Cs, ^{125}I, ^{192}Ir, ^{103}Pd, and ^{169}Yb sources," Med. Phys. **33**, 1729-1737 (2006).
53. C. S. Melhus and M. J. Rivard, "COMS eye plaque brachytherapy dosimetry for ^{103}Pd, ^{125}I, and ^{131}Cs," Med. Phys. (submitted, 07-853).
54. C. S. Melhus, M. J. Rivard, B. L. Kirk, and L. C. Leal, "Clinical brachytherapy dosimetry parameters and mixed-field dosimetry for a high dose rate Cf-252 brachytherapy source," The Monte Carlo method: Versatility unbounded in a dynamic computing world, Amer Nuc Soc, p. 269 (2005).
55. C. S. Melhus and M. J. Rivard, "Monte Carlo validation of clinical brachytherapy dosimetry under partial scatter conditions for neutron-emitting sources," Med. Phys. **34**, 2330 (2007).
56. C. S Melhus, M. J. Rivard, B. L. Kirk, L. C. Leal, "Storage safe shielding assessment for a HDR californium-252 brachytherapy source," The Monte Carlo method: Versatility unbounded in a dynamic computing world, Amer Nuc Soc, p. 190 (2005).
57. C. S. Melhus, M. J. Rivard, J. KurKomelis, C. B. Liddle, and F. X. Massé, "Shielding evaluation of a medical linear accelerator vault in preparation for installing a high dose rate ^{252}Cf remote afterloader," Rad. Prot. Dos. **113**, 428-437 (2005).

58. M. J. Rivard, "Refinements to the geometry factor used in the AAPM Task Group Report No. 43 necessary for brachytherapy dosimetry calculations," Med. Phys. **26**, 2445-2450 (1999).
59. E. Kouwenhoven, R. van der Laarse, and D. R. Schaart, "Variation in interpretation of the AAPM TG-43 geometry factor leads to unclearness in brachytherapy dosimetry," Med. Phys. **28**, 1965-1966 (2001).
60. J. A. Meli, "Let's abandon geometry factors other than that of a point source in brachytherapy dosimetry," Med. Phys. **29**, 1917-1918 (2002).
61. M. J. Rivard, B. M. Coursey, L. A. DeWerd, W. F. Hanson, M. S. Huq, G. Ibbott, R. Nath, and J. F. Williamson, "Comment on: Let's abandon geometry factors other than that of a point source in brachytherapy dosimetry," Med. Phys. **29**, 1919-1920 (2002).
62. A. S. Meigooni, V. Rachabatthula, S. B. Awan, and R. A. Koona, "Comment on 'Update of AAPM Task Group No. 43 Report: A revised AAPM protocol for brachytherapy dose calculations,'" Med. Phys. **32**, 1820-1821 (2005).
63. M. J. Rivard, W. M. Butler, L. A. DeWerd, M. S. Huq, G. Ibbott, C. S. Melhus, M. G. Mitch, R. Nath, and J. F. Williamson, "Response to "Comment on `Update of AAPM Task Group No. 43 Report: A revised AAPM protocol for brachytherapy dose calculations' " [Med. Phys. 31, 633-674 (2004)]," Med. Phys. **32**, 1822-1824 (2005).
64. O. Chibani, J. F. Williamson, and D. Todor, "Dosimetric effects of seed anisotropy and interseed attenuation for ^{103}Pd and ^{125}I prostate implants," Med. Phys. **32**, 2557-2566 (2005).
65. O. Chibani and J. F. Williamson, "MCPI©: A sub-minute Monte Carlo dose calculation engine for prostate implants," Med. Phys. **32**, 3688-3698 (2005).
66. G. P. Glasgow and L. T. Dillman, "Specific γ-ray constant and exposure rate constant on ^{192}Ir," Med. Phys. **6**, 49-52 (1979).
67. X-5 Monte Carlo Team, "MCNP – A general Monte Carlo N-Particle transport code, Version 5," Los Alamos National Laboratory, Los Alamos, NM (2003).
68. Cross Section Evaluation Working Group. "ENDF/B-VI Summary Documentation (ENDF-201)," Brookhaven National Laboratory report BNL-NCS-17541, 8th Edition, National Nuclear Data Center (December 2000).
69. M. J. Rivard, C. S. Melhus, and B. L. Kirk, "Brachytherapy dosimetry parameters calculated for a new ^{103}Pd source," Med. Phys. **31**, 2466-2470 (2004).
70. ICRU, "Tissue substitutes in radiation dosimetry and measurement," International Commission on Radiation Units and Measurements Report 44, Bethesda, MD USA (1989).
71. J. H. Hubbell and S. M. Seltzer, "Tables of X-Ray Mass Attenuation Coefficients and Mass Energy-Absorption Coefficients (version 1.4)," National Institute of Standards and Technology, Gaithersburg, MD (2004), http://physics.nist.gov/xaamdi [last accessed 1 March 2008].
72. N. Reynaert, H. Palmans, H. Thierens, and R. Jeraj, "Parameter dependence of the MCNP electron transport in determining dose distributions," Med. Phys. **29**, 2446-2454 (2002).
73. J. Pérez-Calatayud, D. Granero, and F. Ballester, "Phantom size in brachytherapy source dosimetric studies," Med. Phys. **31**, 2075-2081 (2004).

74. J. F. Williamson, "Dosimetric characteristics of the DRAXIMAGE model LS-1 I-125 interstitial brachytherapy source design: A Monte Carlo investigation," Med. Phys. **29**, 509-521 (2002).
75. B. Reniers, "Monte Carlo study of the effect of the tissue composition on the dosimetric data used for low energy photons," Med. Phys. **32**, 2069 (2005).
76. J. F. Williamson and Z. Li, "Monte Carlo aided dosimetry of the MicroSelectron pulsed and high dose-rate ^{192}Ir sources," Med. Phys. **22**, 809-819 (1995).
77. M. J. Price, J. L. Horton, K. A. Gifford, P. J. Eifel, A. Jhingran, A. A. Lawyer, P. A. Berner, and F. Mourtada, "Dosimetric evaluation of the Fletcher-Williamson ovoid for pulsed-dose-rate brachytherapy: A Monte Carlo study," Phys. Med. Biol. **50**, 5075-5087 (2005).
78. J. L. M. Venselaar, P. H. van der Giessen, and W. J. F. Dries, "Measurement and calculation of the dose at large distances from brachytherapy sources: Cs-137, Ir-192, and Co-60," Med. Phys. **23**, 537-543 (1996).
79. J. F. Williamson, "Monte Carlo-based dose-rate tables for the Amersham CDCSJ and 3M model 6500 ^{137}Cs tubes," Int. J. Radiat. Oncol. Bio. Phys. **41**, 959-970 (1998).
80. E. Casal, F. Ballester, J. L. Lluch, J. Pérez-Calatayud, and F. Liso, "Monte Carlo calculations of dose rate distributions around the Amersham CDCS-M-type ^{137}Cs source," Med. Phys. **27**, 132-140 (2000).
81. G. Luxton, M. A. Astrahan, and Z. Petrovich, "Backscatter measurement from a single seed of ^{125}I for ophthalmic plaque dosimetry," Med. Phys. **15**, 397-400 (1988).
82. M. A. Astrahan, "Improved treatment planning for COMS eye plaques," Int. J. Radiat. Oncol. Biol. Phys. **61**, 1227-1242 (2005).
83. M. J. Rivard, "Monte Carlo calculations of AAPM Task Group Report No. 43 dosimetry parameters for the MED3631-A/M ^{125}I source," Med. Phys. **28**, 629-637 (2001).
84. J. F. Williamson and R. Nath, "Clinical implementation of AAPM Task Group 32 recommendations on brachytherapy source strength specification," Med. Phys. **18**, 439-448 (1991).
85. R. S. Wittman and D. R. Fisher, "Multiple-estimate Monte Carlo calculation of the dose rate constant for a cesium-131 interstitial brachytherapy seed," Med. Phys. **34**, 49-54 (2007).
86. A. G. Kepka, P. M. Johnson, and R. W. Kline, "The generalized geometry of eye plaque therapy," Med. Phys. **15**, 375-379.
87. M. A. Astrahan, A. Szechter, and P. T. Finger, "Design and dosimetric considerations of a modified COMS plaque: The reusable "seed-guide" insert," Med. Phys. **32**, 2706-2716 (2005).
88. A. de la Zerda, S.-T. Chiu-Tsao, J. Lin, L. L. Boulay, I. Kanna, J. H. Kim, and H.-S. Tsao, "^{125}I eye plaque dose distribution including penumbra characteristics," Med. Phys. **23**, 407-418 (1996).
89. M. J. Rivard, C. S. Melhus, S. Sioshansi, J. Morr, "Impact of prescription depth, dose, dose rate, plaque size, and source loading using ^{103}Pd, ^{125}I, and ^{131}Cs: A modern assessment of eye plaque dosimetry," Brachytherapy (accepted, 2007-62).

90. A. L. Krintz, W. F. Hanson, G. S. Ibbott, and D. S. Followill, "A reanalysis of the collaborative ocular melanoma study medium tumor trial eye plaque dosimetry," Int. J. Radiat. Oncol. Biol. Phys. **56**, 889-898 (2003).
91. ICRU, "Nuclear data for neutron and proton radiotherapy and for radiation protection," International Commission on Radiation Units and Measurements Report 63, Bethesda, MD USA (2000).
92. W. Mannhart, "Evaluation of the Cf-252 fission neutron spectrum between 0 MeV and 20 MeV," IAEA-TECDOC-410, 158-171 (1987).
93. M. J. Rivard, J. G. Wierzbicki, F. Van den Heuvel, R. C. Martin, and R. R. McMahon, "Clinical brachytherapy with neutron emitting ^{252}Cf sources and adherence to AAPM TG-43 dosimetry protocol," Med. Phys., **26**, 87-96 (1999).
94. "Experimental Nuclear Reaction Data (EXFOR/CSISRS)," National Nuclear Data Center, Brookhaven National Laboratory, http://www.nndc.bnl.gov/exfor/index.html (2005) [last accessed 1 March 2008].
95. K. Skarsvåg, "Differential angular distribution of prompt gamma rays from spontaneous fission of ^{252}Cf," Phys. Rev. C, **22**, 638-650 (1980).
96. V. V. Verbinski, H. Weber, and R. E. Sund, "Prompt gamma rays from ^{235}U(n,f), ^{239}Pu(n,f), and spontaneous fission of ^{252}Cf," Phys. Rev. C, **7**, 1173-1185 (1973).
97. J. B. Knauer, C. W. Alexander, and J. E. Bigelow, "Cf-252: properties, production, source fabrication and procurement," Nuc. Sci. Appl., **4**, 3-17 (1991).
98. Y. Maruyama, "Neutron brachytherapy for the treatment of malignant neoplasia," Int. J. Radiat. Oncol. Bio. Phys., **15**, 1415-1429 (1988).
99. A. X. da Silva and V. R. Crispim, "Shielding design studies for a neutron irradiator system based on a ^{252}Cf source," Radiat. Prot. Dos. **95**, 333-338 (2001).
100. "Computational Pile – LINUX Cluster," Nuclear Science and Technology Division, Oak Ridge National Laboratory, http://cpile.ornl.gov/index.html (last accessed August 18, 2004) [no longer available].
101. M. J. Rivard, K. E. Evans, L. C. Leal, and B. L. Kirk, "Selective perturbation of in vivo linear energy transfer using high-Z vaginal applicators for Cf-252 brachytherapy," Nucl. Inst. Meth. Phys. Res. B **213**, 621-625 (2004).
102. J. J. DeMarco, R. E. Wallace, and K. Boedeker, "An analysis of MCNP cross-sections and tally methods for low-energy photon emitters," Phys. Med. Biol. **47**:1321-1332 (2002).
103. T. D. Bohm, P. M. DeLuca, and L. A. DeWerd, "Brachytherapy dosimetry of ^{125}I and ^{103}Pd sources using an updated cross section library for the MCNP Monte Carlo transport code," Med. Phys. **30**:701-711 (2003).
104. Rivard, M. J., Kirk, B. L., Stapleford, L. J. and Wazer, D. E. "A comparison of the expected costs of high dose rate brachytherapy using ^{252}Cf versus ^{192}Ir," Appl. Radiat. Isot. **61**, 1211-1216 (2004).
105. Y. Maruyama, R. Kryscio, J. R. Van Nagell, J. Yoneda, E. Donaldson, M. Hanson, J. L. Beach, J. M. Feola, A. Martin, and C. Parker, "Clinical trial of ^{252}Cf neutron brachytherapy vs. conventional radiotherapy for advanced cervical cancer," Int. J. Radiat. Oncol. Biol. Phys. **11**, 1475-1482 (1985).
106. T. Tačev, B. Ptáčková, and V. Strnad, "Californium-252 (^{252}Cf) versus conventional gamma radiation in the brachytherapy of advanced cervical carcinoma," Strahlenther. Onkol. **179**, 377-384 (2003).

107. B. M. Vtyurin, V. S. Medvedev, V. A. Anikin, L. F. Ivanova, V. N. Ivanov, S. D. Fomin, and A. A. Omarov, "Neutron brachytherapy in the treatment of melanoma," Int. J. Radiat. Oncol. Biol. Phys. **28**, 703-709 (1994).
108. X. Tang, C. Cheng, and X. Xu, "Cf-252 neutron brachytherapy in China," 5th International topical meeting on industrial radiation and radioisotope measurement applications. Bologna, Italy, 51 (2002).
109. M. J. Rivard, "Burst calculations for ^{252}Cf brachytherapy sources," Med. Phys. **27**, 2816-2820 (2000).
110. M. J. Rivard, J. K. Sganga, F. d'Errico, J.-S. Tsai, K. Ulin, and M. J. Engler, "Calculated neutron air kerma strength conversion factors for a generically encapsulated Cf-252 brachytherapy source," Nuc. Instr. Meth. in Phys. Res. A **476**, 119-122 (2002).
111. National Council on Radiation Protection and Measurements. Structural shielding design and evaluation for medical use of x rays and gamma rays of energies up to 10 MeV. NCRP Report 49 (1976).
112. National Council on Radiation Protection and Measurements. Neutron contamination from medical electron accelerators. NCRP Report No. 79 (1984).
113. National Council on Radiation Protection and Measurements. Radiation protection for particle accelerator facilities. NCRP Report No. 144 (2003).
114. D. Robinson, J. W. Scrimger, G. C. Field, and B. G. Fallone, "Shielding considerations for tomotherapy," Med. Phys. **27**, 2380-2384 (2000).
115. S. Mutic, D. A. Low, E. E. Klein, J. F. Dempsey, and J. A. Purdy, "Room shielding for intensity-modulated radiation therapy treatment facilities," Int. J. Radiat. Oncol. Biol. Phys. **50**, 239-246 (2001).
116. B. M. Methe, "Shielding design for a PET imaging suite: a case study," Health Phys. **84**, S83-88 (2003).
117. L. K. Felker, REDC shipment no. 2065: Shipment of neutron sources, Radiochemical Engineering Development Center, Oak Ridge National Laboratory, 20 April 2004. Personal communication.
118. Health Physics Instruments. REM 500 instruction manual, revision A. (1998).
119. Keithley Instruments, Inc.. Integrating survey meter instruction manual, manual no. 32957IM, revision B. (1983).
120. Landauer, Inc.. Products and services [online]. http://ldrsolutions.landauerinc.com/PRODUCTCATALOG/ [last accessed 1 March 2008].
121. G. F. Knoll, *Radiation detection and measurement*, 3rd ed., New York: Wiley & Sons (2000).
122. 10CFR20.1003. Standards for Radiation Protection. U.S. Code of Federal Regulations Title 10, 1, 320-326 (2004).
123. M. J. Rivard, "Neutron dosimetry, moderated energy spectrum, and neutron capture therapy for ^{252}Cf medical sources," Ph.D. dissertation, Wayne State University: Detroit, MI (1998).
124. Personal communication, Landauer Neutron Calibration, Landauer, Inc., Glenwood, IL, 25 May 2004.
125. National Council on Radiation Protection and Measurements. Limitation of exposure to ionizing radiation. NCRP Report No. 116 (1993).

126. R. L. Dixon and D. J. Simpkin, Primary shielding barriers for diagnostic x-ray facilities: a new model. Health Phys. **74**, 181-189 (1998).
127. J. F. Williamson, W. Butler, L. A. DeWerd, M. S. Huq, G. S. Ibbott, Z. Li, M. G. Mitch, R. Nath, M. J. Rivard, and D. Todor, "Recommendations of the American Association of Physicists in Medicine regarding the Impact of Implementing the 2004 Task Group 43 Report on Dose Specification for ^{103}Pd and ^{125}I Interstitial Brachytherapy," Med. Phys. **32**, 1424-1439 (2005).
128. M. J. Rivard, W. M. Butler, P. M. Devlin, J. K. Hayes , R. A. Hearn, E. P. Lief, A. S. Meigooni, G. S. Merrick, and J. F. Williamson, "American Brachytherapy Society recommends no change for prostate permanent implant dose prescriptions using iodine-125 or palladium-103," Brachytherapy **6**, 34-37 (2007).
129. A. K. Carlsson and A. Ahnesjö, "The collapsed cone superposition algorithm applied to scatter dose calculations in brachytherapy," Med. Phys. **27**, 2320-2332 (2000).
130. A. K. Carlsson Tedgren and A. Ahnesjö, "Accounting for high Z shields in brachytherapy using collapsed cone superposition for scatter dose calculation," Med. Phys. **30**, 2206-2217 (2003).
131. Personal communication, F. Ballester and J. Pérez-Calatayud, 21 January 2008.
132. B. Kassas, F. Mourtada,2 J. L. Horton, R. G. Lane, T. A. Buchholz, and E. A. Strom, "Dose modification factors for ^{192}Ir high-dose-rate irradiation using Monte Carlo simulations," J. Appl. Clin. Med. Phys. **7**, 28-34 (2006).
133. C. Melchert, P. Kohr, and R. Schmidt, "Calculation of dose decrease in a finite phantom of a ^{192}Ir point source," Med. Phys. **34**, 3943-3950 (2007).
134. O. Chibani, J. F. Williamson, and D. Todor, "Dosimetric effects of seed anisotropy and interseed attenuation for ^{103}Pd and ^{125}I prostate implants," Med. Phys. **32**, 2557-2566 (2005).
135. O. Chibani and J. F. Williamson, "MCPI©: A sub-minute Monte Carlo dose calculation engine for prostate implants," Med. Phys. **32**, 3688-3698 (2005).
136. R. E. P. Taylor, G. Yegin, and D. W. O. Rogers, "Benchmarking BrachyDose: Voxel based EGSnrc Monte Carlo calculations of TG-43 dosimetry parameters," Med. Phys. **34**, 445-457 (2007).
137. R. C. Martin and D. S. Halpern, "Development of miniature high-dose-rate ^{252}Cf sources for boron-enhanced and fast neutron brachytherapy," ORNL, Cooperative Research and Development Agreement (2003).
138. Oak Ridge National Laboratory, "The californium sales/loan program," [online]. http://www.ornl.gov/sci/nuclear_science_technology/redc/ [last accessed 1 March 2008].

7 Appendices

7.1 Appendix I: List of acronyms and abbreviations

AAPM	American Association of Physicists in Medicine
ABS	American Brachytherapy Society
COMS	Collaborative Occular Melanoma Study
ENDF	Evaluated Nuclear Data File
HDR	High-dose rate
ICRP	International Council for Radiation Protection and Measurements
ICRU	International Commission on Radiation Units and Measurements
LDR	Low-dose rate
LLD	Lower limit of detection
MC	Monte Carlo
MCNP	Monte Carlo N-Particle
MMCI	Masaryk Memorial Cancer Institute (Czech Republic)
NCRP	National Council on Radiation Protection and Measurements
NEMC	New-England Medical Center
NIST	National Institute of Science and Technology
NNDC	National Nuclear Data Center
ORNL	Oak Ridge National Laboratory
RBE	Relative biological effectiveness
REDC	Radiochemical Engineering Development Center
TED	Threshold erythema dose
TG-43	AAPM Task Group 43 Report (Ref. **10**)
TG-43U1	Updated AAPM Task Group 43 Report (Ref. **20**)
WAFAC	Wide-Angle Free-Air Chamber (Ref. **18**)

7.2 Appendix II: Summary of the AAPM TG-43U1 dosimetry formalism

The AAPM report TG-43U1 brachytherapy dosimetry two-dimensional (2D) formalism is given in **Eq. 7.2.1**.[20]

$$\dot{D}(r,\theta) = S_K \cdot \Lambda \cdot \frac{G_L(r,\theta)}{G_L(r_0,\theta_0)} \cdot g_L(r) \cdot F(r,\theta) \qquad \textbf{(7.2.1)}$$

Where:	$\dot{D}(r,\theta)$	dose rate at position (r,θ) in spherical coordinates [cGy h^{-1}]
	S_K	Air kerma strength [cGy cm^2 h^{-1}]
	Λ	Dose rate constant [cm^{-2}]
	$G_L(r,\theta)$	Geometry function for the line-source approximation
	$g_L(r)$	Radial dose function
	$F(r,\theta)$	2D anisotropy function
	r_0	Reference radial distance (r_0 = 1 cm)
	θ_0	Reference angle from the seed long axis (θ_0 = 90°)

Eq. 7.2.1 employs a spherical coordinate system to calculate dose rate distributions in the plane coincident with the source long axis. Cylindrical symmetry about the source is assumed. The first two terms, S_K and Λ, normalize the individual source strength to the reference dose rate, $\dot{D}(r_0,\theta_0)$. The remaining terms account for the geometrical effects of inverse square law and attenuation through source components. The subscript L denotes the line source approximation of the geometry function.

Eq. 7.2.2 defines Λ and describes the reference dose rate characteristics for a given seed design. The brachytherapist need only multiple Λ by S_K for a given seed/source to obtain the dose rate [cGy h^{-1}] at the reference point.

$$\Lambda = \frac{\dot{D}(r_0,\theta_0)}{S_K} \qquad \textbf{(7.2.2)}$$

The geometry function corrects for inverse square law effects. For a point source, the geometry function follows the inverse square law and is called $G_P(r,\theta)$ where the subscript P denotes the point source approximation. As source length increases; however, the geometry function must account for the distributed nature of the source. Two defining regimes are given in **Eq. 7.2.3**.

$$G_L(r,\theta)=\begin{cases}\dfrac{\beta}{Lr\cdot\sin(\theta)} & \text{if } \theta\neq 0^\circ \\ \left(r^2-L^2/4\right)^{-1} & \text{if } \theta=0^\circ\end{cases} \tag{7.2.3}$$

In **Eq. 7.2.3**, β is the angle in radians between the line source and calculation point, and L is the active length of the source. For linear sources including hollow right cylinders, L is defined as the length of the active region. An effective active length, L_{eff}, should be calculated by multiplying the number of distinct internal elements and their center-to-center spacing for sources with multiple internal components. If the calculated L_{eff} exceeds the source capsule length, brachytherapists are advised to use the maximum extent of the radioactivity distribution. Additional discussion of L_{eff} can be found in **Ref 63**.

The radial dose function, $g_L(r)$, calculates the rate of dose fall-off in the plane bisecting the source, known as the "transverse plane." Inverse square effects are accounted for in $G_L(r,\theta)$; thus, the radial dose function determines the relative amount of scattering and attenuation along θ=90°. **Eq. 7.2.4** defines the radial dose function.

$$g_L(r)=\frac{\dot{D}(r,\theta_0)}{\dot{D}(r_0,\theta_0)}\frac{G_L(r_0,\theta_0)}{G_L(r,\theta_0)} \tag{7.2.4}$$

As shown in **Eq. 7.2.4**, $g_L(r)$ is normalized to unity by the value at r_0.

In comparison to the relative dose decrease on the transverse plane, the 2D anisotropy function, $F(r,\theta)$, is the relative dose as a function of polar angle. As for $g_L(r)$, the 2D anisotropy function accounts for the scattering and attenuation in water and in source components. The definition of $F(r,\theta)$ is given in **Eq. 7.2.5**.

$$F(r,\theta)=\frac{\dot{D}(r,\theta)}{\dot{D}(r,\theta_0)}\frac{G_L(r,\theta_0)}{G_L(r,\theta)} \tag{7.2.5}$$

Some treatment planning systems do not allow for the characterization of source orientation. As such, the TG-43U1 dosimetry formalism includes a one-dimensional (1D) formalism. In this formalism, $G_P(r,\theta)$ is used, and $F(r,\theta)$ is replaced with the 1D anisotropy function, $\phi_{an}(r)$. The 1D anisotropy function is the solid-angle weighted

dose rate at a distance r relative to the dose rate at the same distance on the transverse plane. **Eq. 7.2.6** shows the equation for determining $\phi_{an}(r)$.

$$\phi_{an}(r) = \frac{\int_0^{\pi} \dot{D}(r,\theta) \cdot \sin(\theta) \cdot d\theta}{2\dot{D}(r,\theta_0)} \tag{7.2.6}$$

Substituting $G_P(r,\theta)$ and $\phi_{an}(r)$ into **Eq. 7.2.1** provides the recommended 1D dosimetry formalism shown in **Eq. 7.2.7**.

$$\dot{D}(r,\theta) = S_K \cdot \Lambda \cdot \left(\frac{r_0}{r}\right)^2 \cdot g_P(r) \cdot \phi_{an}(r) \tag{7.2.7}$$

It is important to note that the TG-43U1 brachytherapy dosimetry formalism allows additional formulae for the 1D formalism, and the interested reader is referred to **Ref. 20** for further reading.